UNIVERSITY OF OKLAHOMA

GRADUATE COLLEGE

EXPERIMENTAL AND COMPUTATIONAL ANALYSIS OF THE AERODYNAMICS OF MELT BLOWING DIES

A Dissertation

SUBMITTED TO THE GRADUATE FACULTY

in partial fulfillment of the requirements for the

degree of

Doctor of Philosophy

By

Eric Michael Moore
Norman, Oklahoma
2004

EXPERIMENTAL AND COMPUTATIONAL ANALYSIS OF THE AERODYAMICS OF MELT BLOWING DIES

A Dissertation Approved for the
SCHOOL OF CHEMICAL ENGINEERING AND MATERIALS SCIENCE

BY

_____
Professor Robert Shambaugh

_____
Professor Dimitrios Papavassiliou

_____
Professor Brian Grady

_____
Professor David Nelson

_____
Professor Faruk Civan

Acknowledgements

I would like to thank the following people for their contributions that made my education possible. All of these people have helped make my journey through graduate school a unique experience; a time of both hard work and hard play, one of deep thought and the occasional silliness.

Professor Robert Shambaugh, for serving as my advisor for these four years of work. Teaching me more that I ever thought I would need to know and providing financial support so I could be around to learn them.

Professor Dimitrios Papavassiliou, for being my co-advisor and instruction in Industrial Transport.

Professor Brian Grady, for serving on my committee and guidance in many interesting projects.

Professor Faruk Civan for serving as a member of my committee.

Professor David Nelson at 3M, for serving on my committee and providing guidance and a place to work while collecting data.

Vishnu, Diana, and Jacob, for being great co-workers and for being friends through both good times and bad.

Dr. Anne de Rovere at 3M, for helping me navigate the corporate world and making sure I had what I needed to get my work done.

Mr. Larry Isley, for all the help with the many projects I've worked on while here at OU.

My brother, Jason. For being both my brother and my friend.

My parents, Cheryl and Kenny Moore. For teaching me to think for myself and guiding me when my thinking led me astray. For all the support you have given me to make it through many years of study and work.

Table of Contents

List of Tables

List of Figures

Abstract

An experimental and computational study of melt blowing jets and processes was done. Computational studies were done on three types of melt blowing jets: conventional annular, tapered annular and swirling. Conventional annular melt blowing jets were simulated and compared with experimental data. Tapered annular jets were simulated and compared with conventional annular and slot jets. Swirling adhesive nozzles were simulated and compared with experimental data. Experimental work consisted of measurements of both slot dies and swirling adhesive nozzles. Pitot tube measurements were made on the air flow in the jets of both slot dies and swirling adhesive nozzles. The temperature field of a heated slot die jet was also measured. Online diameter measurements were made of the fibers produced by a pilot-scale melt blowing die using a new Ensemble Laser Diffraction (ELD) technique. Light absorbance of fiber mats produced by a slot die was measured. The vibration amplitude of fibers during the melt blowing process was measured photographically. It was found that the jets studied act largely as variations of classical circular and rectangular jets. For all the jets studied, it was found that the far field decay coefficient was higher for melt blowing jets than for the classical jet geometries. Accurate computational techniques were developed for both annular and swirl nozzle geometries.

Experimental and Computational Studies of the Aerodynamics of Melt Blowing Dies

Chapter 1

Introduction

1.1 Melt Blowing and Its Application

Melt blowing is a method for producing fine fibers from thermoplastics using the drag of a high velocity gas, typically air, as the attenuating method. Melt blowing was initially developed by Wente through work at the Naval Research Laboratory (Wente, 1956). The fibers are produced as a semi-random mat, not spun into threads or directly woven into fabrics. Because of this, melt blown materials are classified as nonwovens. Melt blown fibers are generally of very small diameter, with 0.5 to 50

microns being typical. Applications for melt blown fibers include: filtration media, thermal insulation, absorptive wipes, and personal hygiene products. Melt blown fabrics are typically made from synthetic high polymers, mostly polyolefins, however they can be made from natural polymers such as starch (Bailey et al., 2004).

Melt blowing is accomplished using specifically designed dies, with one or more polymer orifices surrounded by one or more air orifices. A diagram of the melt blowing process is shown in Figure 1.1. Molten polymer and heated air are fed to their respective orifices. At the die face, the air and polymer meet, where the drag of the blowing air attenuates the polymer. At some distance below the die is the collection mechanism, typically a moving screen, which collects the attenuated fibers into a web. After collection the webs are either used directly or further processed into finished products. Various designs for melt blowing dies exist, with slot and annular die configurations being the most common. Slot dies, as shown in Figure 1.2, use a row of polymer capillaries blown using two parallel converging rectangular air jets, parallel to the row of capillaries (Harding et al., 1974). Annular dies, commonly attributed to Schwarz (1983), use groups of polymer capillaries, each surrounded by a single annular jet, see Figure 1.3. While much of the research work done is based on a single polymer capillary, it is important to note that commercial melt blowing dies are typically used in large groups. Commercial dies often consist of thousands of polymer capillaries integrated into a single die assembly.

A unique class of melt blowing dies is swirl nozzles, shown in Figure 1.4. Swirl nozzles are melt blowing dies designed to deposit adhesive onto a surface in a specific pattern using the air jets to control the deposition. Unlike conventional melt

blowing, where the air primarily serves to attenuate the polymer, the jets in a swirl nozzle are primarily to control the deposition pattern of the adhesive. Even though the applications of adhesive nozzles and conventional melt blowing dies are the different the underlying principles of operation are very similar. The deposition is based on the vibration of the adhesive stream in response to the blowing air.

1.2 Turbulent Free Jets and Melt Blowing

Free turbulent jets are one of the classical problems of turbulent fluid flow. With analytical and experimental studies dating to the 1920s, it is one of the most studied problems in fluid dynamics. Even with almost eighty years of nearly continuous research, most of the problems solved are based on relatively simple geometries, such as circular, planar and rectangular jets. Melt blowing provides several complications, including: multiple interacting jets, compressible flow, high temperatures, and small dimensions. Despite the added complexity, the fundamental principles of turbulent jets flow still apply to the melt blowing process. Schlichting (1979), in his classic text, gives analytical and experimental results for simpler turbulent jet geometries. Solutions for the flow fields of circular and planar free jets are given, and match very well with experimental data.

Several researchers (Uyttendaele and Shambaugh 1989, Majumdar and Shambaugh 1991, Harpham and Shambaugh 1996, Tate and Shambaugh 1998) have collected experimental data on the flow behavior of melt blowing dies. The common conclusion reached across the works is that in the far field (i.e. large distances from the die) melt blowing jets behave similarly to the simpler, well-studied jets. That is

not to say that melt blowing jets behave exactly as other jets. Often there are differences, most notably the far field decay and spreading of melt blowing jets is often faster than the equivalent simple jet geometry. The near field behavior of melt blowing jets most differentiates it from simpler jet. Converging and merging jets create complex flow fields that are not easily correlated. Most of the past research done on melt blowing jets has been done on laboratory scale dies and relatively low velocities; this work will provide measurements and simulations on a much larger scale and at typical commercial operating speeds.

1.3 Application of CFD to Melt Blowing Jets

The application of computational fluid dynamics (CFD) to melt blowing processes is a relatively new development. The work of Krutka, Shambaugh and Papavassiliou (2002, 2003) studied slot dies as a two dimensional problem and developed a technique that matched experimental data. Mukhopadhyay et al., (2002) applied the Large Eddy Simulation (LES) technique to slot dies, however their results were not verified against any experimental data. The present work expands and extends the application of CFD to annular and swirl nozzle geometries.

1.4 Online Measurement of Fibers During Melt Blowing

The measurement of the diameter of fibers during the melt blowing process is not a trivial task. Previous works by Bansal and Shambaugh (1997) have looked at the online diameter and vibration of melt blowing at the laboratory scale. However Bansal and Shambaugh's work was limited to fairly low velocities, approximately an

order of magnitude below the normal operating speed of a melt blowing die. At these increased speeds, the photographic techniques used by Bansal and Shambaugh lose their effectiveness. In a work by Yin et al., (1999), full-speed melt blowing fibers were successfully photographed using pulse laser illumination, on-line diameter measurements were still not possible more than 0.3 inches from the die face. Work in developing diameter profiles for industrial melt blowing conditions has been done by varying collector distance, which inherently interferes with the process. This work will explore the ability of the new Ensemble Laser Diffraction (ELD) technique to measure the diameter distribution within a fiber curtain during the melt blowing process. This technique is a non-intrusive technique for determining the diameter distribution based on the scattering of laser light that passes through a group of fibers within the fiber curtain.

1.5 Objectives

There are two primary objectives to this work. The first is to develop a set of techniques that allow for the quantitative simulation of melt blowing jets. The second is to collect aerodynamic and operating data on different dies for validation of future CFD simulations and fiber dynamics modeling. These two objectives relate to each other directly, as any model, CFD or otherwise, applied to melt blowing processes should be correlated to actual experimental data on melt blowing processes.

Both objectives are extensions of previous works, carried to the next logical step. The experimental data taken encompasses the commercial operating ranges for both a slot die and a swirl nozzle. Some researchers (Yin et al., 1999; Yin et al., 2000;

Bresee and Ko, 2003) have published limited operating data on commercial slot dies, however, no detailed aerodynamic analysis of full scale melt blowing dies has been published to date. No known aerodynamic study of any type has been published relating to swirl nozzles.

1.6 A Note on Formatting

Each of the main chapters of this book, Chapter Two through Chapter Six, are written for publication separately. The publication details for each chapter are listed on the first page of that chapter. As such, each chapter also contains a brief introduction of its own. It is hoped that the reader will understand the necessity of this and forgive the small amount of repetition.

1.7 References

Bailey, V.A.; Mackey, L.N.; Trokhan, P.D. "Melt Processable Starch Compositions", United States Patent 6,709,526, **2004**.

Bansal, V.; Shambaugh, R.L. "Online Determination of Diameter and Temperature During Melt Blowing of Polymer Fibers.", *Ind. Eng. Chem. Res.*, **1998**, *37*, 1799-1806.

Bresee, R.; Ko, W. "Fiber Formation During Melt Blowing", *Int. Nonwovens J.*, **2003**, 12(2), 21-28.

Harding, J.W.; Keller, J.P.; Buntin, R.R. "Melt Blowing Dies for Producing Non-woven Mats", United States Patent 3,825,380, **1974**.

Harding, J.W.; Keller, J.P.; Buntin, R.R. "Melt-blowing die for producing nonwoven mats.", U.S. Patent 3,825,527, **1974**.

Harpham, A.; Shambaugh, R.L. "Flow Field of Practical Dual Rectangular Jets", *Ind. Eng. Chem. Res.*, **1996**, *35*, 3776-3781.

Krutka, H.; Shambaugh, R.L.; Papavassiliou, D.V. "Analysis of a Melt Blowing Die: Comparison of CFD and Experiments", *Ind. Eng. Chem. Res.* **2002**, *41*, 5125-5138.

Krutka, H. M.; Shambaugh, R. L.; Papavassiliou, D. V., "Effects of Die Geometry on the Flow Field of the Melt Blowing Process", *Ind. Eng. Chem. Res*. **2003**, *42*(22), 5541-5553.

Majumdar, B.; Shambaugh, R.L. "Velocity and Temperature Fields of Annular Jets", *Ind. Eng. Chem. Res.* **1991**, *30*, 1300-1306.

Mukhopadhyay, A.; Prasad, R.O.S.; Grald, J. Sun; Lifshutz, N.; "Performance Analysis of Melt-blown Dies Using Computational Fluid Dynamics", Proceedings of INTC 2002 Conference, Atlanta, GA, USA, September 25-26, **2002**.

Schlichting, H. Boundary Layer Theory, 7th Ed., McGraw Hill, **1979**, pp. 729-752.

Schwarz, E.C.A. "Apparatus and Process for Melt-Blowing a Fiberforming Thermoplastic Polymer and Product Produced Thereby", U.S. Patent 4,380,570, **1983**.

Tate, B.D.; Shambaugh, R.L. "Modified Dual Rectangular Jets for Fiber Production", *Ind. Eng. Chem. Res.*, **1998**, *37*, 3772-3779.

Uyttendaele, M.A.J.; Shambaugh, R.L. “The Flow Field of Annular Jets at Moderate Reynolds Numbers”, *Ind. Eng. Chem. Res.* **1989**, *28*, 1735-1740.

Wente, V.A.; “Superfine Thermoplasic Fibers”, *Ind. Eng. Chem. Res*, **1956**, *8*, 1342-1346.

Yin, H.; Yan, Z.; Bresee, R.R. “Experimental Study of the Melt Blowing Process”, *Int. Nonwovens J.*, **1999**, *8*(1), 60-65.

Yin, H.; Yan, Z.; Ko, W.; Bresee, R. “Fundamental Description of the Melt Blowing Process”, *Int. Nonwovens J.*, **2000**, 9(4), 25-28.

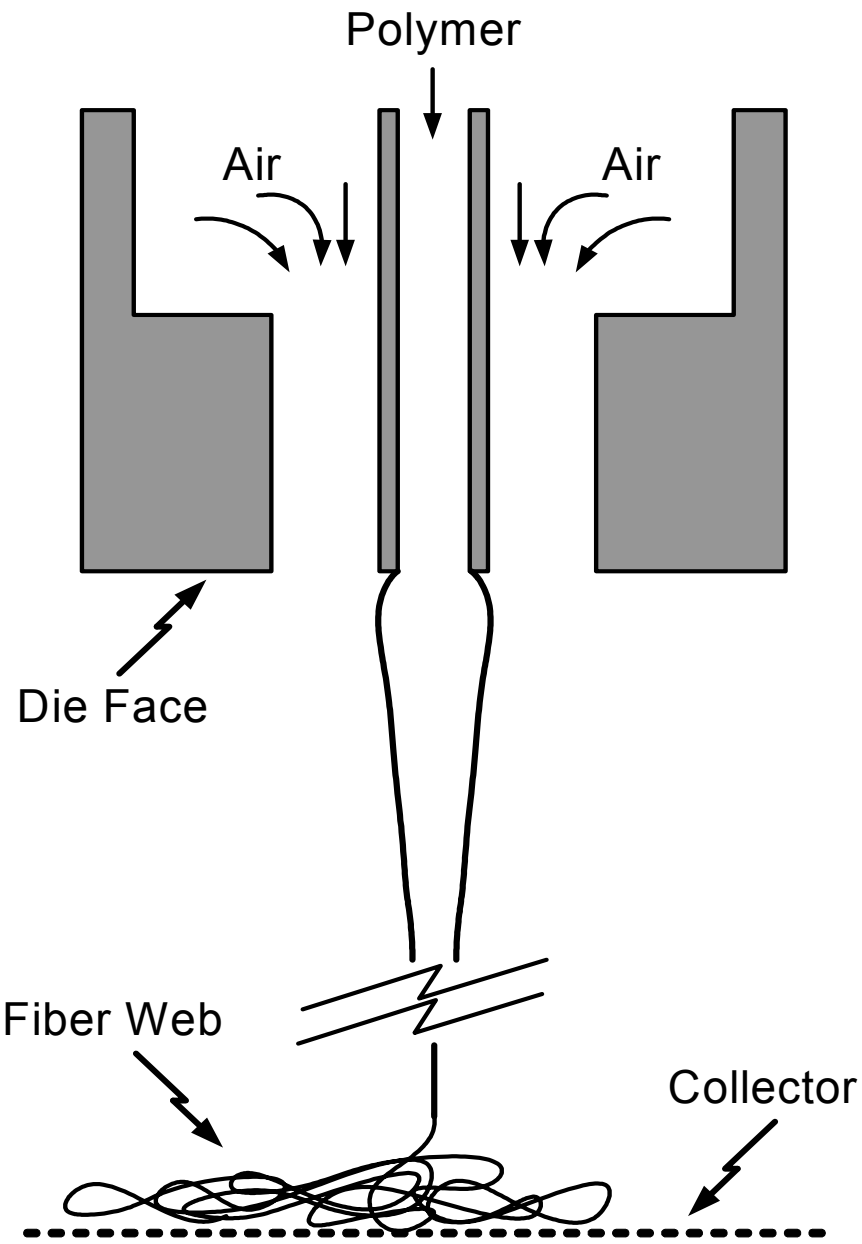

Figure 1.1. Diagram of the melt blowing process.

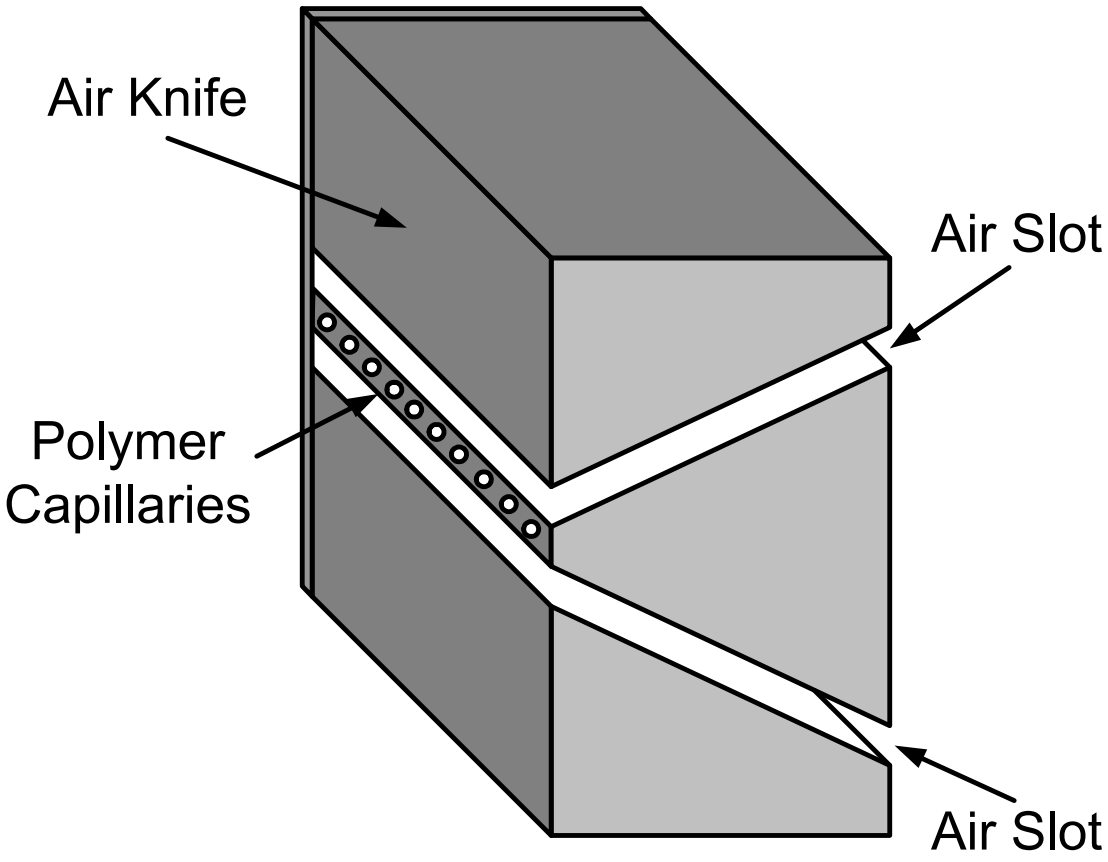

Figure 1.2. Cut away view of a slot melt blowing die.

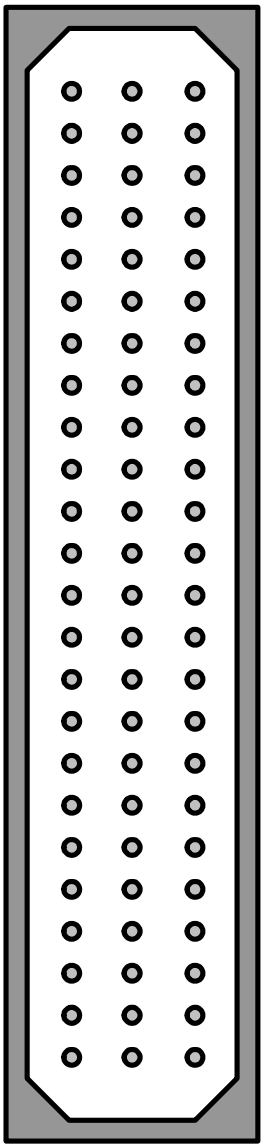

Figure 1.3. End on view of a multi-hole annular melt blowing die.

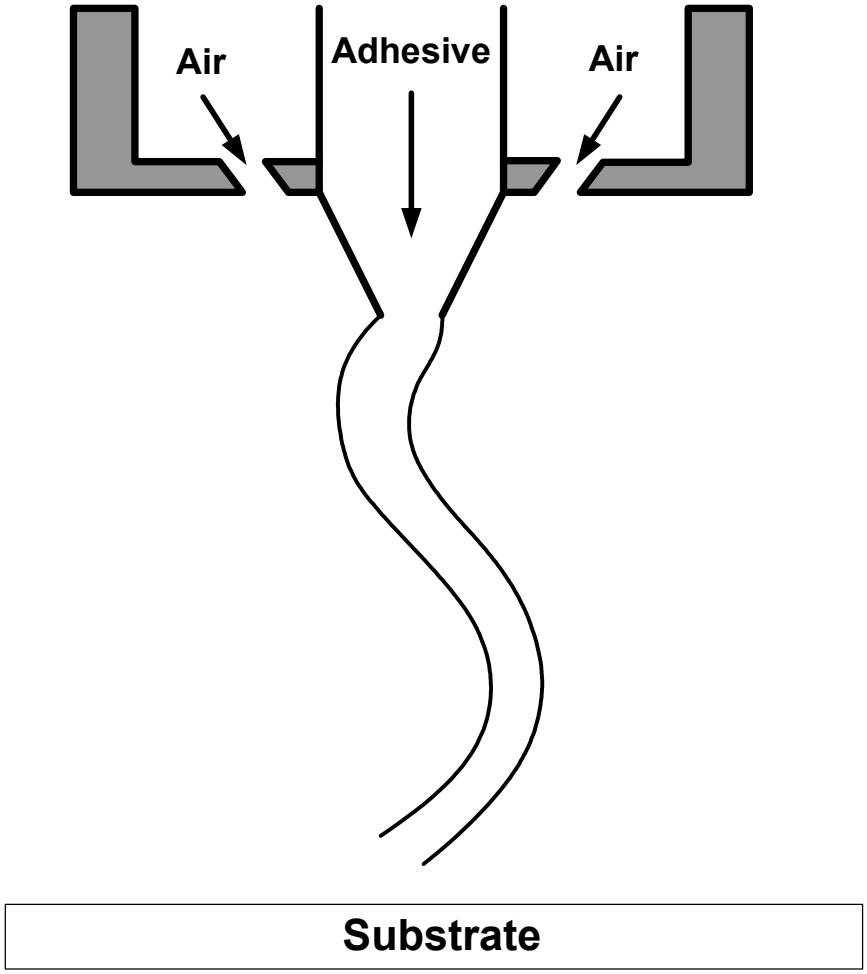

Figure 1.4. Diagram of a swirl deposition process.

Chapter 2

Analysis of Isothermal Annular Jets: Comparison of CFD and Experimental Data

(This chapter has been accepted for publication in Journal of Applied Polymer Science as: Moore, E.M., Papavassiliou, D.V., Shambaugh, R.L. "Analysis of Isothermal Annular Jets: Comparison of CFD and Experimental Data")

2.1 Abstract

A computational fluid dynamics model was developed for the simulation of airflow through an annular jet. The model was based on the Reynolds stress model for the simulation of turbulent flows, and the parameters were calibrated using available experimental data for circular and annular jets. It was found that, after this

calibration, the computational results agreed well with experimental data (specifically, with the velocity magnitude, velocity decay rate, and the velocity spreading rate). The jet geometry studied was based on industrial melt blowing nozzles. The velocities studied varied from the low subsonic incompressible range to nearly sonic conditions. Based on both the computational and experimental results, a correlation was proposed that predicts the centerline velocity profiles in both the near and far field regions.

2.2 Introduction

Melt blowing is a process for manufacturing polymer fibers. In melt blowing, streams of hot gases (usually air) attenuate a molten polymer stream into a fine fiber. The fibers are generally collected as a mat upon an open screen and that fiber mat is referred to as a nonwoven structure. There are different die geometries that are used to create melt blown fibers. The two most commonly used dies are slot dies (commonly called Exxon dies; see Harding et al., 1974) and annular dies (often called Schwarz dies; see Schwarz, 1983). Slot dies are dies where the air is sent through a pair of long linear slots located on opposite sides of a row of polymer outlets. Typically, the air slots are of the order of 1 mm wide, and the two slots are located about 1 mm apart; however, the length of a slot die is about 0.5 to 3 meters. Annular dies are dies where a single annular air outlet surrounds each polymer outlet; generally, there are several rows (3 to 5) of polymer outlets. A diagram of one hole of an annular melt blowing die is pictured in Figure 2.1. Annular melt blowing dies typically have inner (air) diameters of around 1 mm and outer (air) diameters of about 2 mm.

Recently, slot dies have been studied with a combination of computational fluid dynamics (CFD) analysis and comparison to experimental data (Krutka et al., 2002; Krutka et al., 2003); slot dies have also been studied with a large eddy simulation approach (Mukhopadhyay et al., 2002). Krutka et al. (2002) found that the default turbulence model parameters - the parameters suggested within the software (Fluent Inc., 2003) - need to be modified in order to obtain agreement between the CFD results and experiments. The present study explores the development of a CFD model for various flowrates of isothermal air emanating from an annular orifice. The goal is to develop a method for investigating annular melt blowing dies without going through the considerable expense of constructing and testing physical dies. The model is calibrated against the annular jet experimental data of Uyttendaele and Shambaugh (1989) as well as other experimental data on circular jets (Obot et al., 1986).

The efficiency of the melt blowing process depends upon the behavior of both the air flow field and the polymer stream. The analysis performed here is focused on the air flow field and does not include the effects of the polymer on the air flow field. This approximation is consistent with available experimental data and with models already developed for the melt blowing process (Rao and Shambaugh, 1993; Marla and Shambaugh, 2003). This decoupling of the air and polymer flow leads to a significant reduction in computational and modeling effort, while providing a valuable tool for process development. The implicit assumption, when decoupling the air and polymer flow fields, is that the polymer stream has a small effect on the air flow field. Due to the rapid attenuation and small diameters of the fibers involved,

this appears to be a good approximation when the fibers are beyond the immediate vicinity of the die face (where the fiber diameter is quite large) and away from the fiber collection device (since the collection device can interfere with the air flow pattern).

Circular jets have been studied extensively; however, much less work has been done with annular jets. Schlichting (1979) presents a theoretical analysis of turbulent circular jets. Ferdman et al. (2000) reported that the far field development of circular turbulent jets is independent of the initial jet velocity profile. This result suggests that annular jets may, at least in the far field region, behave in a manner similar to a turbulent circular jet.

The contributions of the present paper are (a) the determination of the turbulence model parameters that need to be used for the successful simulation of an annular air jet, (b) the development of predictive correlations that describe the behavior of the mean air velocity field in annular jets used for melt blowing, and (c) the prediction of turbulence quantities below annular air jets.

2.3 Methodology

2.3.1 Computational Domain and Grid Generation

The seven different types of dies simulated in this work included a circular jet and six different annular jets. The first four dies are referred to as Die A, Die B1 (the circular jet), Die B3 and Die B5; this nomenclature is consistent with Majumdar and Shambaugh's work (1991). Experimental data are available for these four dies (Uyttendaele and Shambaugh, 1989; Majumdar and Shambaugh, 1991). The remaining three computational dies are referred to as Die C, Die D, and Die E. For

all seven dies, the outer diameters vary from 1.25 mm (Die C) to 3.5 mm (Die E). Inner diameters vary from zero (Die B1) to 2.25 mm (Die D). Table 2.1 shows the dimensions of all the dies studied in this work. It is important to note that Die B1 is a circular die used to compare the behavior of a circular jet to an annular jet with the same outer diameter (Die B3). The experimental orifices had different inlet lengths ("L" on Figure 2.1) that ranged from 2.70 mm to 9.36 mm; however, it was experimentally determined that, over the inlet length range used, the length had little effect on the jet development (Uyttendaele and Shambaugh, 1989). Other researchers (Obot et al., 1984; Obot et al., 1986) found that inlet length does have an effect on jet development in circular jets, but only when inlet lengths are higher than those used in the experimental work of Uyttendaele and Shambaugh (our simulations used lengths of the order of those used by Uyttendaele and Shambaugh).

In our present work, the computational grid was created with a 5 mm inlet length, and the starting velocity profile was assumed to be flat (plug flow). The software used for the CFD calculations was Fluent® Version 6 from Fluent, Incorporated. In order to develop a model for the annular jet flow, a proper computational domain and grid was developed (using Gambit®, which is also from Fluent, Inc). The coordinate system origin was placed in the plane of the die face and at the center of the annulus. The positive y (axial) axis was aligned with the dominant flow and the x (radial) axis was perpendicular to the y axis; see Figure 2.2. Since the flow geometry involved axisymmetric flow, the Fluent® axisymmetric solver was used. This solver mechanism employs a two-dimensional grid to model the three-dimensional jet using the inherent axial symmetry of the problem. This two

dimensional grid greatly reduced the computation time necessary for convergence. The computational domain was defined as a frustum with dimensions sufficient to bound the jet over the region of jet development. In the vertical (y) direction, the domain ran from the jet inlet and on into the fully developed region. Based on the experimental measurements of Uyttendaele and Shambaugh (1989), the overall length of the computational grid was 75 mm (5 mm for the inlet region plus 70 mm for the jet region). In the x direction (the radial direction as shown in Figure 2.2), the experimental measurements of Uyttendaele and Shambaugh were also used to define the active zone of jet development: the upper surface containing the orifice was given a radius of 5 mm, and the radius of the lower surface was set at 20 mm. Uyttendaele and Shambaugh did their experimental measurements of air flow without the presence of a fine polymer stream (see Fig. 2.1). Likewise, in our simulations we ignored the presence of a polymer stream.

The inlet to the region (at the far left of Fig. 2.2) was defined as a mass flow inlet; the "height" of this inlet was only $(D_o - D_i)/2$. The two outlets (shown as "radial outlet" and "axial outlet" on Fig. 2.2) were defined as pressure outlets at atmospheric conditions. The upper (located at the left in Fig. 2.2) surfaces - both the inlet walls and inlet face - were defined as solid walls. The air was modeled as an ideal gas with constant viscosity. At the relatively low pressures involved in the simulation, the ideal gas model adequately accounts for compressibility. Constant viscosity was assumed due to the nearly isothermal nature of the flow. Since an ideal gas model was used, energy boundary conditions had to be specified also. All walls and outlets were defined at a constant 300K, with the inlet total temperature was

defined such that the static temperature of the inlet air was 300K. It is important to note that the flow solution is not entirely isothermal. Near the jet inlet there are some thermal variations due to both the viscous dissipation and the expansion of the air as it exits the inlet. At higher flow rates these changes become larger due to the increased inlet pressure of the air and increased velocity gradients present in the flow.

A grid consisting of rectangular cells was developed to provide accurate answers within reasonable computational time. Grid generation was handled by the Gambit® program from Fluent, Inc. A cell count of approximately 58,000 cells was found to be large enough to guarantee grid independence. For the different dies, the number of cells within each grid was slightly different due to the different die geometries. Table 2.1 lists the number of cells used in each grid. Grid generation was done by first creating an initial coarse grid; then, the grid was refined in the region closest to the jet orifice. The refinement was done throughout the inlet and on all cells up to 15 mm away from the die face for the entire width of the domain. Figure 2.3 shows one of the grids used. In order to test for grid dependence, a case was run on a grid that had been refined across the entire computational domain. This test grid had 235,400 cells. The centerline velocity profile predicted with these 235,400 cells was compared to the velocity profile predicted with only 58,850 cells; see Figure 2.4. Since the difference between the two predictions is very small (largest difference was 2% with most of the differences much smaller), the coarser grid was deemed adequate.

Simulations with four different air inlet flow rates were conducted (0.125 g/s, 0.25 g/s, 0.50 g/s, and 1.0 g/s). These flow rates corresponded to nominal velocities

of 30.1 to 289.1 m/s (nominal velocity is defined as the flow rate divided by the cross sectional area of the annular inlet). The flow rates were chosen such that the flow remained subsonic (the speed of sound in dry air at 21°C and 101 kPa is 343.9 m/s). However, the air flows were high enough so that different levels of compressible behavior could be observed for each die. Table 2.2 lists the specific flow rate and die combinations used.

2.3.2 Turbulence Modeling and Determination of Model Parameters

The Reynolds stress model (RSM; see Launder, Reece, and Rodi, 1975) was chosen as the turbulence model for this study. For stationary state and isothermal conditions, the RSM model equation for the transport of Reynolds stresses is given by (Durbin and Petterson Reif, 2001; Fluent User's Manual, 2003)

$$\frac{\partial}{\partial x_k}(\rho U_k \overline{u_i u_j}) = -\frac{\partial}{\partial x_k}\left[\rho\overline{u_i u_j u_k} + \overline{p(\delta_{kj}u_i + \delta_{ik}u_j)}\right] + \frac{\partial}{\partial x_k}\left[\mu\frac{\partial}{\partial x_k}(\overline{u_i u_j})\right] - \rho\left(\overline{u_i u_k}\frac{\partial U_j}{\partial x_k} + \overline{u_j u_k}\frac{\partial U_i}{\partial x_k}\right) + \overline{p\left(\frac{\partial u_i}{\partial x_j} + \frac{\partial u_j}{\partial x_i}\right)} - 2\mu\overline{\frac{\partial u_i}{\partial x_k}\frac{\partial u_j}{\partial x_k}} \quad (1)$$

The summation convention is used in the above equation. In addition to the Reynolds stress transport equations, the dissipation rate is modeled by the dissipation equation in the standard *k*-ε model

$$\rho\frac{D\varepsilon}{Dt} = \frac{\partial}{\partial x_i}\left[\left(\mu + \frac{\mu_t}{\sigma_\varepsilon}\right)\frac{\partial\varepsilon}{\partial x_i}\right] + C_{1\varepsilon}\frac{\varepsilon}{k}G_k - C_{2\varepsilon}\rho\frac{\varepsilon^2}{k} \quad (2)$$

Krutka et al. (2002) found in a study of slot melt blowing dies that the RSM model was more accurate than the *k*-ε model for modeling the behavior of dual slot jets. Our simulations of annular dies were tested with the Krutka et al. (2002) parameters

(which were developed for slot dies). With the Krutka parameters, the simulated annular mean centerline velocity profiles matched the experimental data from annular dies; however, the velocity spreading rates did not match. In fact, the simulated spreading rate was found to be approximately twice that of the experimentally determined spreading rate. Consequently, a study of the effects of different model parameters was undertaken. After testing several different parameter combinations, it was found that changing the value of $C_{2\varepsilon}$ to 1.82 produced the best fit to the experimental velocity correlations proposed by Uyttendaele and Shambaugh (1989). Our $C_{2\varepsilon}$ value of 1.82 is slightly lower than the Fluent default value of 1.92, while the $C_{2\varepsilon}$ value suggested by Krutka et al. is 2.05. In the RSM turbulence model, as well as the standard *k*-ε model, $C_{2\varepsilon}$ is a constant that controls the magnitude of the rate of dissipation of turbulent energy (see Equation 2).

In summary, for the RSM model, Fluent recommends the following default values for the nine fitting parameters: $C_{\mu} = 0.09$, $C_{1ps} = 1.8$, $C_{2ps} = 0.6$, $C'_{1ps} = 0.5$, $C'_{2ps} = 0.3$, $\sigma_k = 1$, $\sigma_{\varepsilon} = 1.3$, $C_{1\varepsilon} = 1.44$, and $C_{2\varepsilon} = 1.92$. Krutka et al. (2002; 2003) used the first seven of these default parameters. However, they found that changing $C_{1\varepsilon}$ and $C_{2\varepsilon}$ to 1.24 and 2.05, respectively, was necessary to produce a good simulation (based on experimental results) of slot dies used for melt blowing. For our work on the simulation of annular melt blowing dies, we used eight of the nine parameters used by Krutka et al. However, we had to change $C_{2\varepsilon}$ to 1.82 to produce a good match of the simulation to experimental results. Figure 2.5 shows a comparison of the centerline velocity calculated using different turbulence model parameters; also shown is the correlation produced by Uyttendaele and Shambaugh from actual

experiments with a die of identical geometry. Figure 2.6 shows the simulated velocity half-widths for the same turbulence model parameters; the correlation suggested by Uyttendaele and Shambaugh is also shown. The velocity half-width, $x_{1/2}$, is the distance from the jet centerline at which the velocity becomes half of its value at the centerline (i.e., $V(x_{1/2},y)=1/2*V_o(0,y)$). The rate of change of $x_{1/2}$ with y is the spreading rate of the jet velocity field. Using $C_{2\varepsilon}=1.82$ allows us to match correlations (i.e., experimental data) with both the simulated mean centerline velocity and the simulated spreading rate better than using the default model parameters.

Computationally, the CFD analyses discussed here are not expensive. A single run (i.e., the simulation of one die at one flowrate) was completed in about 12 to 18 hours using dual 2.2 GHz Xeon processors and approximately 200 megabytes of primary memory.

2.4 Results

2.4.1 Centerline Velocity Correlation

The development of the flow field downstream from an annular jet exhibits three major zones. First, closest to the orifice, is the converging zone where the jet is still annular in shape. The dominant characteristic of this zone is the presence of a recirculation area where flow is traveling in the opposite direction from the main direction of the jet. The merging zone is next; this is a transition between the converging zone and the fully developed region. The dominant characteristics of the merging zone are the lack of a recirculation area and the presence of peak velocities away from the centerline. The final region is the well-developed region, where the

velocity maximum is along the centerline, and the velocity is decaying. Figure 2.7 shows a diagram of the three zones; Nasr and Lai (1997) showed similar zones for parallel jet flow. Figure 2.8 shows the centerline profile (for Die A run with a high air throughput) with these three zones highlighted. Tanaka (1970, 1974) first reported on and described these three zones for the flow of parallel plane jets. In Figure 2.8, the point where the centerline velocity crosses from a negative to a positive value is called the merging point; the point where the maximum centerline velocity is reached is called the combined point. These two points were defined by Lai and Nasr (1998).

In order to better study the centerline velocity profiles, a proper frame of reference is needed to correlate data from various flow rates and flow geometries. In particular, to develop a dimensionless description of the jet behavior, the determination of characteristic scales is needed. The peak centerline velocity (see Figure 2.5) was used as the characteristic velocity for the scaling of the centerline velocity. The distance along the centerline from the die face to the point where maximum velocity occurs (i.e., the convergence distance, Z_{max}) was picked to be the characteristic length. The velocity at this point was defined as V_{max}. Note that this is not the maximum velocity in the entire flow field. Rather, it is the maximum centerline velocity.

In order to describe the geometry of the jet orifice, three geometric parameters were used. The first parameter is D_o, the outer diameter of the annular opening; the second parameter is D_i, the inner diameter of the annular opening. The third parameter is the fraction open area, FOA, which is defined as follows:

$$FOA = \frac{D_o^{\,2} - D_i^{\,2}}{D_o^{\,2}} \tag{3}$$

The fraction open area is used as a measure of the available flow area versus the flow area of a circular jet with diameter D_o.

In order to predict the centerline velocity behavior of an annular jet, an empirical model was developed. Through variations of inlet velocity, outer diameter, and FOA, a number of different velocity profiles were obtained. These differing velocity profiles served as the basis for developing a universal centerline mean velocity profile. From the computed velocity profiles it was apparent that no simple correlation (e.g., linear, exponential, etc.) could model the behavior of all the variables involved. A slightly more complex correlation was developed using the following equations:

$$V / V_{max} = F(Z / Z_{max}) \tag{4}$$

$$Z_{max} / D_o = G(FOA, V_o / V_{sound}) \tag{5}$$

$$V_{max} / V_{sound} = H(FOA, V_o / V_{sound}) \tag{6}$$

In order to determine the mathematical forms for the functions F, G, and H, regression was used based on all the computational cases tested. This analysis showed that the circular die (Die B1) had significantly different behavior than the other dies. Therefore, the regression is only valid for the case of annular dies. Regression showed that no simple equation could describe the velocity profile over the entire flow range. The flow field was separated at the point where $V = V_{max}$ (the "combined point" in Figure 2.8), and the two regions were fitted to two different equations. The far-field flow region, where the annular jet is similar to circular jets,

was approximated using an inverse linear relationship, since such a function has been found to describe the decay of centerline mean velocity for circular jets (Schlichting, 1979). The second region -- the complex near-field flow area -- includes both the converging and merging regions. The fitted equations for these regions are

$$\frac{V}{V_{\max}} = c_1 + \frac{c_2}{\dfrac{Z}{Z_{\max}}} \qquad \text{for } Z / Z_{\max} > 1 \tag{7}$$

and

$$\frac{V}{V_{\max}} = ax + bx^2 + cx^3 + dx^4 + ex^5 + fx^6 + gx^7 + hx^8 + ix^9 + jx^{10} \qquad \text{for } Z / Z_{\max} < 1 \tag{8}$$

with G defined as

$$\frac{Z_{\max}}{D_o} = \frac{1}{\alpha + \beta FOA^2 + \gamma FOA^3} \tag{9}$$

and H defined as

$$\frac{V_{\max}}{V_{sound}} = \frac{1}{A + B \cdot \left(FOA^2 \cdot \ln(FOA)\right) + C\left(\ln(Ma_o)^2\right)} \tag{10}$$

The values for the regression constants are given in Table 2.3. Figure 2.9 is an example of how well this empirical model can predict the centerline axial velocity for an annular die for the entire range of y values (die face to far field). Figure 2.9 shows results for die B3; results are similar for the other die geometries shown in Table 2.1. As the reader can see, the match between the correlation and the experiments is excellent. While theoretical models do exist for the far field region of flow, very few exist for the important, high velocity region nearest to the die. Observe that the form

for far field flow is similar to that suggested by Schlichting (1979) for the centerline velocity decay of a circular jet.

2.4.2 Velocity Spreading and Horizontal Velocity Profile

An important part of modeling the behavior of turbulent jets is capturing the mean velocity spreading rate. The spreading rate is largely dependent on the turbulent transport of momentum away from the jet and the entrainment of additional air mass into the jet from the adjacent quiescent air.

As discussed in section 2.2, the spreading of a turbulent jet is usually characterized by the jet velocity half-width, $x_{1/2}$. The half-width increases with increasing distance from the jet source. Within the well-developed region the growth of the jet is linear (Schlichting, 1979). The slope and intercept of this line are measurable characteristics of the jet. For our work both half-width and distance from the die were non-dimensionalized using the outer diameter of the die.

The jet spreading rate was calculated for each simulation. In order to determine the spreading rate constants, the region from $y/D_o = 10$ to the end of the computational domain was used. In every case the velocity half-width varied linearly with position in the well-developed region. Figure 2.10 shows a typical example (for die A). It was found that the spreading rate was nearly constant for every case run, including the circular die case (die B1). Table 2.4 lists the seven dies and the gas flow rates run for each die. The slope and intercept for each of the 19 simulations are listed on the table. The average slope, average intercept, and standard deviations for each die are shown in the last 4 columns, and the total averages for all the dies are shown at the bottom of the last 4 columns. A plot of this total average (slope =

0.1139 and intercept = -0.4243) is shown in Figure 2.11. This average slope is a good representation of our simulations: as Table 2.4 shows, the overall standard deviation of the slope is only 0.0036. Also shown on Figure 2.11 are the experimentally determined correlations of four groups of researchers. Our average slope compares well with the experimental work of Majumdar and Shambaugh (1991); they reported a slope of 0.112 and an intercept of 0.040. Uyttendaele and Shambaugh (1989) and Obot et al., (1984; 1986) both reported lower values (0.077 to 0.097) for the slope, but they forced the intercept to be zero. With a fixed zero intercept, our data produce an average slope of 0.0935, which is actually within the range given by Obot et al. (1984) for circular jets with various inlet geometries. [If we use the FLUENT default turbulent model parameters (curve not shown of Fig. 2.11), we will produce a line with a slope of 0.146 and an intercept of –0.5528; the fit of this curve to the experimental data is not good.] Discrepancy in the jet spreading correlation is not an unusual occurrence. Kotsovinos (1976) reviewed several different works that reported different values for both the slope and intercept of the half-width correlation in plane jets.

As Table 2.4 shows, there is significantly more variance in the intercept than with the slope. Though the overall standard deviation for the slope was only 0.0036, or 3.2 percent, the intercept had a much larger overall standard deviation of 0.0489, or 11.5 percent. For a given die geometry our data shows that the slope decreases, and the intercept increases, with increasing inlet flow rate. However, when comparing the different die geometries, there is no discernable pattern in the slope or intercept with respect to either inlet velocity or outer die diameter.

2.4.3 Turbulence

The measurement of turbulence quantities is of importance to the melt blowing process. Strong velocity fluctuations can lead to operating problems, such as the fiber sticking to the die face or the entangling of the newly formed fiber with itself or with adjacent fibers. For very small volumes, such as the near field region of an annular die, the experimental measurement of turbulence quantities can be difficult. However, regardless of the volume considered, simulations can provide information on the state of turbulence within the flow.

The turbulent kinetic energy (k or TKE) is a measure of the kinetic energy associated with the fluctuations of the velocity; TKE is an output of the Fluent simulations. Figure 2.12 shows centerline TKE (nondimensionalized) for Die A at three gas flows. The profiles have a two-peaked shape. The first peak approximately corresponds to the location where the flow reversal ends (see Fig. 2.7). The second peak corresponds to the region where the centerline velocity is decreasing quickly. For Die A run at 0.25 g/s air flow, Figure 2.13 shows an overlay of centerline TKE and centerline velocity. The local minimum between the TKE peaks corresponds to the area of highest velocity. Past the second peak, both the TKE and the centerline velocity profile decay. The generation of TKE is proportional to the velocity gradient, so that the areas of highest TKE are also the areas of highest velocity gradient.

It is apparent from Figure 2.12 that, for Die A, the inlet air flow rate influences both the peak magnitude and the general shape of the curve. The other die geometries show similar results. It appears that this change in the dimensionless TKE

is due to the growing effects of compressibility on the flow as inlet flow rates increase. With our simulated peak velocities transitioning from the generally accepted incompressible flow regime (v < Mach 0.3) to a compressible regime, this is a reasonable hypothesis to make. (The 0.25 g/s, 0.5 g/s, and 1.00 g/s flowrates on Figure 2.12 correspond to Mach 0.20, 0.40, and 0.80, respectively.) As Figure 2.12 shows, the peak velocity location and the areas of high velocity gradient move away from the die at higher inlet flow rates. Lau (1981) reported that the potential core for compressible circular jets stretches with increasing Mach number. This stretching of the potential core moves the start of velocity decay, and the position of velocity maximum, away from the die face. Thus, it is reasonable to expect that the location of the second TKE peak will move away from the die at higher inlet flow rates.

For a given die it is possible to generalize the shape of the TKE curve. For this generalization, TKE is nondimensionalized with SMK, the maximum TKE at the location of the second peak. The abscissa value is nondimensionalized with SMP, the second maximum peak position. With this normalization, the curves for a single die match well. Figure 2.14 shows this type of plot for die A. The normalized plots for the other dies look similar to Figure 2.14. Specifically, the curves for the different airflow rates (for a specific die) are coincident.

The circular die case, die B1, has a significantly different centerline TKE profile than die A. This is due to the lack of an inner wall and the resulting shear on the flow. Even at very high open areas (e.g., see die E in Table 2.1), the annular jet turbulence profile is significantly different than that of the circular jet. Figure 2.15 shows centerline TKE plots for dies A, B1 and E at an air flow rate of 0.25 g/s. These

results suggest that the hypothesis that annular jets can be treated merely as variations on turbulent circular jets is not entirely valid. The presence of the inner wall has a significant effect on the turbulence properties throughout the flow, because it is an additional surface of high shear that generates additional turbulence velocity fluctuations. Figure 2.16 shows the Reynolds stresses along the centerline for die A at an air flow of 0.25 g/s. It is apparent that the three Reynolds stress curves are different both in shape and magnitude. (There are only three significant Reynolds stresses due to the axisymmetric model used for the flow.) The large differences in the Reynolds stresses are an indication that the turbulent flow is anisotropic. The popular k-ε turbulence models, as well as the similar k-ω model, both make the assumption of isotropic turbulence (Durbin and Petterson Reif, 2001). It has been shown that the k-ε model is not particularly well suited to the flow of turbulent free jets (Krutka et al., 2002; Pope 2000). The present work (with the RSM model) suggests that the real flow may have significant turbulent anisotropy, and this anisotropy would hamper the accuracy of the k-ε and k-ω models.

2.5 Conclusions

Through a comparison with experimental data an accurate model for the flow field below an isothermal annular jet has been developed. This model agrees well with the experimental correlations, it provides insight into annular jet physics, and it is a useful tool for engineering annular jet orifices. At different flow rates a change in flow behavior was observed as the jet velocity progressed through the incompressible to compressible, but sub-sonic, flow regimes. One observed effect of increasing

compressibility seems to be that of extending the area of flow reversal farther from the die face, as well as shifting the velocity peak away from the die.

Rather than using all the Fluent default parameters, we used a value of 1.24 for $C_{1\varepsilon}$; this value was suggested by Krutka et al. (2002). In addition, we set the turbulence parameter $C_{2\varepsilon} = 1.82$ to allow a much better agreement of the simulation with experimental measurements. Specifically, changing the value of $C_{2\varepsilon}$ allowed excellent fits to experimental data of both the centerline velocities and the half-width spreading rate.

In comparing different air flow rates, it was found that at higher, but industrially operable, air flow rates the effects of compressibility become significant. At large distances from the die, however, it was found that these effects are much smaller than in the near field. When melt blowing dies are operated at high nominal velocities (velocities greater than approximately 100 m/s), compressibility should be taken into account for the calculation of the air flow field for positions close to the die.

An annular jet has significantly different flow characteristics than the more well studied circular jets. The presence of the inner annular wall induces large differences in turbulent behavior. The presence of the recirculation region is the most apparent example of the center wall effects. Another effect of the annular orifice is the large generation of turbulence in the immediate vicinity of the orifice. This turbulence generation is substantially greater for an annular orifice than a circular orifice. In addition, the computational results suggest that the turbulence within an annular jet is anisotropic with larger Reynolds stresses along the axial direction than

any cross direction. This may potentially explain why the common k-ε model does not do a particularly good job of modeling turbulent melt blowing jets.

2.6 Nomenclature

C_{1ps} = Coefficient for the slow pressure-strain term of the Reynolds stress model

C_{2ps} = Coefficient for the rapid pressure-strain term of the Reynolds stress model

C'_{1ps}, C'_{2ps} = Coefficients for the modeling of the wall reflection effects on the pressure-strain term of the Reynolds stress model

$C_{1\varepsilon}$ = Parameter for the dissipation equation of the RSM model (equation 2)

$C_{2\varepsilon}$ = Parameter for the dissipation equation of the RSM model (equation 2)

C_{μ} = Coefficient for the modeling of turbulent viscosity

D_i = outer diameter of annular orifice, mm

D_o= inner diameter of annular orifice, mm

D_h= difference between inner and outer diameters, D_o - D_i, mm

F (Z/Z_{max}) = function describing V_{ay} / V_{max}

FOA = Fraction Open Area, FOA=$(D_o^2-D_i^2)/D_o^2$

G (FOA) = function describing Z_{max} / D_o

H (FOA, Ma_o) = function describing V_{max} / V_{sound}

k = TKE = turbulent kinetic energy, $(1/2u_iu_i)$, m^2/s^2

Ma_o = nominal Mach number: $Ma_o = V_o/V_{sound}$

P = static pressure, Pa

q = turbulence intensity, $q = (u_i^2)^{0.5} / V_o$

SMK = maximum TKE at the location of the second peak (see Fig. 2.14)

SMP = second maximum peak position (see Fig. 2.14)

TKE = k = turbulent kinetic energy, m^2/s^2

V_{max} = maximum centerline axial velocity, m/s

V_o = nominal discharge velocity, m/s

V_{ay} = velocity in the y-direction, axial velocity, m/s

V_x = velocity in x-direction, m/s

x, y = spatial coordinates, mm

$x_{1/2}$ = jet half-width defined as the distance from flow centerline at which the mean x velocity becomes half of its value at centerline, mm

Greek Characters

ε = dissipation rate of turbulent kinetic energy, m^2/s^3

μ= viscosity, kg/(m*s)

ρ = local density, kg/m^3

σ_k = turbulent Prandtl number for the turbulent kinetic energy

σ_ε = turbulent Prandtl number for the rate of dissipation

2.7 References

Durbin, P.A.; Petterson Reif, B.A. "Statistical Theory and Modeling for Turbulent Flows", John Wiley and Sons Ltd., West Sussex, England, pp 147, 149, **2001**.

Ferdman, E.; Ötugen, M.V.; Kim, S. "Effect of Initial Velocity Profile on the Development of Round Jets", *J. Prop. Power*, **2000**, *16*, 676-686.

Fluent 6.0 User's Guide; www.fluent.com, Fluent Inc., Lebanon NH, **2003**.

Harding, J.W.; Keller, J.P.; Buntin R.R. "Melt-blowing Die for Producing Nonwoven Mats", U.S. Patent 3,825,380, **1974**.

Kotsovinos, N.E. "A Note on the Spreading Rate and Virtual Origin of a Plane Turbulent Jet", *J. Fluid Mech.* **1976**, *77*, 305-311.

Krutka, H.; Shambaugh, R.L.; Papavassiliou, D.V. "Analysis of a Melt Blowing Die: Comparison of CFD and Experiments", *Ind. Eng. Chem. Res.* **2002**, *41*, 5125-5138.

Krutka, H. M.; Shambaugh, R. L.; Papavassiliou, D. V., "Effects of Die Geometry on the Flow Field of the Melt Blowing Process", *Ind. Eng. Chem. Res*. **2003**, *42*(22), 5541-5553.

Lai, J.C.S.; Nasr, A. "Two parallel plane jets: comparison of the performance of three turbulent models", *Proc. Instn. Mech. Engrs*., **1998**, *212*, 379-391.

Lau, J.C. "Effects of exit Mach number and temperature on mean-flow and turbulence characteristics in round jets". *J. Fluid Mech*. **1981**, *105*, 193-218.

Launder, B.E.; Reece G.J.; Rodi, W. "Progress in the Development of a Reynolds-Stress Turbulence Closure", *J. Fluid Mech.*, **1975**, *68*, 537-566.

Majumdar, B.; Shambaugh, R.L. "Velocity and Temperature Fields of Annular Jets", *Ind. Eng. Chem. Res.* **1991**, *30*, 1300-1306.

Marla, Vishnu T.; Shambaugh, R.L. "Three-Dimensional Model of the Melt-Blowing Process", *Ind. Eng. Chem. Res*. **2003**, *32*, 6993-7005.

Mukhopadhyay, A.; Prasad, R.O.S.; Grald, J. Sun; Lifshutz, N.; "Performance Analysis of Melt-blown Dies Using Computational Fluid Dynamics", Proceedings of INTC 2002 Conference, Atlanta, GA, USA, September 25-26, **2002**.

Obot, N.T.; Graska, M.L.; Trabold, T.A. "The Near Field Behavior of Round Jets at Moderate Reynolds Numbers", *Can. J. Chem. Eng.* **1984**, *62*, 587-593.

Obot, N.T.; Trabold, T.A.; Graska, M.L.; Ganghi, F. "Velocity and Temperature Fields in Turbulent Jets Issuing from Sharp-Edged Inlet Round Nozzles", *Ind. Eng. Chem. Fund.* **1986**, *25*, 425-433.

Pope, S.B. *Turbulent Flows*, Cambridge University Press, **2000** p. 382.

Rao, R.S.; Shambaugh, R.L. "Vibration and Stability in the Melt Blowing Process", *Ind. Eng. Chem. Res*. **1993**, *32*, 3100-3111.

Schlichting, H. Boundary Layer Theory, 7th Ed., McGraw Hill, **1979**, pp. 729-734, 737-738.

Schwarz, E.C.A. "Apparatus and Process for Melt-Blowing a Fiberforming Thermoplastic Polymer and Product Produced Thereby", U.S. Patent 4,380,570, **1983**.

Tanaka, E. "The interference of two-dimensional parallel jets (1st report, experiment on the combined flow of dual jet)", *Bull. JSME*, **1970**, *13*, 272-280.

Tanaka, E. "The interference of two-dimensional parallel jets (2nd report, experiments on the combined flow of dual jet)", *Bull. JSME*, **1974**, *17*, 920-927.

Uyttendaele, M.A.J.; Shambaugh, R.L. "The Flow Field of Annular Jets at Moderate Reynolds Numbers", *Ind. Eng. Chem. Res.* **1989**, *28*, 1735-1740.

Die Name	D_o	D_i	Fraction Open Area	Grid Size
	mm	mm	unitless	cells
A	2.37	1.30	0.699	58,850
B1	2.46	0.00	1.000	61,150
B3	2.46	1.27	0.733	59,950
B5	1.89	1.27	0.548	59,350
C	1.25	0.45	0.870	58,300
D	2.75	2.25	0.331	58,100
E	3.50	0.50	0.980	60,300

Table 2.1: Die Dimensions and Grid Sizes Used

	Flow Rate			
Die	**0.125 g/s**	**0.25 g/s**	**0.50 g/s**	**1.0 g/s**
A		**X**	**X**	**X**
B1		**X**	**X**	**X**
B3		**X**	**X**	**X**
B5	**X**	**X**	**X**	
C	**X**	**X**		
D	**X**	**X**	**X**	
E		**X**	**X**	**X**

X	Flow Condition Simulated
	Flow Condition Not Simulated

Table 2.2. Die and flow rate combinations used

Constant	Value
Equation 7	
c1	1.2267
c2	-0.05913
Equation 8	
a	-18.67
b	373.01
c	-2661.51
d	10558.70
e	-26244.90
f	42648.80
g	-45422.30
h	30612.00
I	-11855.60
j	2011.50
Equation 9	
α	0.31596
β	-0.73194
γ	0.60345
Equation 10	
A	2.51858
B	6.55777
C	1.74253

Table 2.3. Model equation constants that were produced by regression analysis

	Flow Rate											
Die	0.125 g/s		0.25 g/s		0.50 g/s		1.0 g/s		Average		Standard Deviation	
	Slope	Intercept	Slope	Intercept	Slope	Intercept	Slope	Intercept	Slope	Intercept	Slope	Intercept
A			0.1157	-0.4168	0.1132	-0.4418	0.1052	-0.4629	0.1114	-0.4405	0.0055	0.0231
B1			0.1168	-0.4398	0.1154	-0.4523	0.1108	-0.4456	0.1143	-0.4459	0.0031	0.0063
B3			0.1160	-0.4131	0.1146	-0.4431	0.1080	-0.4375	0.1129	-0.4312	0.0043	0.0160
B5			0.1172	-0.4168	0.1123	-0.4644			0.1148	-0.4406	0.0035	0.0337
C	0.1179	-0.4823	0.1158	-0.5347					0.1169	-0.5085	0.0015	0.0371
D	0.1181	-0.3311	0.1182	-0.3497	0.1147	-0.3653			0.1170	-0.3487	0.0020	0.0171
E			0.1121	-0.3819	0.1113	-0.3861	0.1101	-0.3959	0.1112	-0.3880	0.0010	0.0072
Average	0.1180	-0.4067	0.1160	-0.4218	0.1136	-0.4255	0.1085	-0.4355	**0.1139**	**-0.4243**	**0.0036**	**0.0489**

Table 2.4. Constants for half-width correlations for the cases that were studied

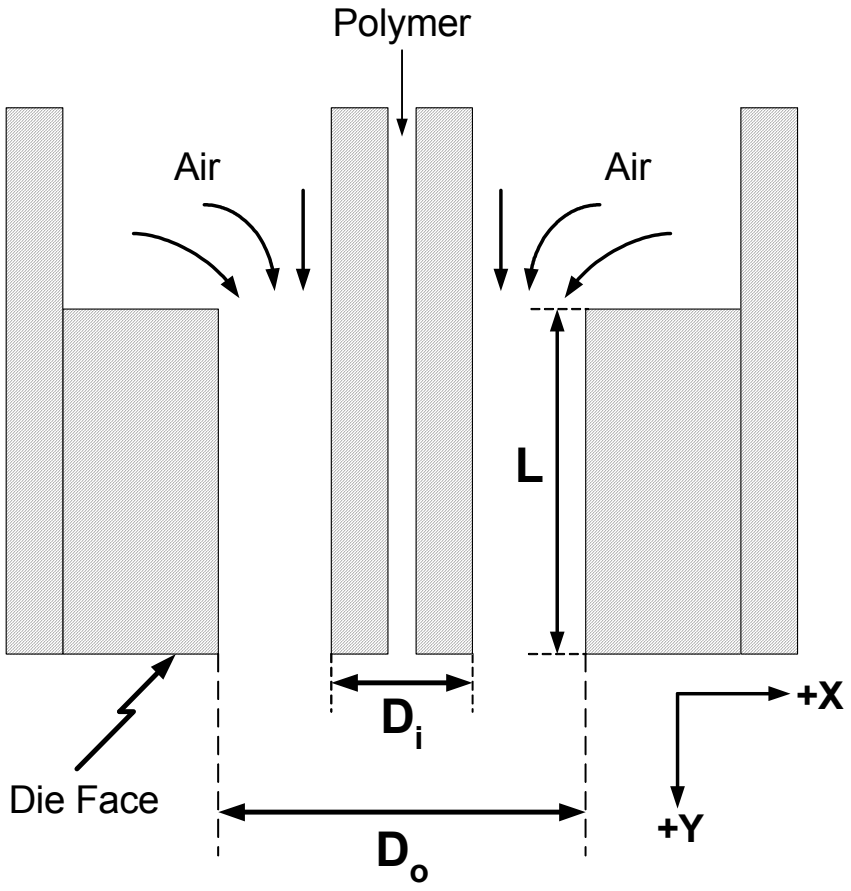

Figure 2.1. A cross-sectional view of the annular melt blowing die. The origin of the coordinate system is in the plane of the die face and at the center of the polymer outlet.

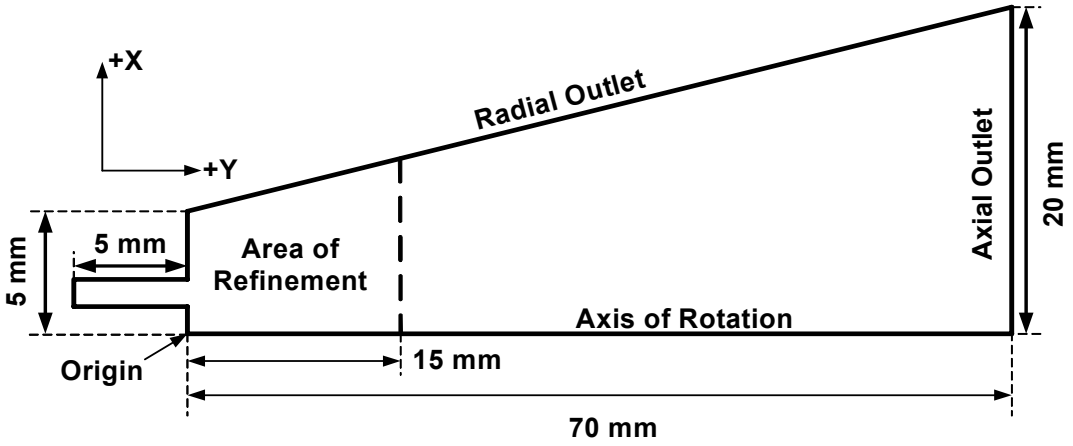

Figure 2.2. The computational domain used for the simulations. Note that this figure is rotated 90° relative to Figure 2.1. Thus, the left side of this figure corresponds to the top of the flow field, while the right side of the figure corresponds to the bottom of the flow field.

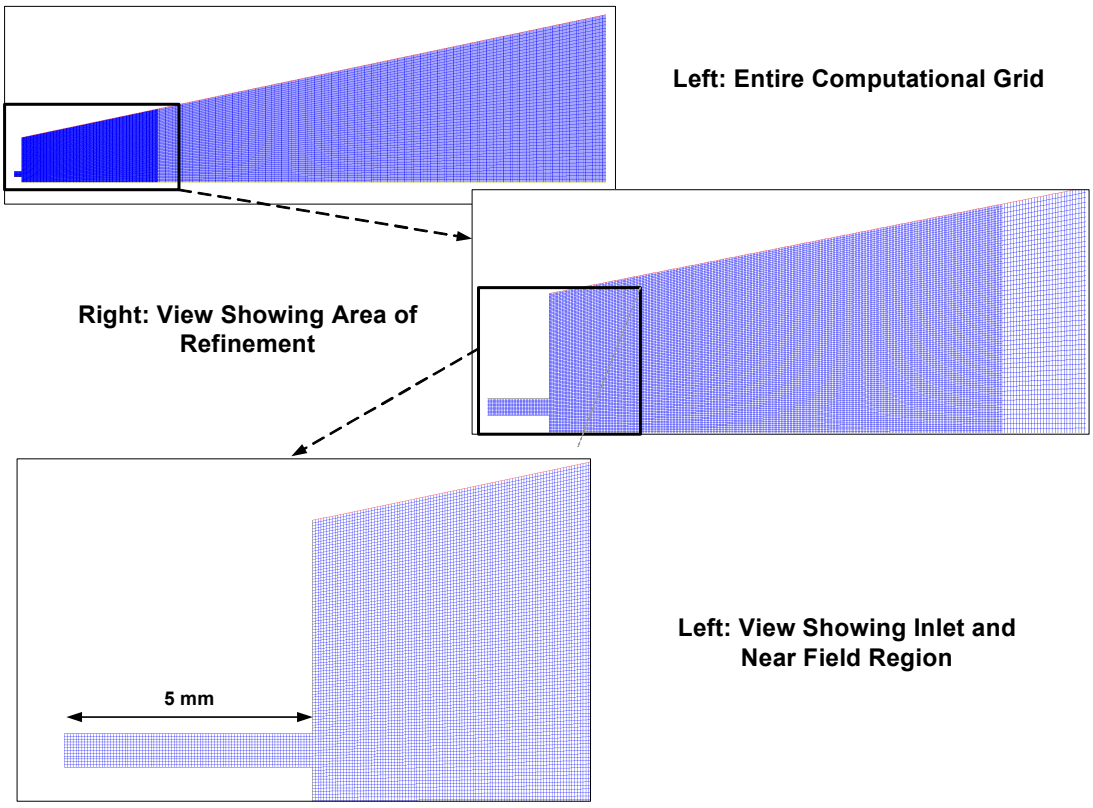

Figure 2.3. The actual grid used for simulations with Die B3. The width of the jet inlet shown is 0.595 mm (this inlet is the 5 mm long inlet shown in the bottom left of the figure).

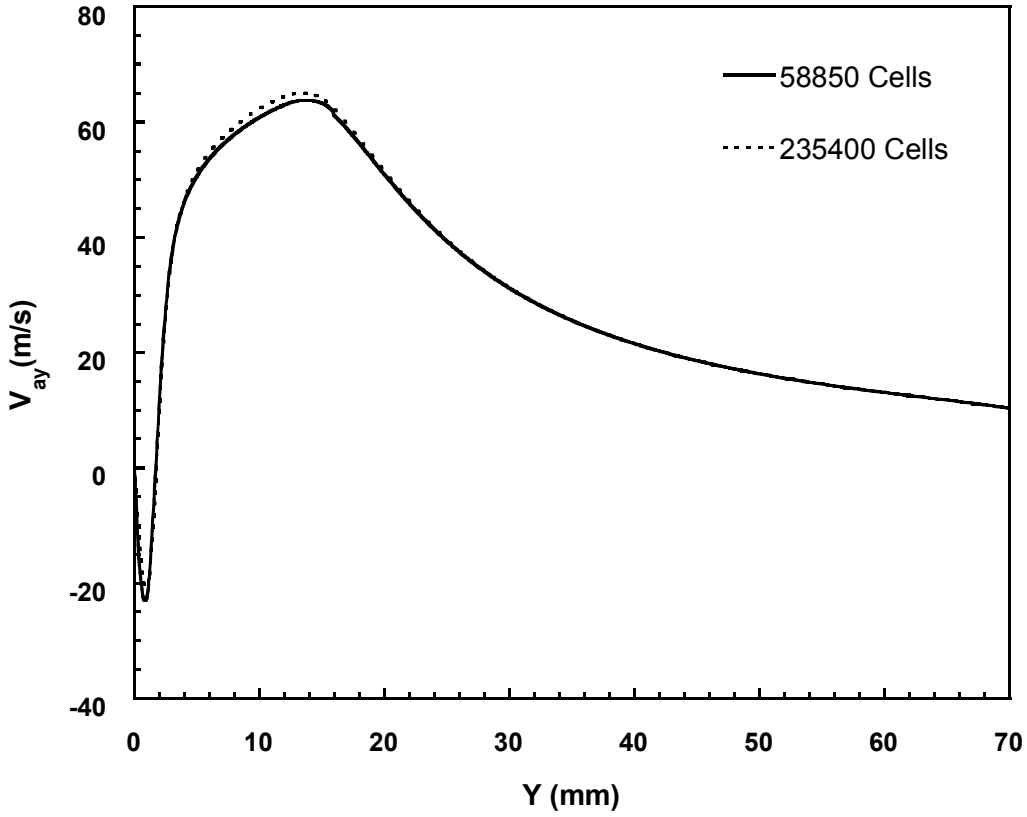

Figure 2.4. The effect of the grid cell number on the simulated profile of the centerline axial velocity (V_{ay}) for Die A run with an air throughput of 0.25 g/s.

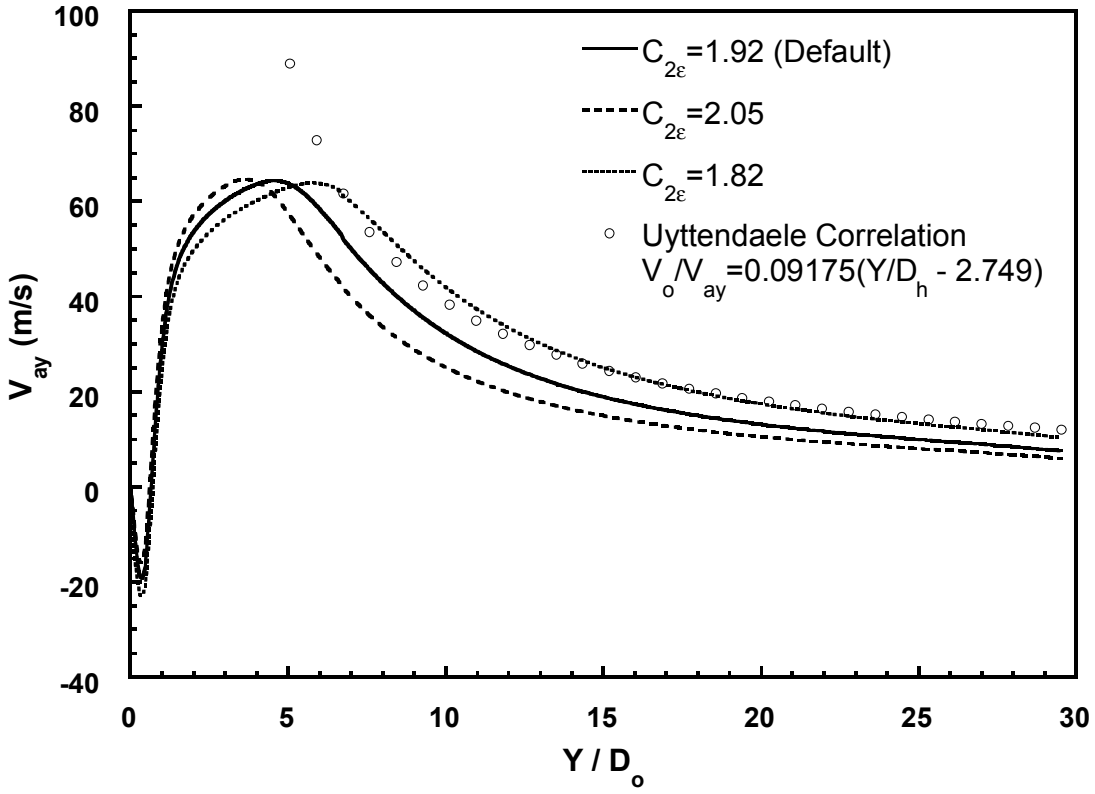

Figure 2.5. The effect of turbulence parameters on centerline velocity for Die A at an air throughput of 0.25 g/s. In the Uyttendaele correlation, $D_h = D_o - D_i$.

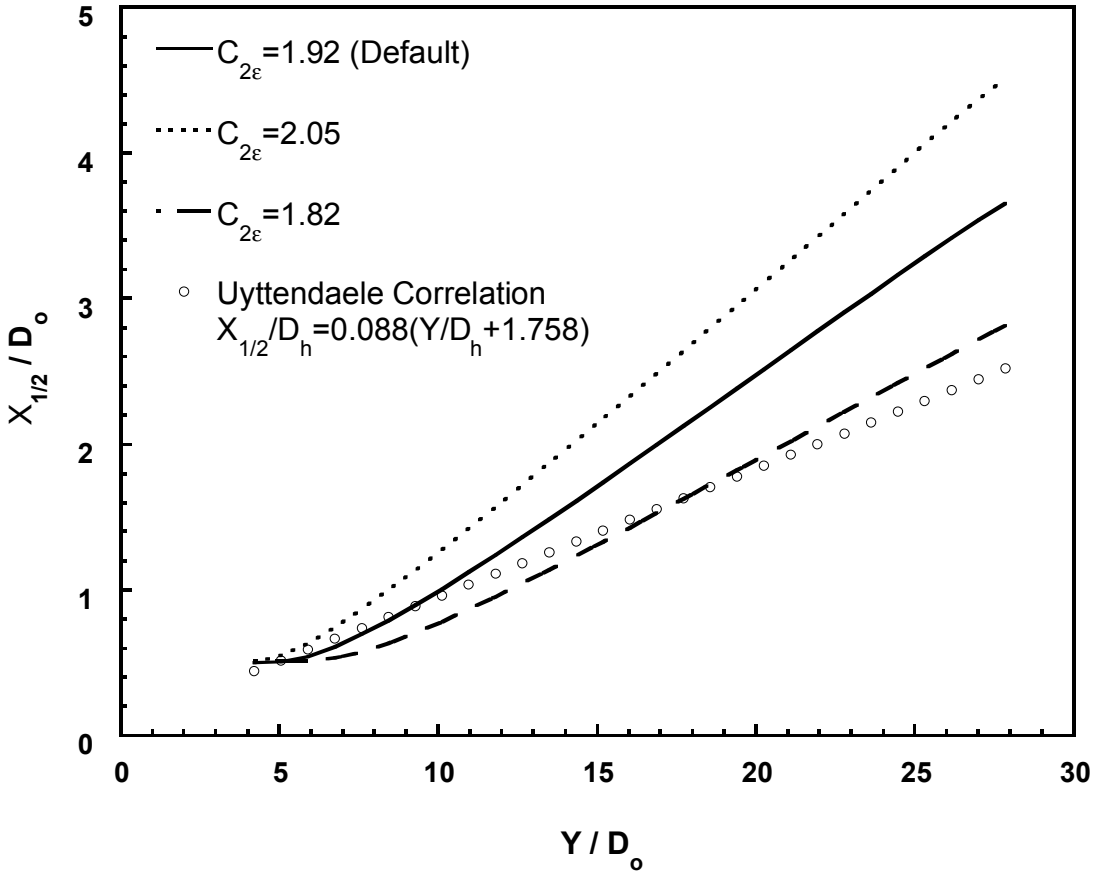

Figure 2.6. The effect of turbulence parameters on velocity half-width for Die A at an air throughput 0.25 g/s.

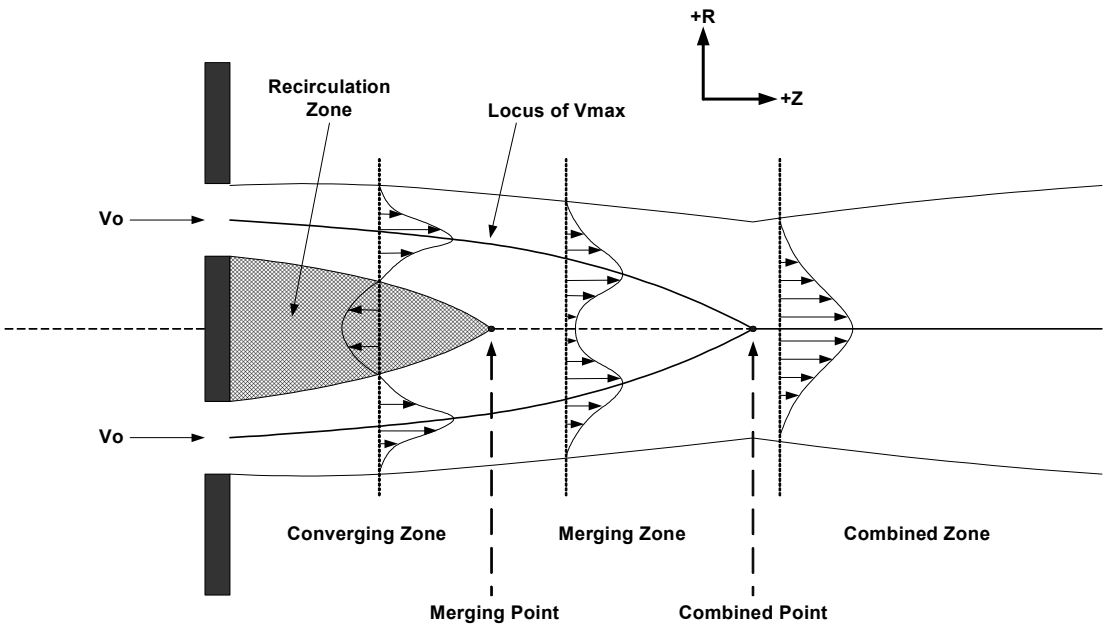

Figure 2.7. Diagram of near field flow of an annular jet. This diagram is based on that in Lai and Nasr (1998).

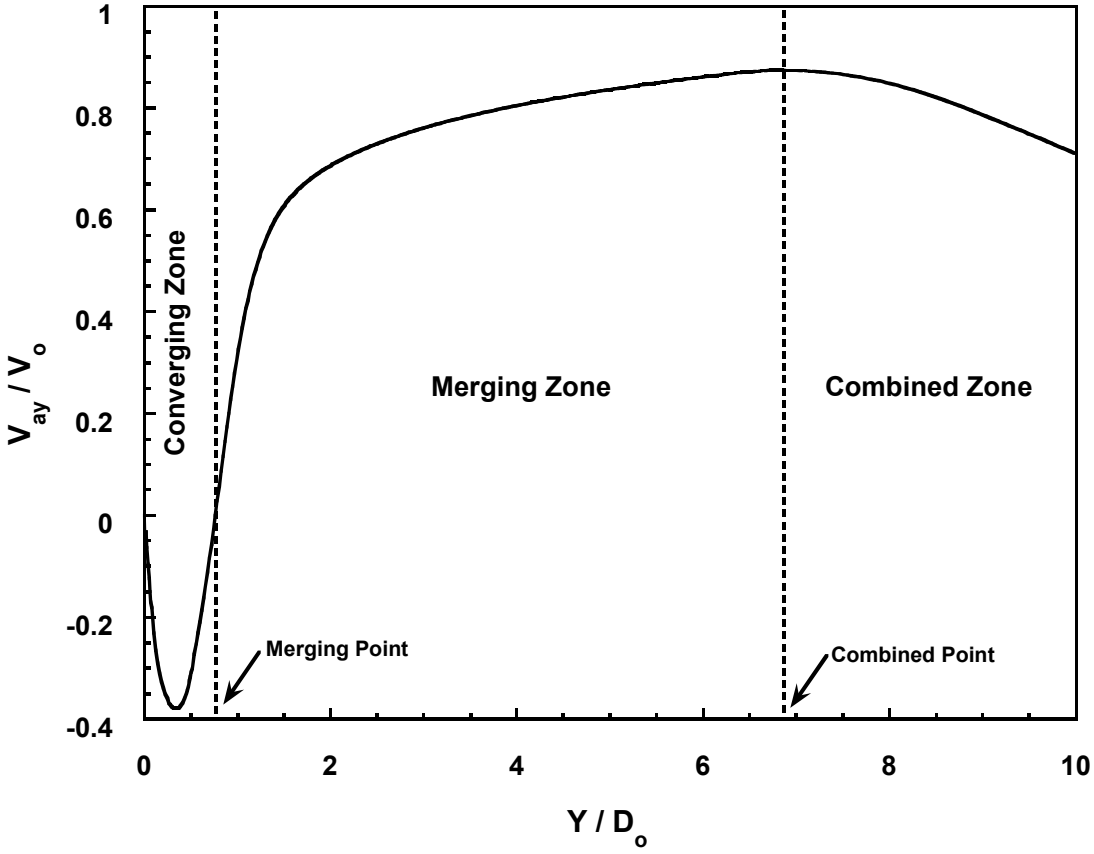

Figure 2.8. Near field centerline velocity for Die A at an airflow of 1.0 g/s. The regions of jet development are shown.

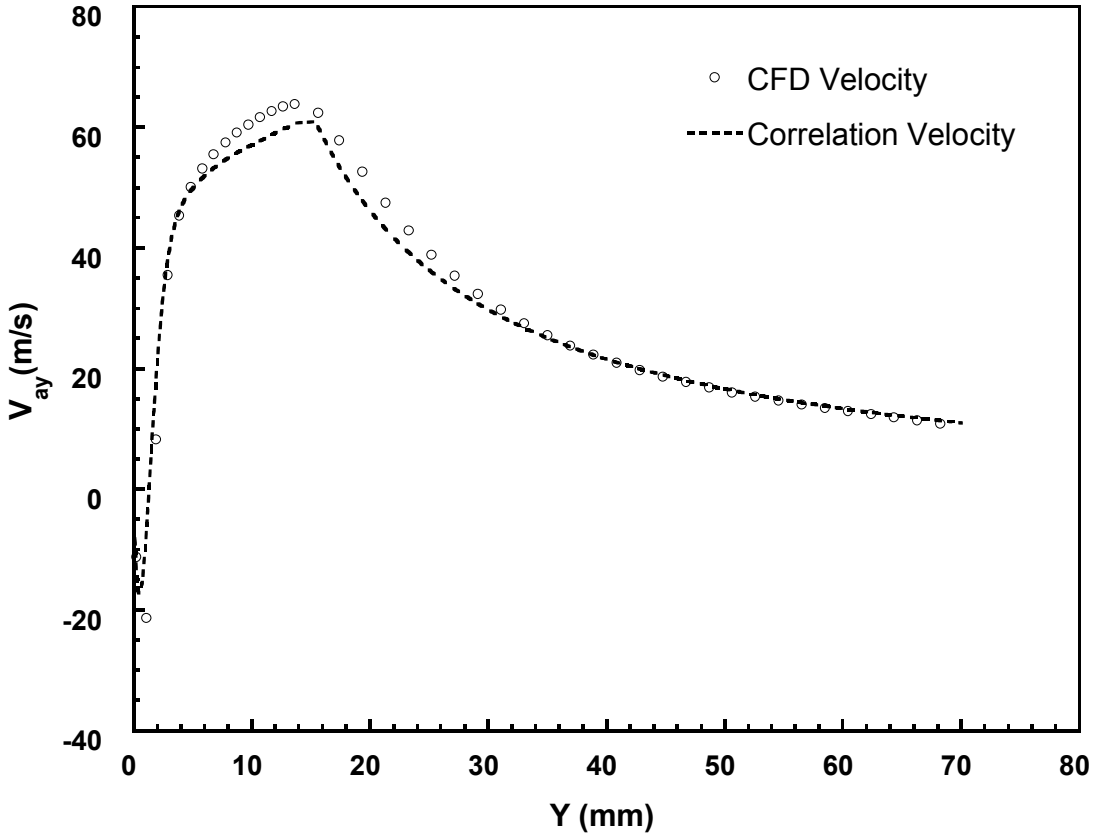

Figure 2.9. Comparison of centerline axial velocity as predicted by CFD with centerline velocity predicted by empirical correlations (see equations 7 to10). These CFD results and correlations are for Die B3 and an airflow of 0.25 g/s.

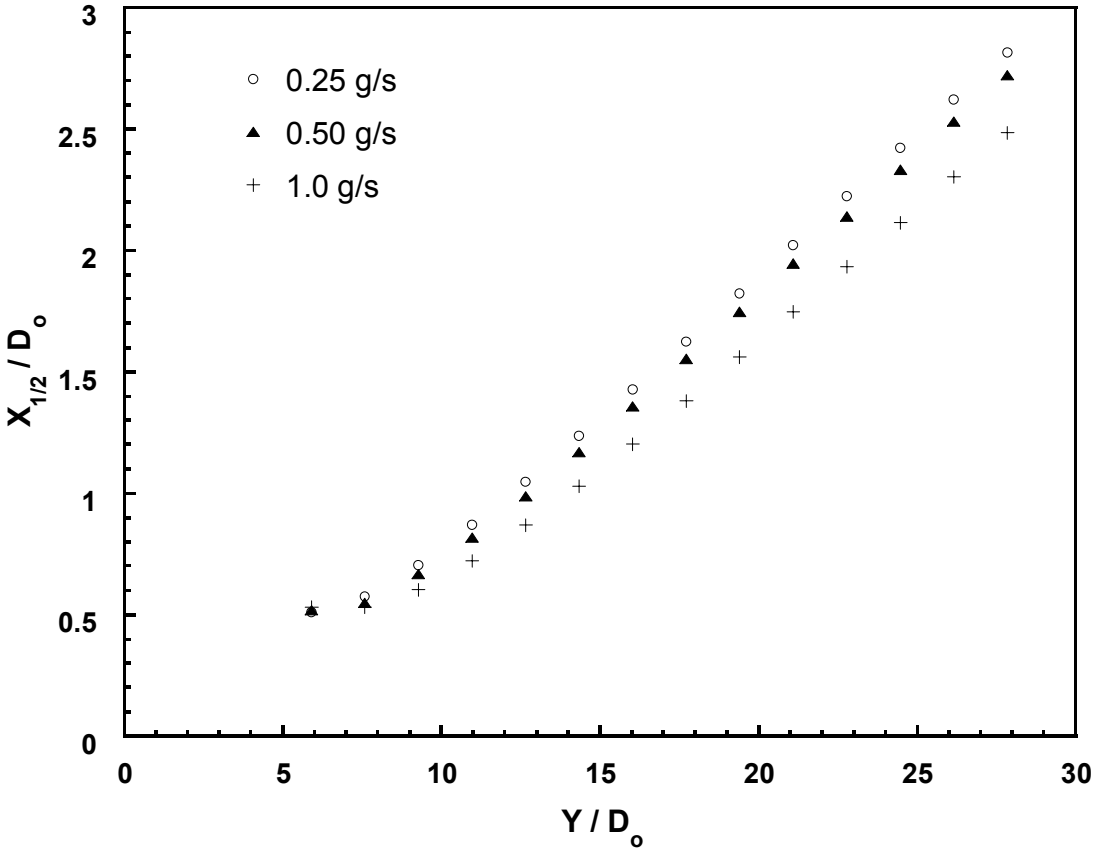

Figure 2.10. Effect of flow rate on jet spreading for Die A at 0.25, 0.5, and 1.0 g/s.

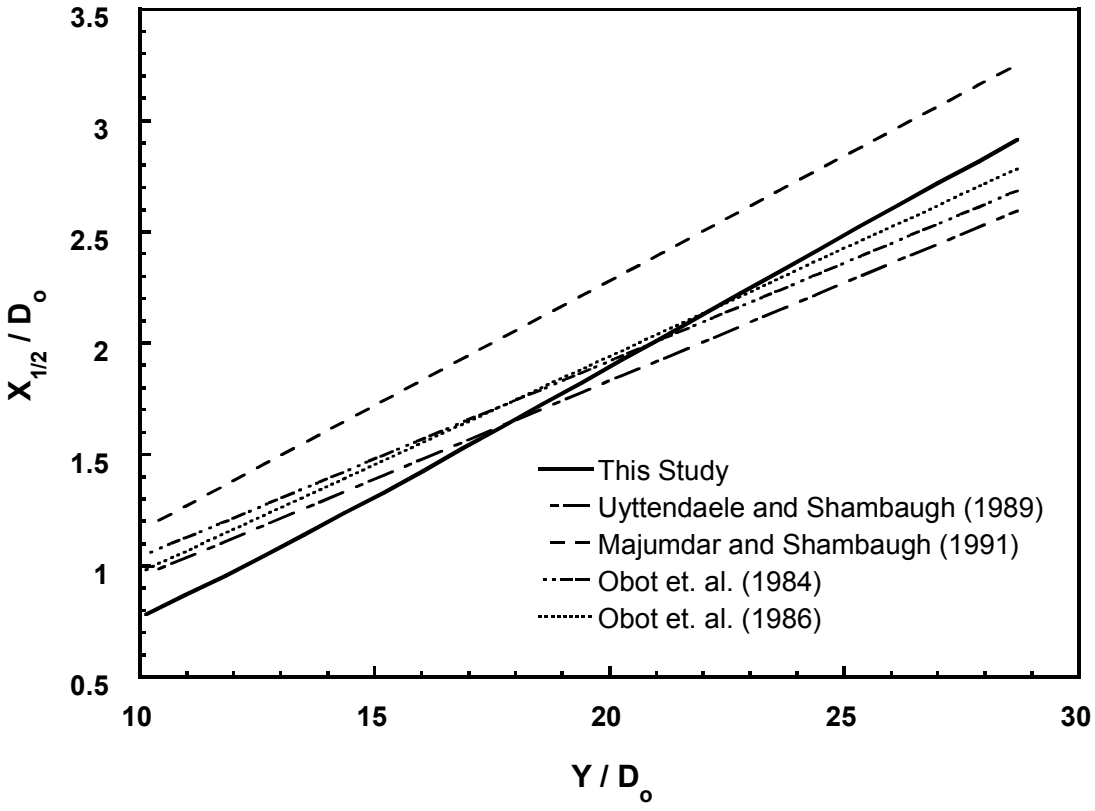

Figure 2.11. The average half-width (spreading rate) as predicted by CFD. Also shown are experimental jet spreading correlations developed by other researchers.

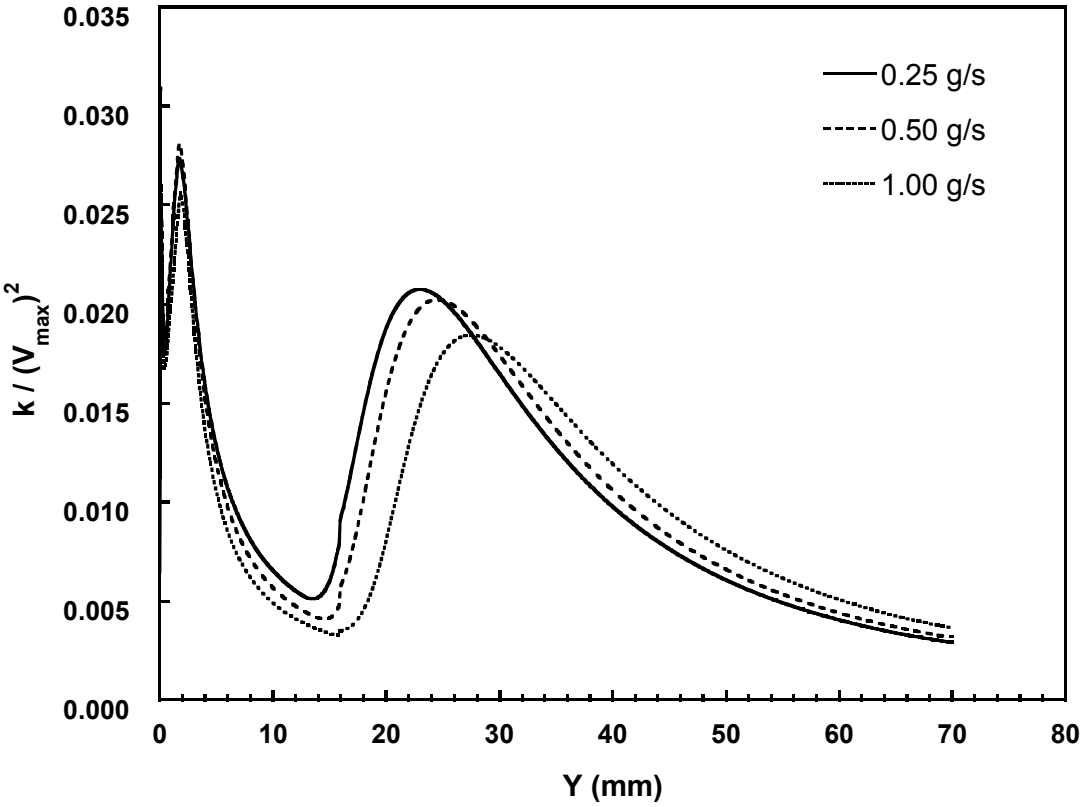

Figure 2.12. Centerline (dimensionless) TKE versus position for various air flowrates. This simulation is for Die A.

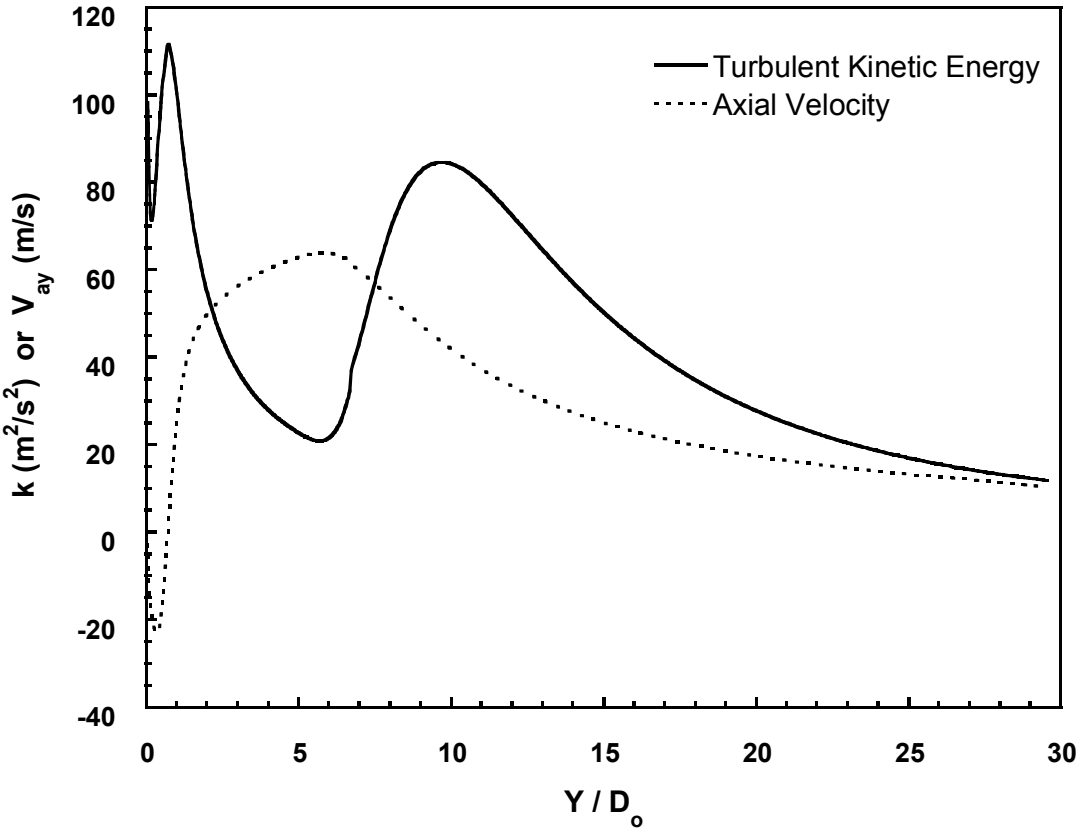

Figure 2.13. Comparison of centerline TKE and mean velocity for Die A at 0.25 g/s.

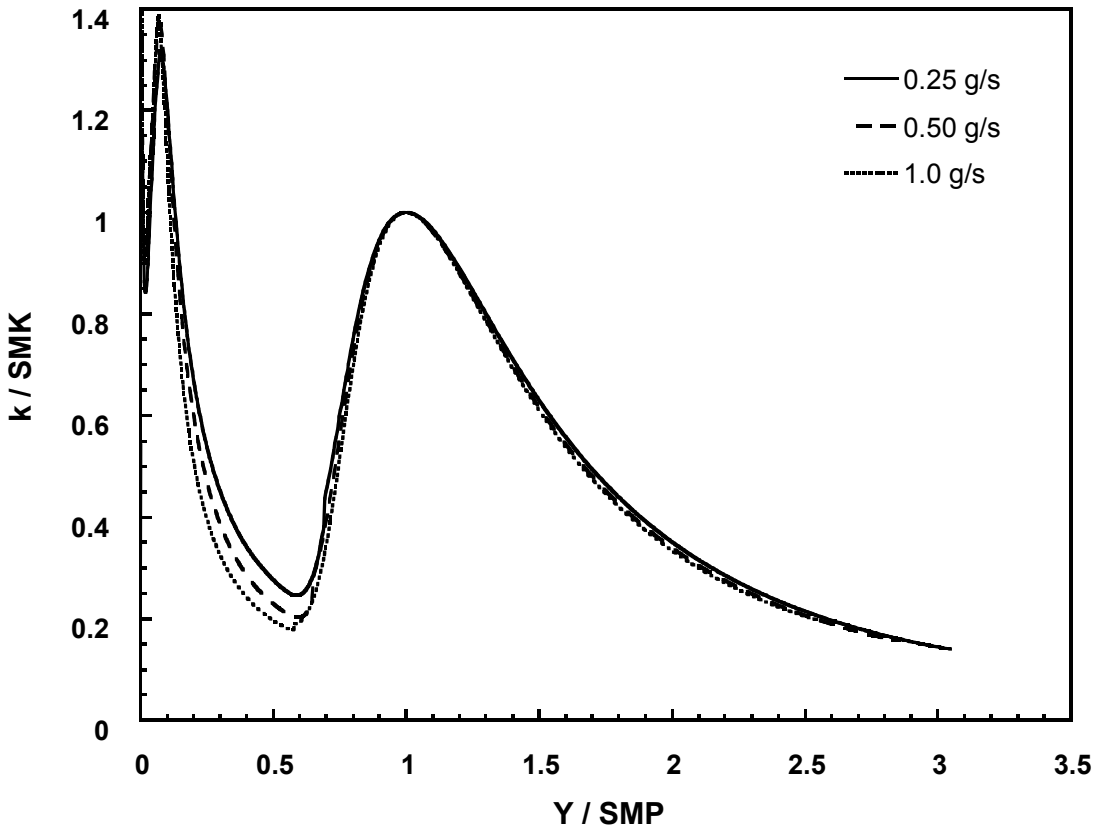

Figure 2.14. Generalized TKE plot for Die A. SMK = maximum TKE at the location of the second peak. SMP = second maximum peak position.

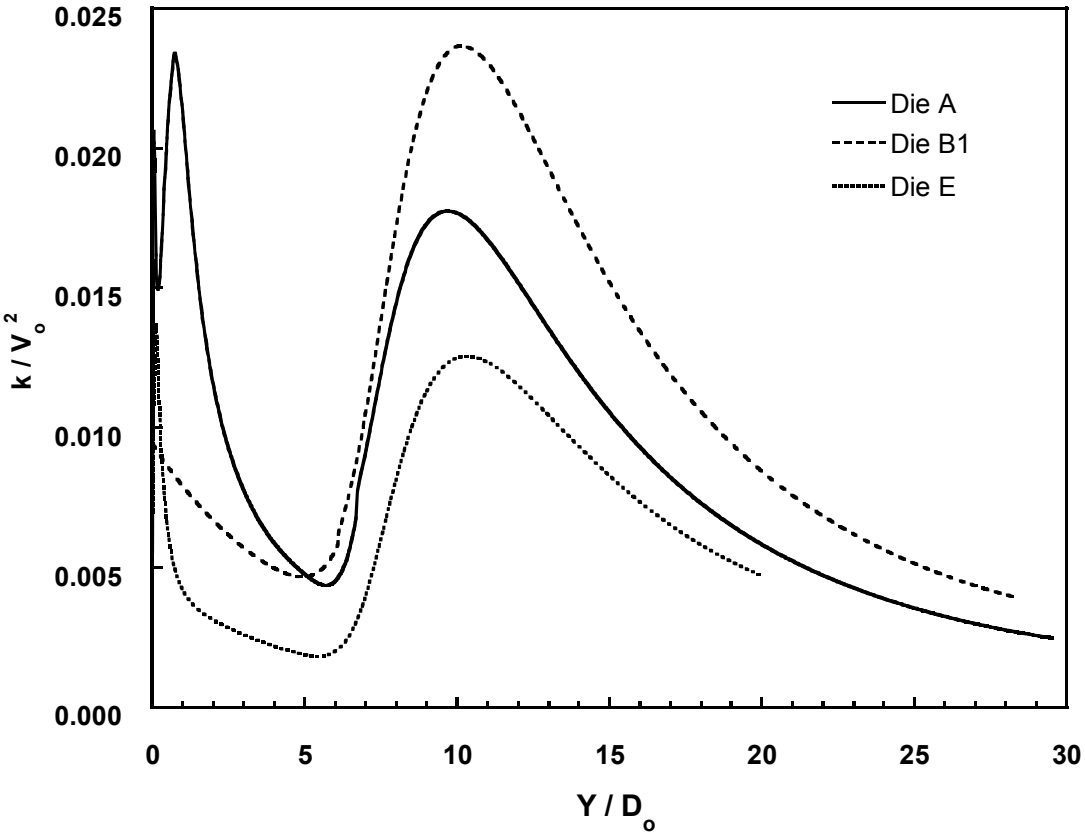

Figure 2.15. Comparison of (dimensionless) centerline TKE for Dies A, B1, and E at 0.25 g/s.

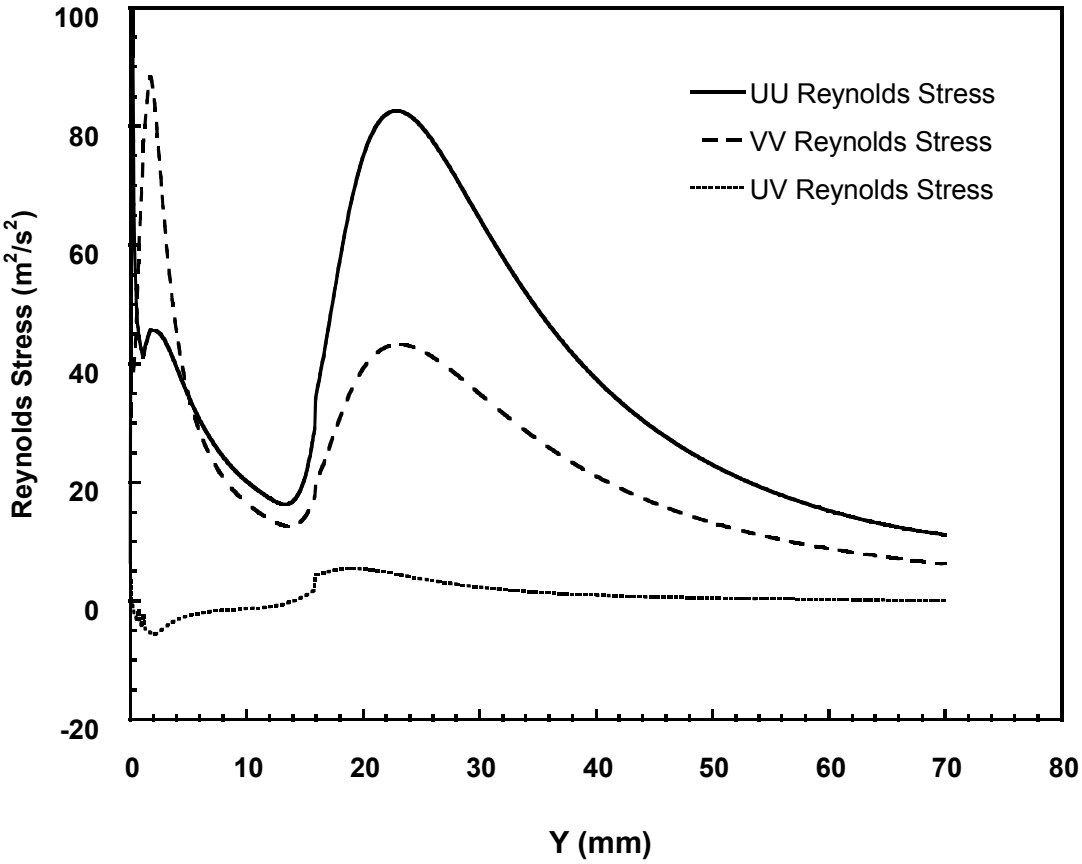

Figure 2.16. Centerline Reynolds stresses for Die A at 0.25 g/s.

Chapter 3

Analysis of a Converging, Annular, Isothermal Melt Blowing Jet Using Computational Fluid Dynamics

3.1 Abstract

An unconventional melt blowing die was analyzed using computational fluid dynamics (CFD). This die has an annular configuration wherein the jet inlet is tapered (the cross-sectional area decreases) as the air approaches the die face. It was found that the flow characteristics of this die are different from conventional slot and annular dies. In particular, for the tapered die the near-field normalized turbulent kinetic energy was found to be lower at shallow die angles. Also, it was found that the peak mean velocity behavior was intermediate between that of conventional

annular and slot dies. The centerline turbulence profiles were found to be qualitatively similar to those of annular dies; quantitatively, higher values were present for tapered dies.

3.2 Introduction

Melt blowing is an industrial method for the rapid production of nonwoven fibers. In melt blowing a polymer is melted and extruded through a capillary while heated air is blown through one or more jet orifices. These jet orifices are situated around the polymer capillaries such that the air jets impact upon the polymer as it extrudes from the capillaries. The aerodynamic drag of the air jets on the polymer provides the attenuation force that draws the polymer streams into fine diameter fibers. These fibers are usually collected on a moving screen for either direct use or further processing. Many different designs exist for melt blowing dies; the most common arrangements are slot and annular dies (Shambaugh, 1988). Zhao (2002) recently reviewed the designs and development of industrial melt blowing dies. Commercial annular dies have multiple holes, but the study of single-hole dies give results that can easily be extended to multiple-hole configurations. In the single-hole die shown in Figure 3.1, an annular air outlet surrounds a polymer orifice. Observe that the air flows parallel with the polymer, and this is typical of the common commercial design attributed to Schwarz (1983). An alternative to the common parallel-flow design is the tapered die shown in Figure 3.2. Observe that, in the tapered die, the air jet impacts the polymer stream at an angle θ where $90° > \theta > 0°$. In a conventional slot die the air exits from two slots, and the air impacts the polymer

streams at an angle θ that is also in the range $90° > \theta > 0°$. The result of this tapered design is a hybrid of the common annular and slot die designs. However, within the confines of the die cavities, the cross-sectional area available for air flow does not decrease for a slot die. But for the tapered, or conical, airflow path shown in Figure 3.2, the cross-sectional area available for airflow decreases significantly as the air flows towards the die face.

An unconventional die with this annular taper is described in the United States patent issued to Brackmann and Diiani (1975). However, to our knowledge there has been no performance data published for tapered dies of this type. According to Brackmann and Diiani, a tapered annular die design can avoid two common concerns that occur with conventional slot die designs. The first, fiber entanglement, can be controlled through the use of a single air jet for each polymer capillary (the Schwarz die also has this advantage). The second concern is the inflexible nature of the slot die, can be overcome with the modularity of the die design described in the patent. This modularity allows for individual dies to be replaced without replacing an entire assembly (which is different from the conventional Schwarz die). Also, such a modular design would allow different die geometries (e.g., with different polymer orifice diameters or die angles) to be incorporated into a single melt blowing assembly. This would result in a single fiber mat containing fibers with different properties (strength, diameter, etc.). Other modular melt blowing designs have been developed. For example, Allen and Fetcko (1997) developed a modular die system for adhesive deposition purposes.

The aerodynamic characteristics of melt blowing dies are crucial in determining the final mat properties and production rates of melt blowing processes. Also, besides being of great practical importance for fiber producers, the study of die aerodynamics is of great theoretical interest due to the unique requirements of an efficient melt-blowing die. The flow around a melt-blowing die is a specific form of free turbulent jet flow, which has been widely studied and documented (Schlichting, 1979). However, unlike typical turbulent jet flows, the tapered jet considered herein has a converging, annular air orifice. For our work, a single converging die was considered, and calculations were made for isothermal conditions. Previous work has shown that many of the characteristics of an isothermal die can be carried over to nonisothermal behavior (Harpham and Shambaugh, 1996; 1997). Another assumption was that there was no polymer stream present. Because the mass flow of air is much greater than the mass flow of polymer, this appears to be a good approximation. In support of this approximation, previous modeling work has been based on air measurements taken in the absence of polymer flow (e.g., see Uyttendaele and Shambaugh, 1990).

In our work the air flow was simulated with a commercial CFD package, Fluent®, using a Reynolds Averaged Navier-Stokes turbulence model. The Reynolds Averaged Navier-Stokes (RANS) method is based on the decomposition of velocity into mean and fluctuating parts. This method has the advantages of being relatively simple computationally and widely applicable. In order to close the system of the RANS equations, an empirical model is necessary. Several models have been developed and applied to the closure problem. Much theoretical and experimental

work has been done showing the advantages and disadvantages of each model for various flow problems (Pope, 2000; Wilcox, 1993). For our work the Reynolds Stress Model (RSM) was used (see Launder et al., 1975). This RSM model was chosen because Krutka et al. (2002; hereafter, this work is referred to as KSP) showed that, for slot dies, the RSM model provided better agreement with experimental data than the popular k-ε model and its variants. Moore et al. (2004) showed similar results for conventional annular melt blowing dies (hereafter this work will be referred to as MSP). For our work the technique developed in KSP was applied to the tapered die geometry.

In our work the aerodynamics in the vicinity of a converging melt blowing die were studied and compared to results for conventional slot and annular dies. The two variables that were explored were the die angle and the inlet velocity. As defined earlier in Figure 3.2, the die angle θ is the angle the inlet taper makes with the die plane. We tested θ values of 40°, 45°, 50°, 60°, and 70°. The mean inlet velocity V_o (see Figure 3.3) was set at 17.3 m/s and 34.6 m/s.

3.3 Numerical Procedure

The die was modeled as a two-dimensional axisymmetric case centered at the end of the polymer capillary; see Figure 3.3. The die had a flat (blunt) surface where the polymer orifices would be placed. (See KSP for a discussion of blunt versus sharp slot die designs.) For the modeling, an inlet region was used to achieve more fully developed flow before the air jet enters the quiescent air. The parameters f, b and q were kept constant as the die angle was varied. The slot offset q is listed on

Figure 3.3 for the different angles studied. The geometry in Figure 3.3 is the axisymmetric analogue to that used by KSP. In the work described herein, the effect of die angle on flow properties was explored over a wider range than the slot angle considered in KSP.

The computational domain was cylindrical with a 100 mm length and a 30 mm radius (see Figure 3.3). Based on previous papers on melt blowing (KSP; MSP) this computational domain size was sufficient to adequately resolve the flow features of the tapered jets. The computational domain was divided into rectangular cells using a sub-mapping grid generation algorithm. Initially, the edges of the domain were given 0.122 mm node point spacings. This relatively coarse grid was then partially refined by cutting the node spacing in half (to 0.061 mm). This refinement was only applied to the cells within the volume where z was less than 30 mm and r was less than 7.5 mm. After refinement, the final grids contained approximately 245,000 cells each. The actual number of cells in each grid varied a small amount due to the varying inlet geometry. KSP and MSP both showed that this level of resolution was sufficient to achieve grid independence.

The inlet boundary condition was set as a uniform velocity inlet with a turbulence intensity of 10 % and a hydraulic diameter of 0.7 mm. Outlets were specified as pressure outlets at an atmospheric pressure of 101325 Pa. Since a pressure specification on an outlet allows for flow into the system through the outlets, turbulence specifications for backflow were set as 10 % intensity and 10 mm hydraulic diameter. All the other boundaries were set as no-slip walls. All boundary temperatures were set to be constant at 300K.

Comparisons were made between our tapered die simulations and the work of others on slot dies and annular dies. The length chosen for normalization of our data was the outer diameter, D_o, of the die orifice at the die face. Based on the parameters defined in Figure 3.3, $D_o = 2 (f + b)$. This D_o is comparable to both the outer diameter for an annular die (see Figure 3.1) and the width of the jets and nosepiece (dimension h in KSP) in a slot die. With this normalization the flow properties of the three different die geometries can be compared with a common frame of reference. The values of f and b used in our simulations were fixed at f = 1.01 mm and b = 0.65 mm. These values are of the same order as the nosepiece size and gap size used in the slot die simulations of KSP, as well as the experimental work of Harpham and Shambaugh (1996, 1997) and Tate and Shambaugh (1998).

3.3.1 Physical Model

The choice of physical models and parameters are critical to achieving realistic results from any CFD method. In preliminary simulations of our tapered die, it was found that, locally, very high velocities were predicted. This is due to the constriction caused by the die taper. These large local velocities required the use of a compressible flow model. The ideal gas model was chosen, as it is both explicit in density and simple computationally. The pressures - less than 20 kPa gauge - and the temperatures - very near 300K - encountered in our simulations suggested that the ideal gas model would be suitable. Other physical properties, such as viscosity and thermal conductivity, were assumed to be constant at the ambient conditions. The use of the ideal gas model requires the use of the non-isothermal solver. The temperature

of the air was allowed to change as the pressure changed. Only small temperature gradients were observed during the simulations; these gradients were deemed to have insignificant effects on the results.

As described previously, the modeling of turbulence is a much more complex matter. The choice of closure model can have large effects on the computational results. For our work, we did not use the suggested, or default, values for all of the RSM parameters that were proposed by Launder et al.(1975). The effects of varying turbulence parameters in melt blowing applications were studied in KSP and MSP. The non-default parameter values used by KSP, $C_{1\varepsilon} = 1.44$ and $C_{2\varepsilon} = 2.05$, were used for the present work. As also suggested in KSP, all other parameters were set at their default values. Since these parameters provide an accurate model for air flow patterns below slot jets with various die angles, it was surmised that these parameters also can be applied to tapered nozzles with various die angles.

3.3.2 Computational Procedure

Calculations were performed using Fluent® version 5.5 CFD software from Fluent, Inc. Grids were generated using Gambit software and directly exported into Fluent®. The grids were then loaded into the Fluent® software, where boundary, model, and physical property parameters were assigned as previously described. Solution initialization was accomplished using the built-in initialization routine, based on the inlet boundary condition.

Initially, each case was iterated using first-order upwind discretization and the standard k-ε model with constant air density. After this simpler model showed

reasonable convergence – i.e., residuals less than 10^{-4} – the settings were changed to second-order upwind, RSM turbulence, and ideal-gas air density. This preliminary iteration procedure served two functions. First, it reduced the total required iteration time; second, it prevented initial divergence of ideal gas compressibility model. Each case was allowed to iterate until the largest residual was no larger than $2x10^{-5}$. The iterations required for convergence varied from case to case, but 20,000 to 25,000 iterations were typical. Computationally, this work was intensive, but not prohibitively so. A full case generally required 140 MB of RAM and took less than 48 hours to converge on dual 2.2 GHz Intel Xeon® Processors.

3.3.3 Data Analysis and Results

The simulations presented in this work focus on the values of flow-related variables along the mean spinline, which is also the axis of rotation. Specifically, the simulations allow the examination of the mean axial velocity, the turbulent kinetic energy (TKE, or k), and the turbulent dissipation rate (ε). The mean velocity profiles are important to the melt blowing process because the air drag on the filament is the primary attenuating force. The mean axial velocity is the component of the mean velocity that is directed away from the die face and most responsible for fiber attenuation. The estimation of turbulent kinetic energy is important in understanding the intensity of the turbulent fluctuations in the flow. Turbulent kinetic energy is defined as the kinetic energy of the velocity fluctuations, as shown in Equation 1.

$$k \equiv \frac{1}{2}\sqrt{< u_i u_i >^2} \qquad (1)$$

The turbulent dissipation rate (ε) is important as it can provide the locations within the flow field where the turbulent velocity fluctuations are dissipated. The turbulent dissipation rate (ε) is defined as half the kinematic viscosity multiplied by the mean of the sum of the squares of the fluctuating rate of strain tensor, as shown in Equation 2.

$$\varepsilon \equiv \frac{1}{2}\nu < s_{ij}s_{ij} > \qquad (2)$$

The effect of die angle on the mean axial velocity profile is shown in Figures 3.4 and 3.5. Figure 3.4 shows the results for an inlet velocity of 17.3 m/s, and Figure 3.5 shows the results for an inlet velocity of 34.6 m/s. The general shapes of the velocity profiles are very similar and show several definitive features. Flow characteristics observed here are similar to the flow development regions in annular jets and slot jets. For example, our results resemble the work of Uyttendaele and Shambaugh (1989), as well as MSP, wherein the flow characteristics and the flow development regions of annular jets are described. Our results also resemble the work of Nasr and Lai for the flow development in parallel plane jets (Nasr and Lai, 1997; Lai and Nasr, 1998).

Figures 3.4 and 3.5 show that, at very short distances from the die face, there is a region of negative mean axial velocity due to flow separation near the blunt die tip. Observe that the size of the flow separation has a strong dependence on the die angle and inlet velocity. The next section of the profiles (beyond an abscissa value of about 1) show a quick rise in velocity, then a smaller increase to the velocity peak, which occurs approximately 8 mm from the die face for all die angles. This rapid,

then slower increase in velocity is different from what happens with slot dies, but is similar to the behavior of annular dies. At distances beyond the velocity peak, each profile shows a rapid decay that tapers off to a much lower decay, which is expected since, at large distances from the die, the flow will decay in the same manner as circular turbulent jets (Schlichting, 1979).

In order to generalize the behavior of the jet flow, it is convenient to nondimensionalize the flow parameters. For our work, the mean outlet velocity V_2 was used for non-dimensionalization of velocities. Because of the tapered geometry of the die, the velocity of the air in the die increases as the air approaches the nozzle discharge. The area available for flow at any position within the nozzle can be described as the total airflow divided by the annular cross-sectional area available for flow. In can be easily shown that the discharge velocity V_2 is related to the inlet velocity V_0 by the relation

$$V_2 \equiv V_0 \cdot \frac{2f + b}{2f + 2q + b} \qquad (3)$$

The relation collapses into the relationship used for the common slot and annular die cases where no constriction occurs ($V_0 = V_2$). Specifically, Equation 3 collapses into the non-dimensionalization used by KSP for slot dies and the non-dimensionalization used by MSP for annular dies. For our work, the axial position Z was non-dimensionalized by dividing by the outer diameter (D_o) of the jet outlet.

Figures 3.6 and 3.7 show the use of V_2 for producing non-dimensionalized mean axial velocity profiles. With V_2, comparisons of different die geometries are possible. For the lower 17.3 m/s inlet air velocity (Figure 3.6), the simulations from

all die angles fall along the same non-dimensional curve. The simulations for upper air inlet velocity show similar results, but there is a clear pattern of decreasing peak non-dimensional velocity with increasing die angle. For all the dies examined, the peak magnitude and the peak position of the flow reversal increases with die angle.

Figure 3.8 shows a comparison of non-dimensionalized velocity profiles for the 40° and 70° degree slot angles and both inlet air velocities. The coincidence of three of the profiles is fairly good. However, the profile for the 40° slot angle and 34.6 m/s air velocity diverges from the other curves. The peak mean velocity for this case is higher than for any other in this work; the non-linear gas compressibility effects encountered are likely causing the difference. The nominal mean exit velocity V_2 for this case is 186 m/s, which is just over half the ambient speed of sound.

Figure 3.9 shows a comparison of dimensionless mean axial velocity profiles for our 60° tapered die and profiles from KSP for a 60° slot die. The difference in mean velocity peak shape is one major difference, and another difference is the magnitude of the flow reversal. The tapered die profiles show a lower overall velocity peak, and the profiles also decay more quickly at increasing distances from the die face. The maximum flow reversal for the tapered die is significantly stronger than reversal for the slot die (examine the abscissa values between 0 and 0.5).

Figure 3.10 shows a comparison of our tapered die simulations with simulations from MSP for a conventional annular die. There is a substantial difference in velocity profiles between the annular and tapered dies. The annular die has a much broader velocity peak and a slower decay. Slightly higher peak velocities are reached with the tapered die, and these velocities decay quickly with substantial

decay by Z / D_o =15. Flow reversal is present for both the annular die and the tapered dies; however, the tapered dies have peak reversals at lower levels than the conventional annular die.

While mean air velocity is important in die design, turbulence must also be taken into account in designing and selecting melt blowing dies. Figures 3.11 and 3.12 show the spinline turbulent kinetic energy (TKE) for the tapered dies. In both figures the TKE is non-dimensionalized by dividing by $(V_2)^2$, while position is non-dimensionalized (as before) by dividing by D_o. The locations of the kinetic energy minimums on the graphs correspond very well with the maximum velocity locations. This behavior is expected, as the generation of turbulent kinetic energy is proportional to the velocity gradient. Another feature to notice is the shift in the minimum value of the first TKE trough when the die angle is increased from 45° to 50°. From the die face to $Z / D_o = 4$, the TKE for 40° and 45° dies is approximately half that of higher angle dies. This reduction in turbulence could impact the performance characteristics of dies of this type. TKE is proportional to the square of the velocity, so while magnitudes shown in Figures 3.11 and 3.12 are similar, the actual TKE quantities are substantially different; this comparison is given in Figure 3.13 for 40° and 70° dies.

Comparing the TKE profiles of slot, annular and tapered dies shows significant differences. Figure 3.14 compares the 60° tapered die with the 60° slot die studied in KSP. It is apparent that the near field TKE is much higher for the slot die. Also note that, while the tapered die shows a strong minimum near $Z / D_o = 2$, the slot die shows only a relatively minor plateau. Figure 3.15 shows a comparison between

the 60° tapered die and the annular die studied in MSP. Here, the tapered die shows much higher near field TKE. Also note that, while the basic two-peak shape is common for both geometries, the annular case has both peaks spread out and shifted away from the die face.

Figures 3.16 and 3.17 show the turbulent dissipation rate (ε) profiles. It is apparent from these figures that, while the profiles in the jet decay region are similar, there are substantial differences in the near-die region. The first troughs in the curves have much lower magnitudes for the 40° and 45° dies than for the others. This difference echoes the differences seen in the TKE profiles in Figures 3.11 and 3.12. Figure 3.18 compares the 60° tapered die against the 60° slot die from KSP. Mirroring the differences in TKE, the ε profile for the tapered die is much lower. Also similar to the TKE results, the tapered die clearly shows a two-peak profile, while the slot die shows only a single maximum. Comparison with the annular die also shows large differences in ε profiles. Again similar to the TKE results, Figure 3.19 shows much higher values of ε for the tapered die in the near-field region.

Figure 3.20 shows the mean axial velocity contour plot for the 45° die with an inlet velocity of 34.6 m/s. Note that the peak mean axial velocities are not along the spinline; rather, the highest velocities seen in the flow field are just off the centerline. Now, these flow properties away from the centerline can have a large impact on the fiber formation process. For example, when the die is operated at high air throughputs, a melt blown fiber will have significant vibration in the transverse (r) direction. This vibration exposes the fiber to different regions of the jet flow field.

In Figure 3.20 the spinline mean velocity stays below its maximum for Z = 0 to about Z = 5 mm. This behavior is expected, as some space is needed for the jets to merge. Note that the geometric convergence point of the die taper varies from Z = 1.12 mm to Z = 3.67 mm as θ is varied from 40° to 70°. Similar convergence behavior in gas jets is observed in both MSP and Lai and Nasr (1998).

Figure 3.21 shows contours of turbulent kinetic energy for the 45° die with an inlet velocity of 34.6 m/s. Prior to the jet converging a great deal of turbulence is generated by the flow separation at the nosepiece. However, once the jet is converged, most of the turbulence is generated at the edges of the jet, rather than the center; this phenomenon also was observed in KSP. These multiple regions of turbulence generation cause the peak areas of turbulent kinetic energy to be away from the centerline until the jet is fully developed.

3.4 Conclusions

In this work the velocity flow fields below tapered melt blowing dies were studied using computational fluid dynamics (CFD). The fields produced by dies with five different die angles were compared. The ideal-gas compressibility model was used due to the high local velocities encountered. It was found that with appropriate non-dimensionalization, the centerline (spinline) velocity profiles were very similar throughout the die angle range studied. The results for a 60° tapered die were compared to previous, experimentally verified results for both a 60° slot die and a conventional annular die. Several differences were noted between the taper die and conventional annular and slot dies. For tapered dies, the centerline mean velocity

peak behavior was found to be intermediate between that of the conventional die designs. Tapered dies show the broadened velocity peak also observed in conventional annular dies. This is in contrast to the sharp peak found with slot die designs. It was also found that, with the tapered die, the velocity decayed more quickly in the far field.

Besides velocity fields, turbulent behavior of tapered jets was also examined. It was found that, for near-die locations, normalized turbulent kinetic energy was much lower for shallow die angles of 45° and less. As with the velocity fields, the turbulent behavior of the tapered die was intermediate between the previous results for slot and annular dies. For both TKE and ε, the slot die shows the highest values, tapered die profiles are intermediate, with the lowest turbulence quantities determined for the annular die. Turbulence profiles for the tapered dies are quantitatively similar to the annular die profiles and significantly different from slot die profiles.

3.5 Nomenclature

b = face slot width as shown in Figure 3.3 (mm)

d = slot width as shown in Figure 3.3 (mm)

D_o = 2*(f + b) ; the outer diameter of annular outlet (mm)

D_i = the inner diameter of the annular outlet as shown in Fig. 1 (mm)

f = nosepiece radius as shown in Figure 3.3 (mm)

h = die slot outer edge distance as use by KSP for slot dies (mm)

k = turbulent kinetic energy (m^2/s^2)

q = inlet offset as shown in Figure 3.3 (mm)

r = radial coordinate as defined in Figure 3.3 (mm)

s_{ij} = fluctuating rate of strain tensor (s^{-1})

u_i = i^{th} component of fluctuating velocity (m/s)

V_0 = mean inlet velocity as shown in Figure 3.3 (m/s)

V_2 = mean jet exit velocity as shown in Figure 3.3 (m/s)

Z = spatial coordinate (mm)

Greek Characters

ε = turbulent dissipation rate (m^2/s^3)

ν = kinematic viscosity (m^2/s)

θ = die angle (°)

3.6 References

Allen, M.A.; Fetcko, J.T. "Modular melt blowing die" U.S. Patent 5,618,566, **1997**.

Brackmann, W.A.; Diianni, D. "Formation of Polymeric Fibers", U.S. Patent 3,888,610, **1975**.

Harpham, A.S.; Shambaugh, R.L. "Flow Field of Practical Dual Rectangular Jets" *Ind. Eng. Chem. Res*. **1996**, *35*, 3776-3781.

Harpham, A.S., and Shambaugh, R.L., "Velocity and Temperature Fields of Dual Rectangular Jets", *Ind. Eng. Chem. Res.* **1997**, *36*(9), 3937-3943.

Krutka, H.M.; Shambaugh, Robert L.; Papavassiliou, Dimitrios V. "Analysis of a Melt-Blowing Die: Comparison of CFD and Experiments." *Ind. Eng. Chem. Res.*, **2002**, *41*, 5125-5138.

Lai, J.C.S.; Nasr, A. "Two parallel plane jets: comparison of the performance of three turbulent models", *Proc. Instn. Mech. Engrs.*, **1998**, *212*, 379-391.

Launder, B.E., G. J. Reece, and W. Rodi. "Progress in the Development of a Reynolds-Stress Turbulence Closure." *J. Fluid Mech.*, **1975**, *68*, 537-566.

Moore, E.M.; Shambaugh, R.L.; Papavassiliou D.V. "Analysis of Isothermal Annular Jets: Comparison of CFD and Experimental Data" submitted to *J. Appl. Polym. Sci*., (2004)

Nasr, A.; Lai, J.C.S. "Comparison of flow characteristics in the near field of two parallel plane jets and an offset plane jet." *Phys. Fluids*, **1997**, *9*(10), 2919-2931.

Pope, S.B. Turbulent Flows; Cambridge University Press: Cambridge, United Kingdom, pp. 134-135, **2000**.

Schlichting, H., Boundary-Layer Theory 7th ed., McGraw-Hill, pp. 729-735, **1979**.

Schwarz, E. "Apparatus and Process for Melt-Blowing a Fiberforming Thermoplastic Polymer and Product Produced Thereby", U.S. Patent 4,380,570, **1983**.

Shambaugh, R.L. "A macroscopic view of the melt blowing process for producing microfibers." *Ind. Eng. Chem. Res.* **1988**, *27*(12), 2363-2372.

Tate, B.D., Shambaugh, R.L. "Modified Rectangular Jets for Fiber Production." *Ind. Eng. Chem. Res.*, **1998**, *37*, 3772-3779.

Uyttendaele, M.A.; Shambaugh, R.L. “The Flow Field of Annular Jets at Moderate Reynolds Numbers.” *Ind. Eng. Chem. Res.*, **1989**, *28*, 1735-1740.

Wilcox, D.C., Turbulence Modeling for CFD, DCW Industries, La Canada, California, **1994.**

Zhao, R. “Melt Blown Dies: A Hot Innovation Spot”, *Int. Nonwovens J.*, **2002**, *11*(4), 37-41.

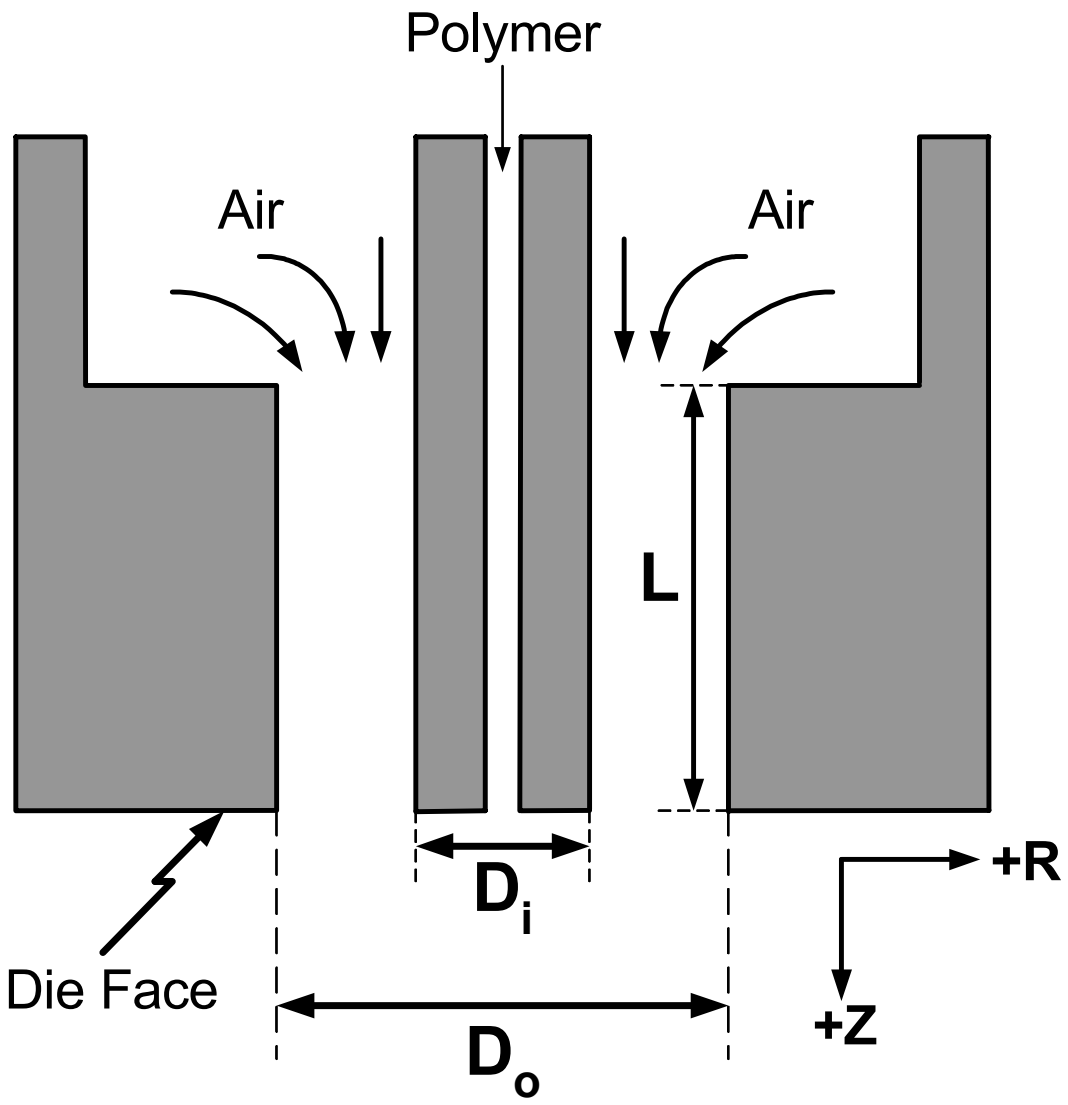

Figure 3.1. A cross-sectional view of the annular melt blowing die. The origin of the coordinate system is in the plane of the die face and at the center of the polymer outlet.

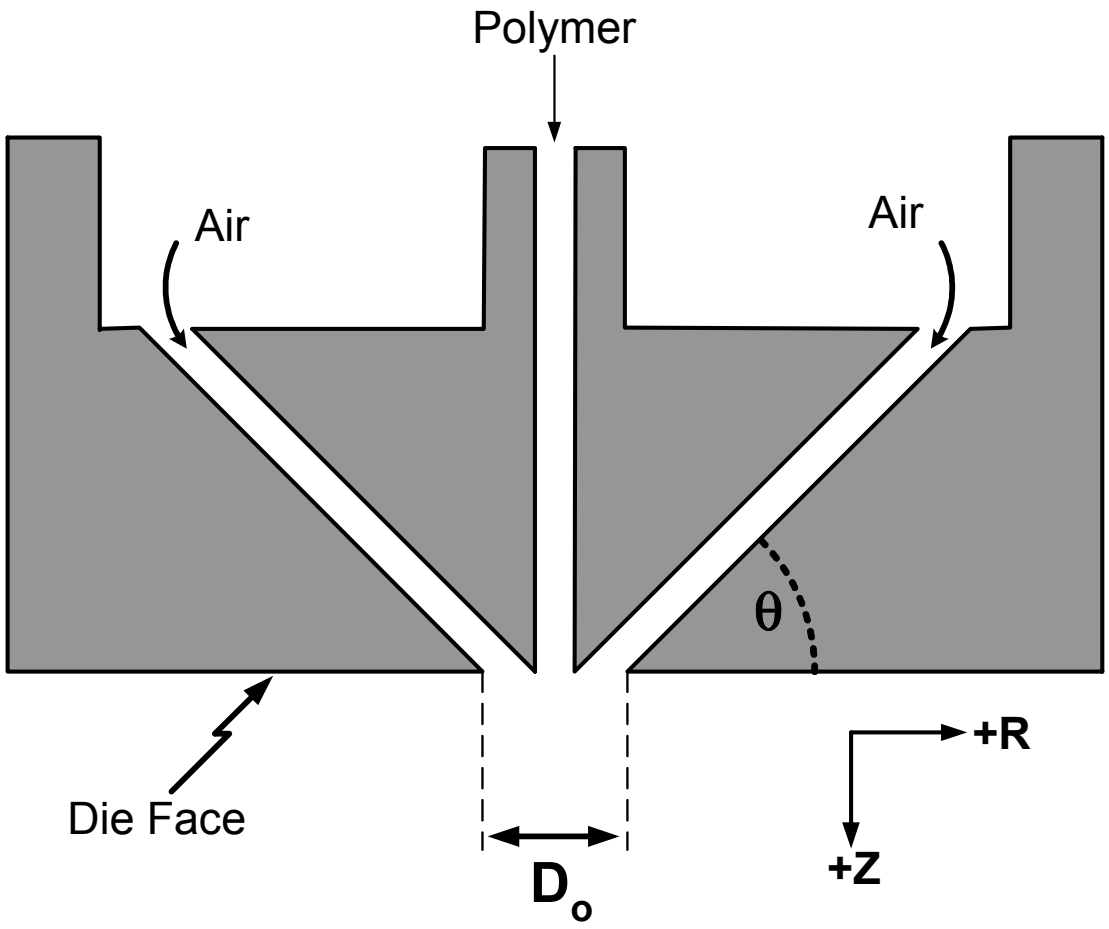

Figure 3.2. A cross-sectional view of the tapered melt blowing die. The origin of the coordinate system is in the plan of the die face and at the center of the polymer outlet.

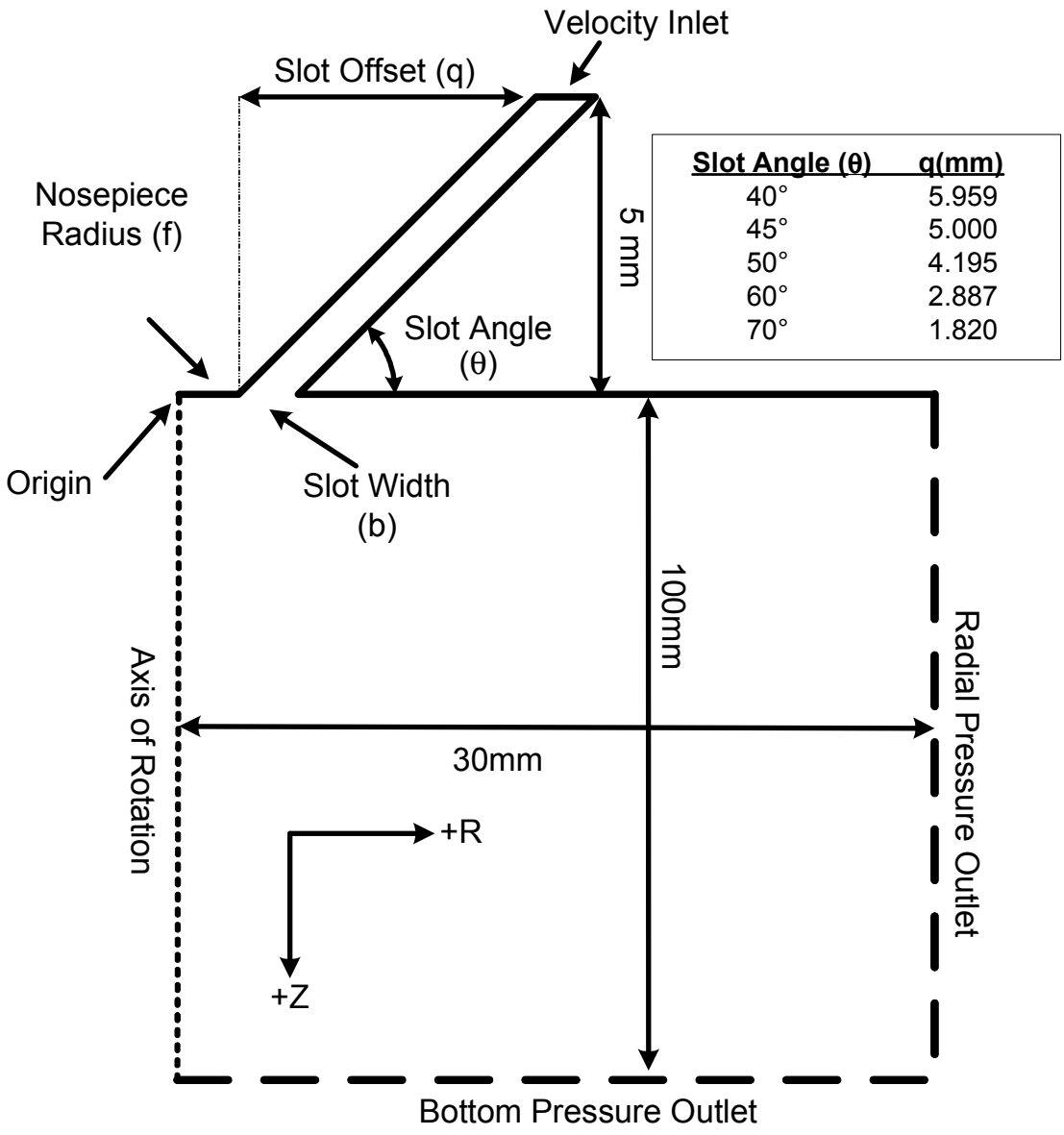

Figure 3.3. The computational domain used in the simulations. For all simulations, f = 1.01 mm and b = 0.65 mm.

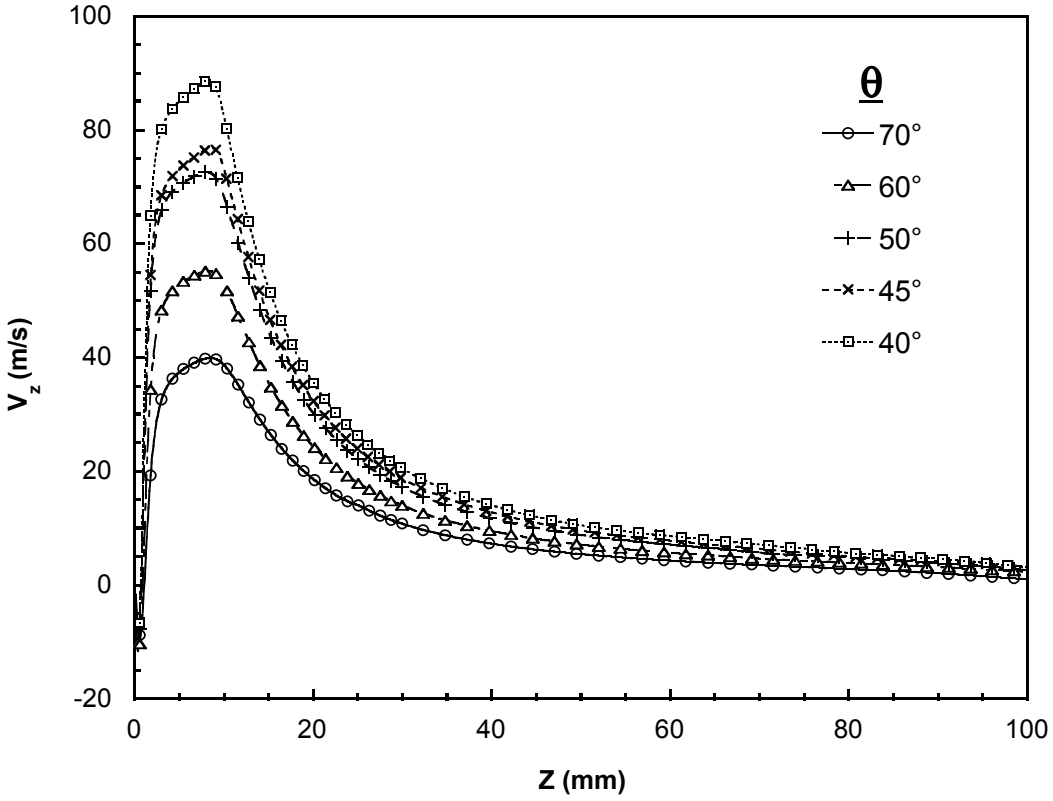

Figure 3.4. The effect of die angle on the centerline mean axial velocity profile (V_o = 17.3 m/s).

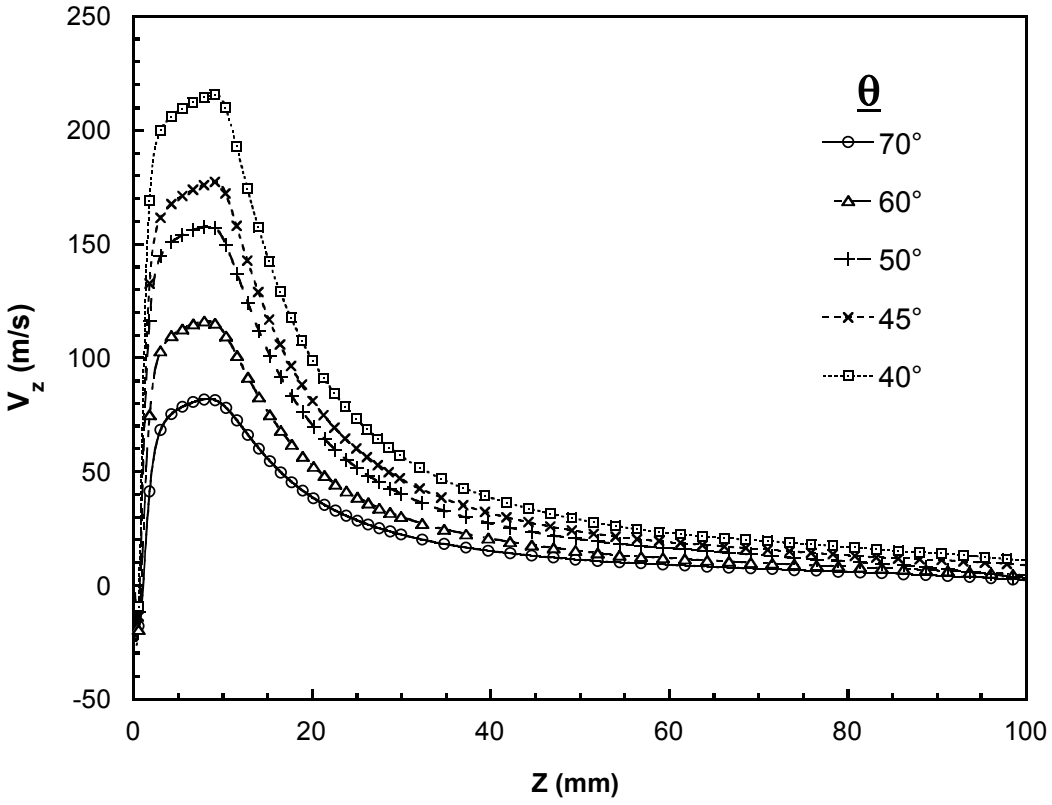

Figure 3.5. The effect of die angle on the centerline mean axial velocity profile (V_o = 34.6 m/s).

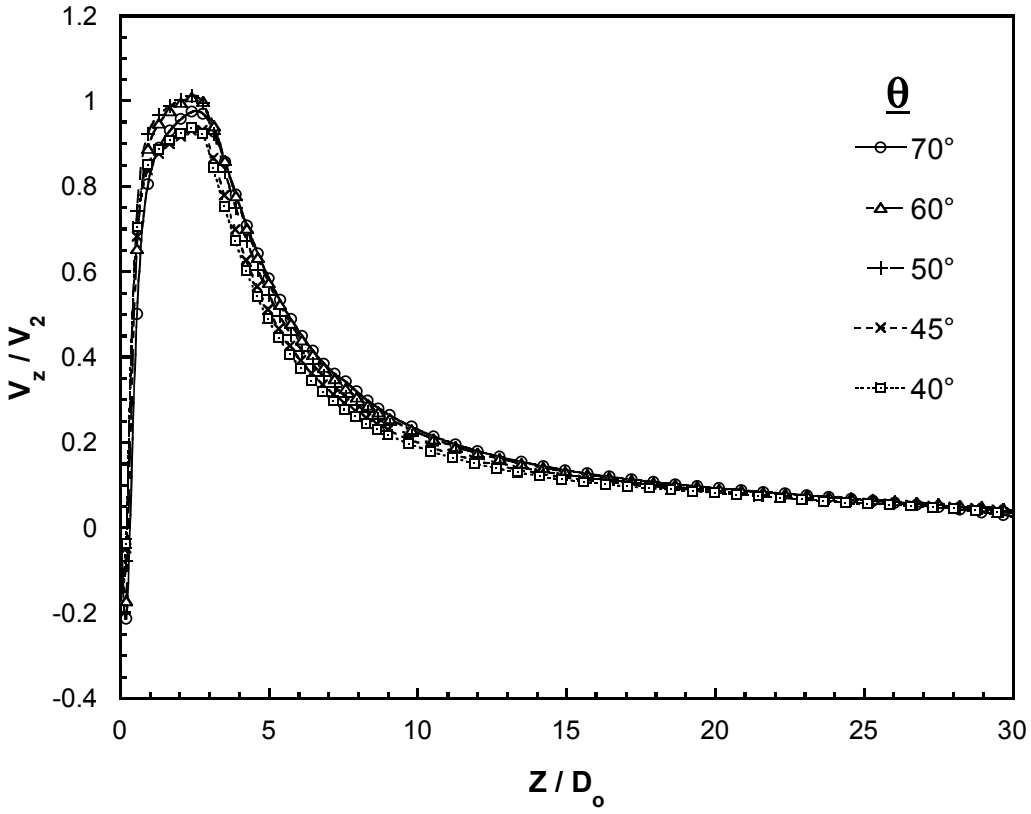

Figure 3.6. The centerline mean axial velocity profile. Nondimensionalization was done by using D_o and V_2. For these profiles, V_o = 17.3 m/s.

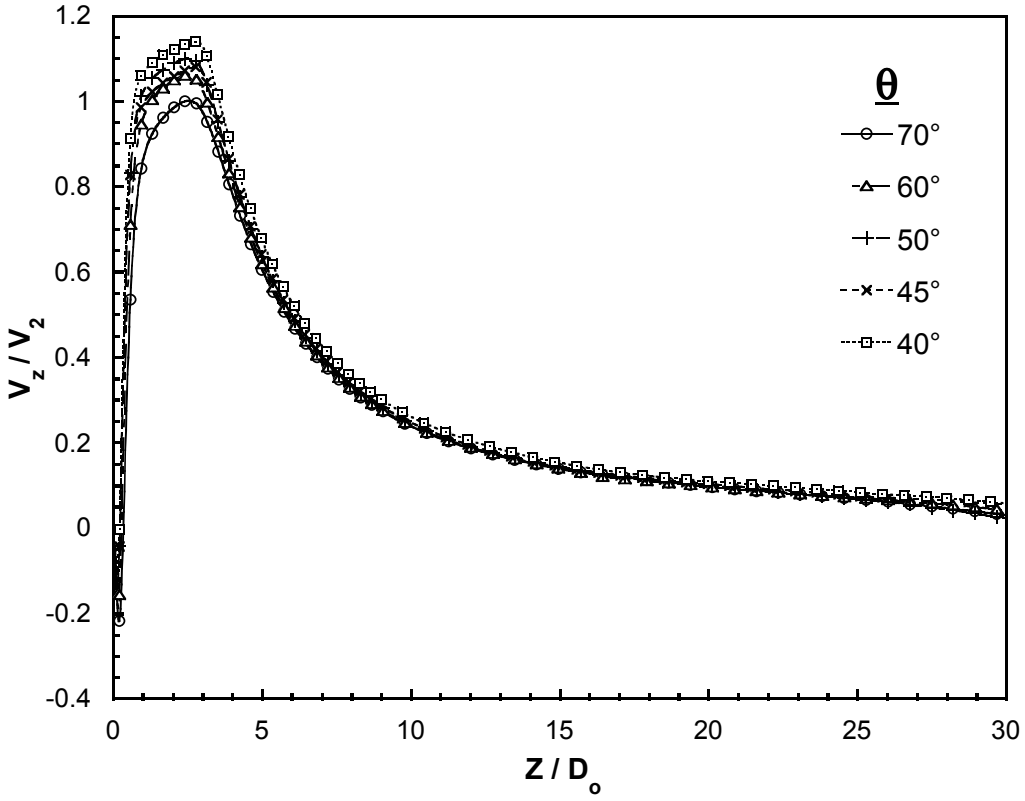

Figure 3.7. The centerline mean axial velocity profile. Nondimensionalization was done by using D_o and V_2. For these profiles, V_o = 34.6 m/s.

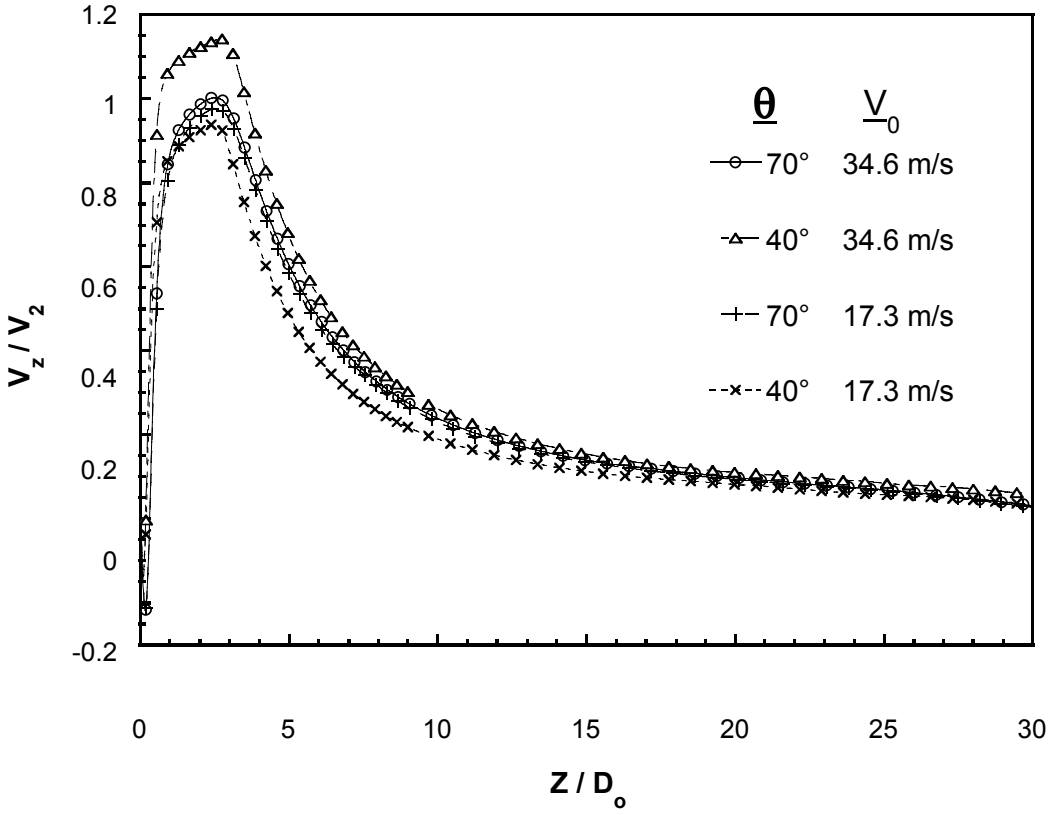

Figure 3.8. Comparison of nondimensionalized mean axial velocity profiles.

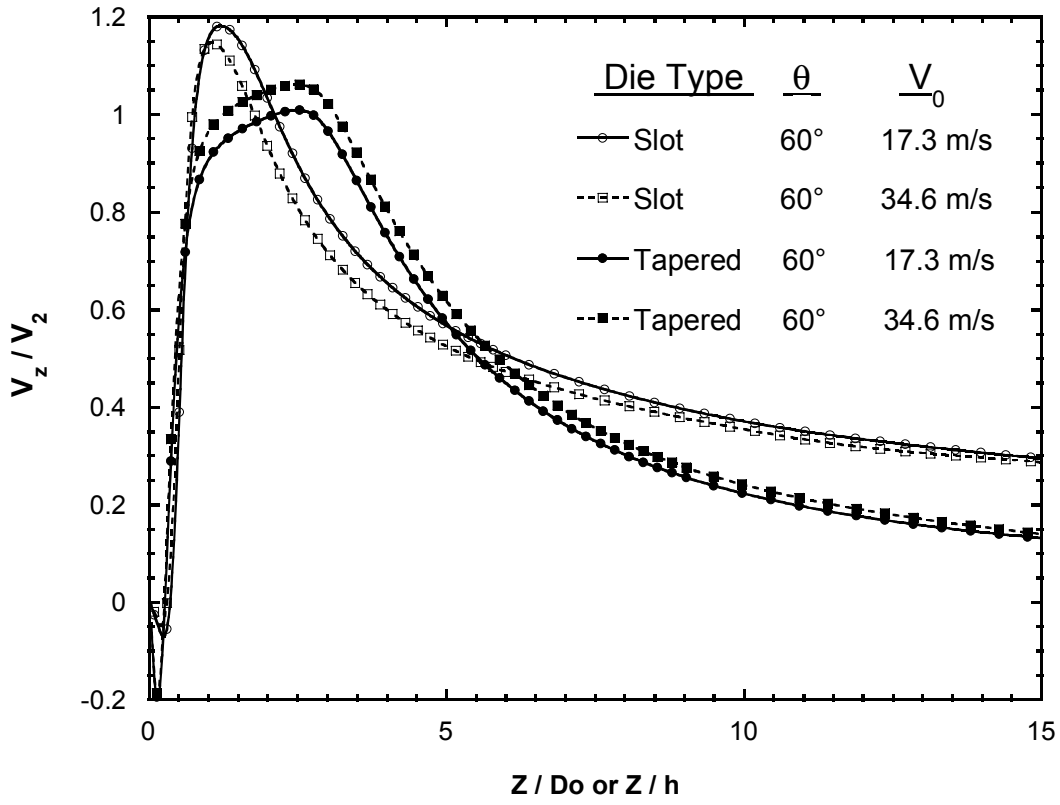

Figure 3.9. Comparison of mean axial velocity profiles for tapered and slot dies. The slot die data are from KSP.

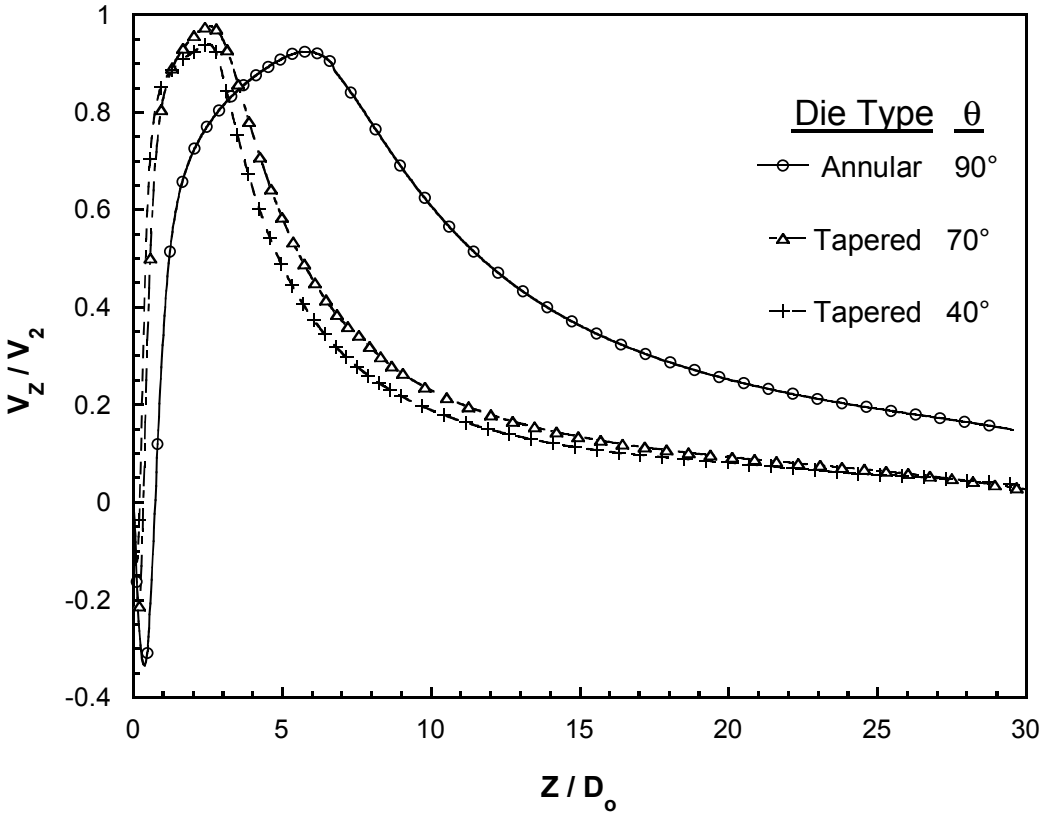

Figure 3.10. Comparison of mean axial velocity profiles for tapered and annular dies. The annular die data are from MSP.

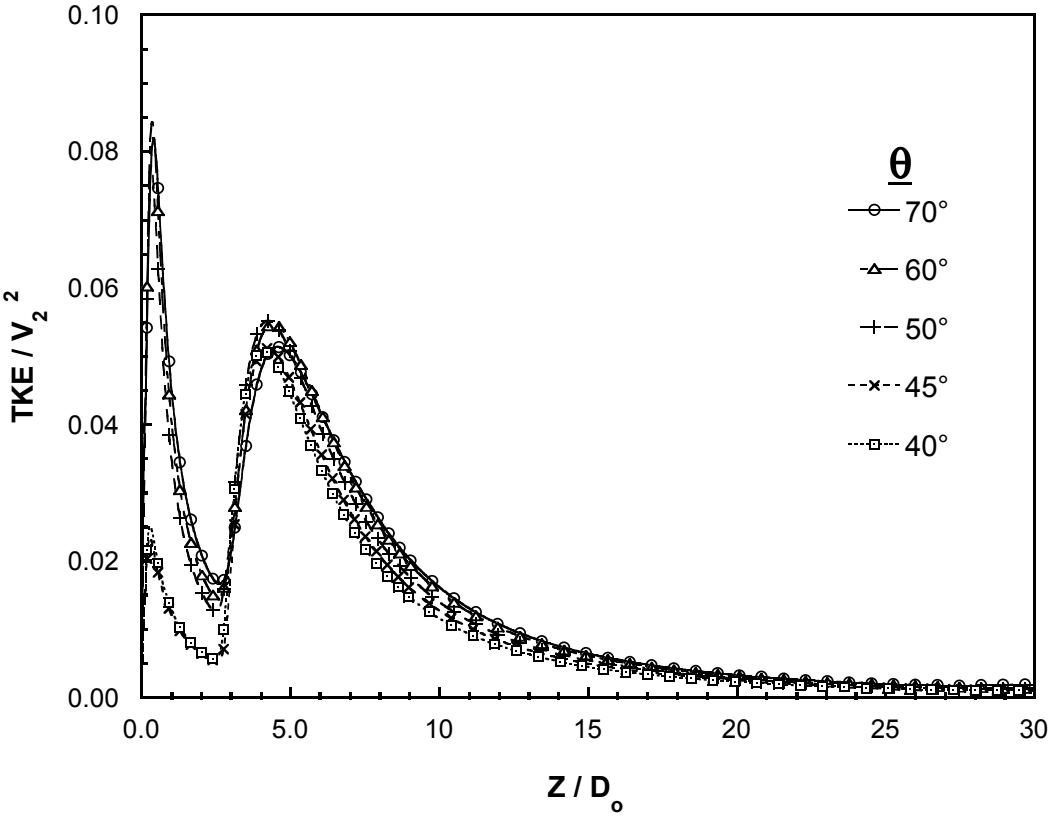

Figure 3.11. The centerline turbulent kinetic energy profile. Nondimensionalized was done by using D_o and V_2. For these profiles, V_o = 17.3 m/s.

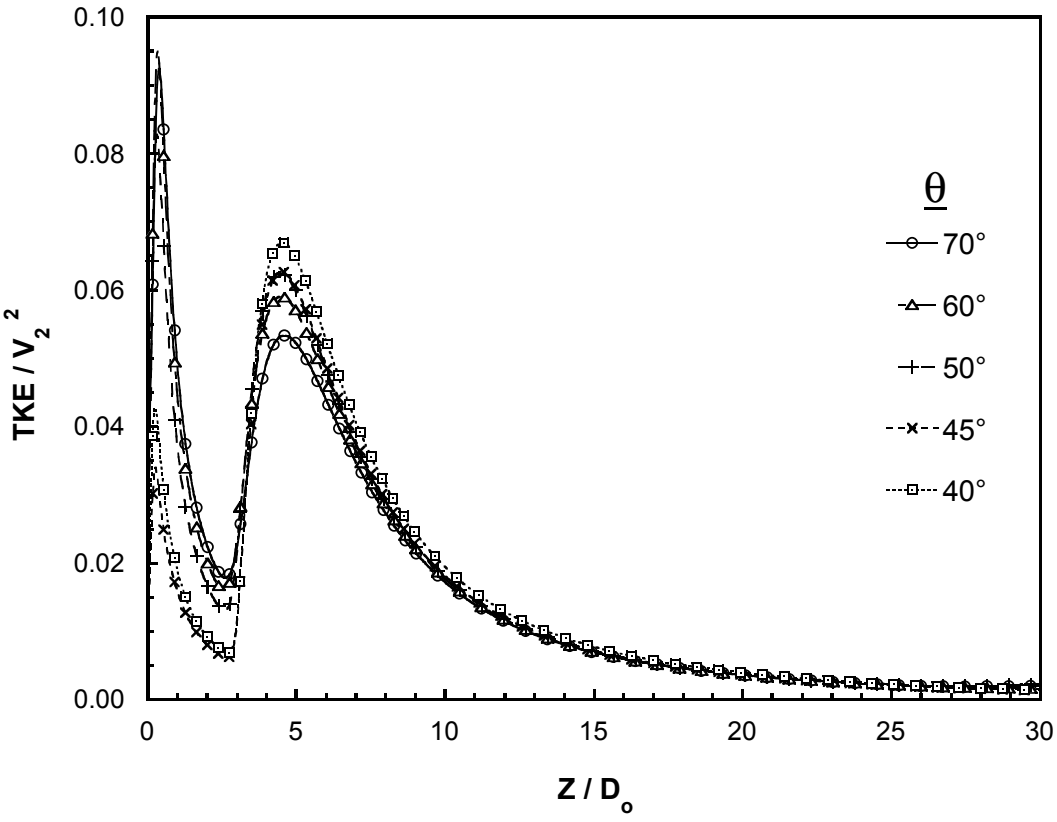

Figure 3.12. The centerline turbulent kinetic energy profile. Nondimensionalization was done by using D_o and V_2. For these profiles, Vo = 34.6 m/s.

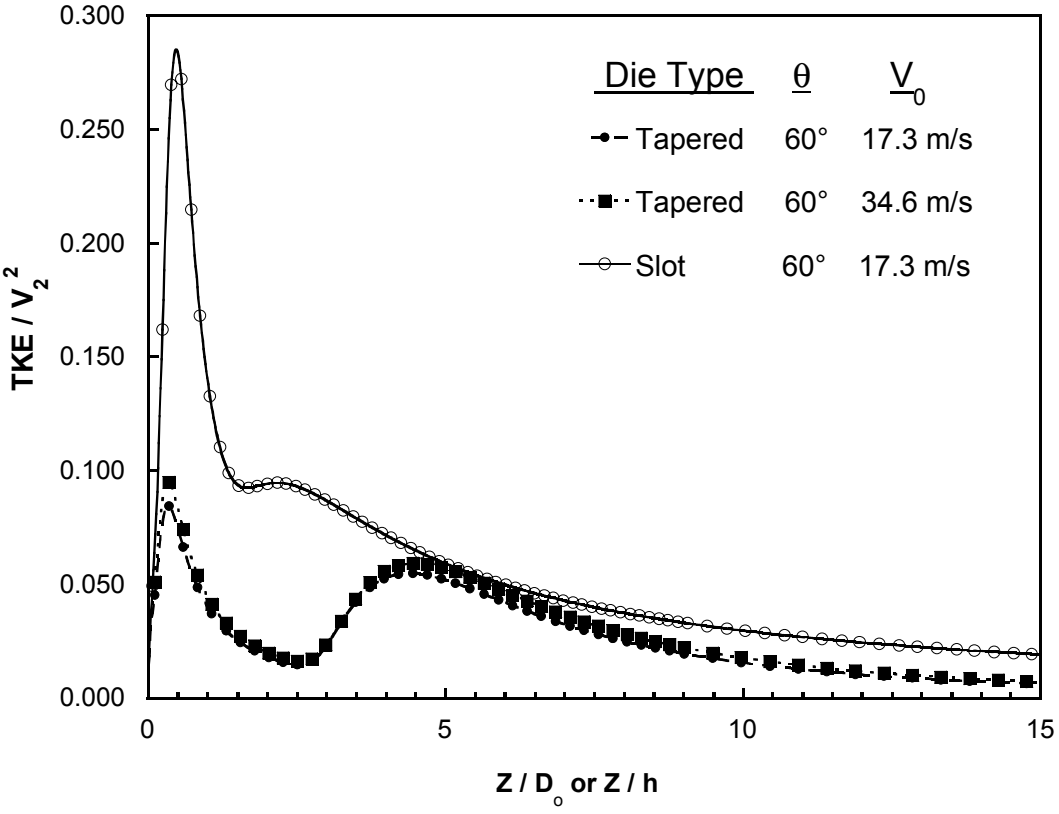

Figure 3.13. Comparison of centerline turbulent kinetic energy profiles for $\theta = 40°$ and $70°$ and for $V_o = 17.3$ m/s and 34.6 m/s.

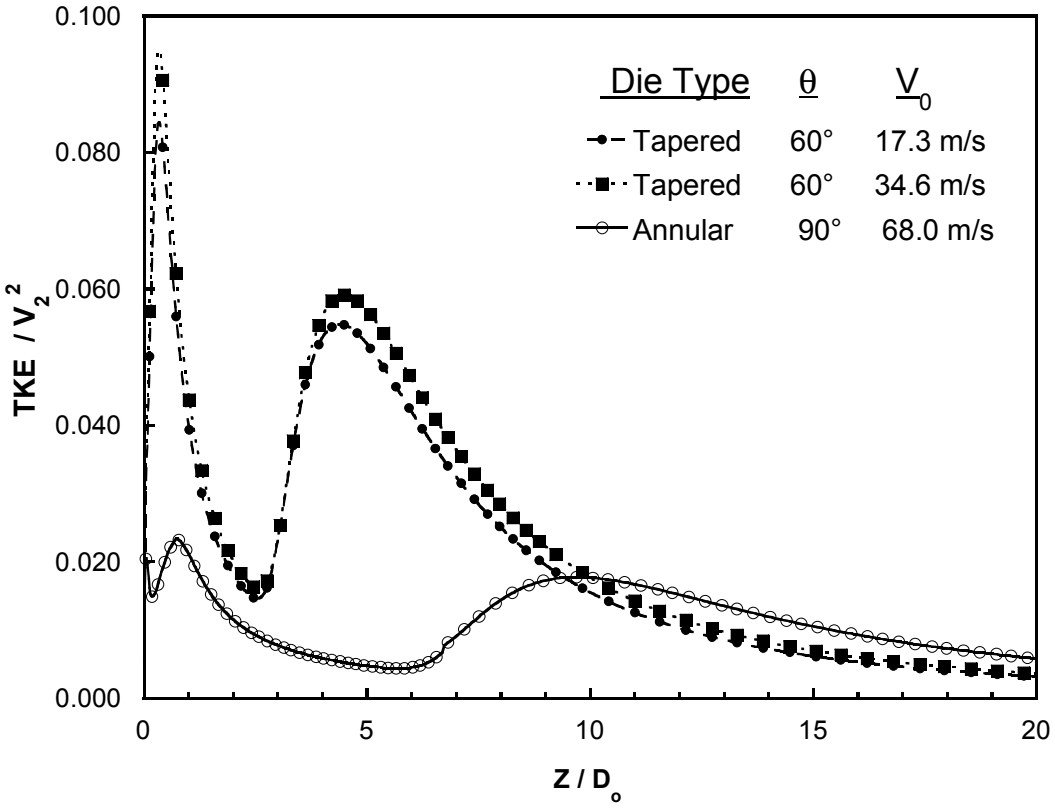

Figure 3.14. Comparison of turbulent kinetic energy profiles for tapered and slot dies. The slot die data are from KSP.

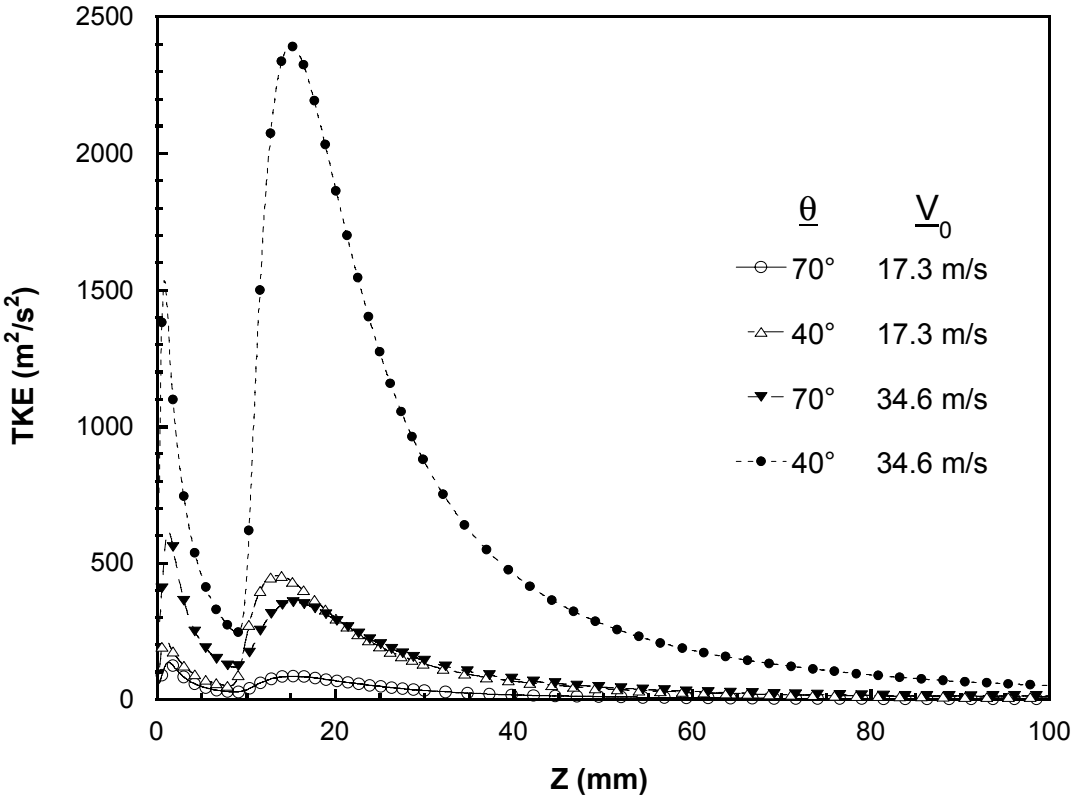

Figure 3.15. Comparison of turbulent kinetic energy profiles for tapered and annular dies. The annular die data are from MSP.

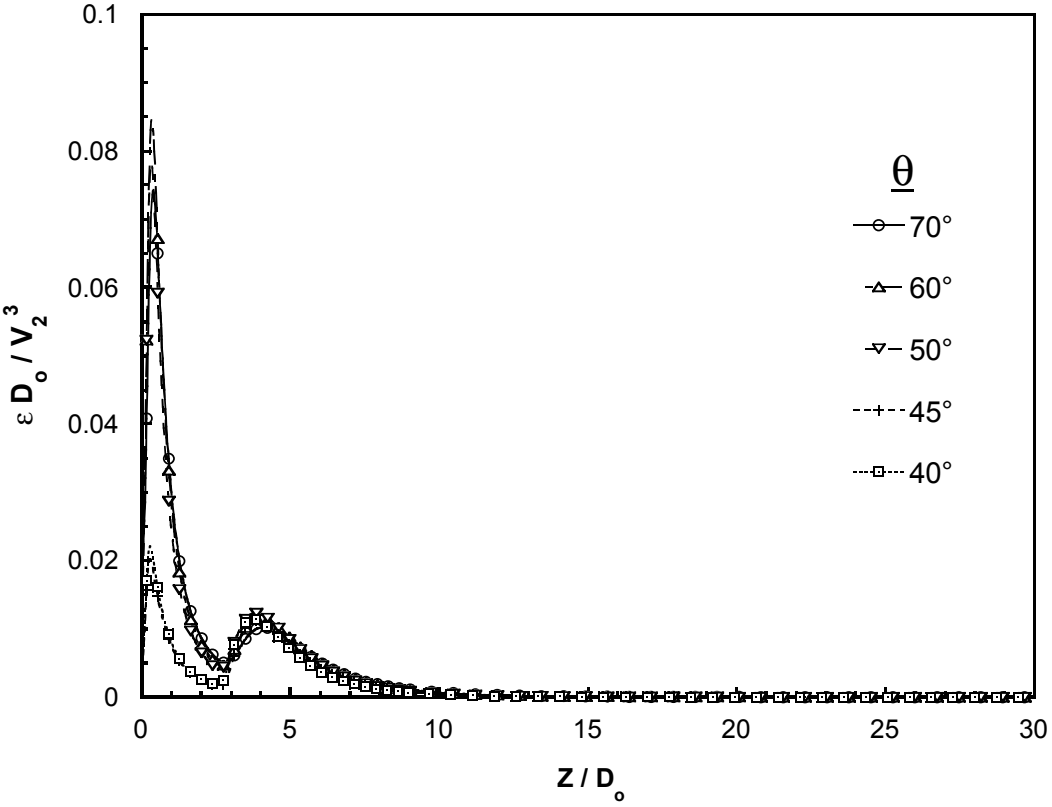

Figure 3.16. Centerline turbulent dissipation rate profiles. Nondimensionalization was done by using D_o and V_2. For these profiles, V_o = 17.3 m/s.

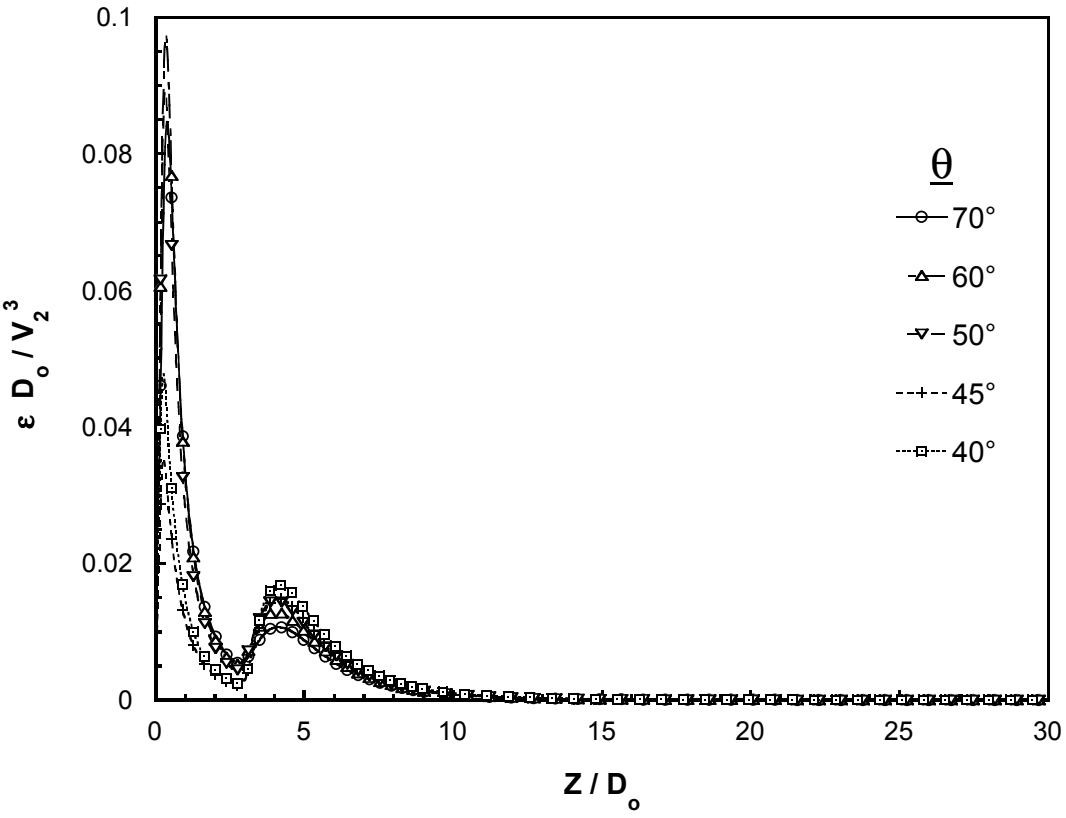

Figure 3.17. Centerline turbulent dissipation rate profiles. Nondimensionalization was done by using D_o and V_2. For these profiles, V_o = 34.6 m/s.

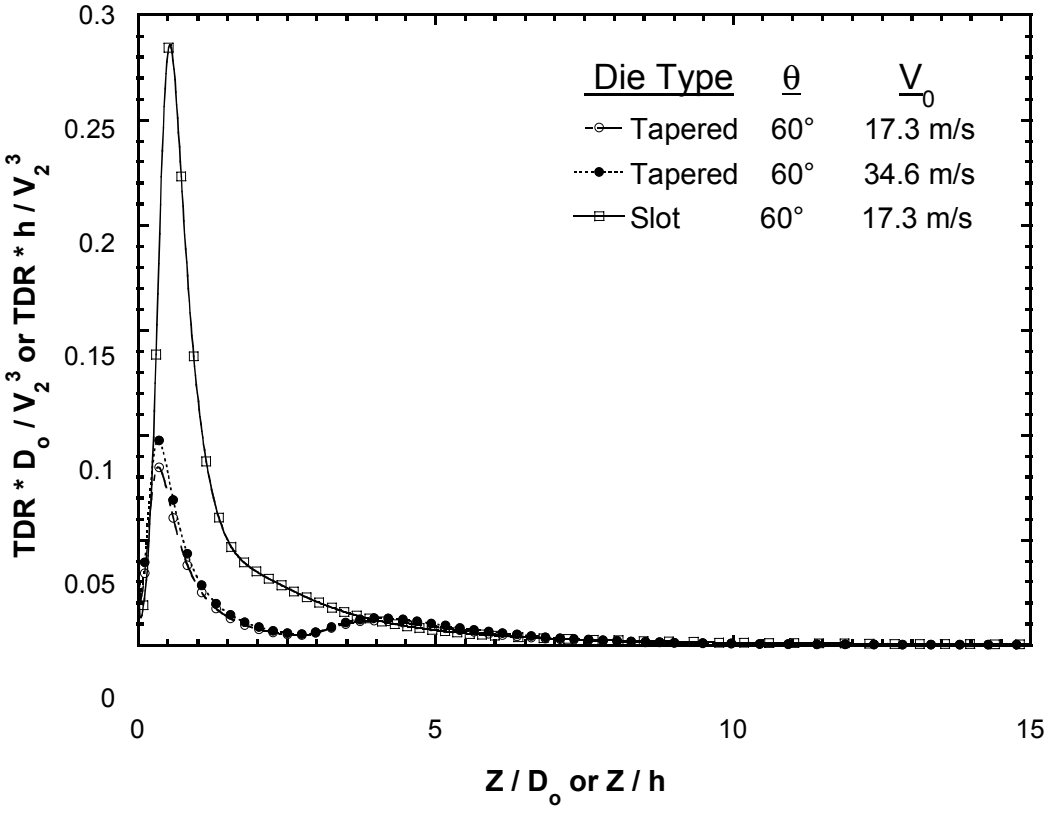

Figure 3.18. Comparison of turbulent dissipation rate profiles for tapered and slot dies. The slot die data are from KSP.

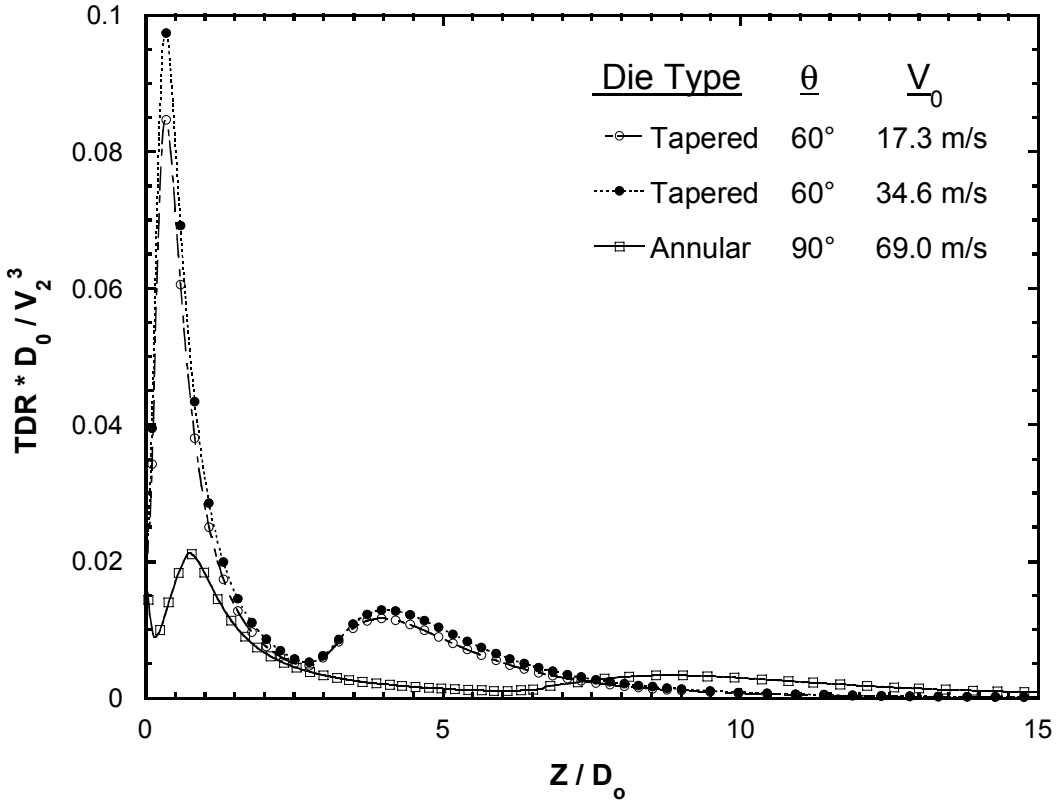

Figure 3.19. Comparison of turbulent dissipation rate profiles for tapered and annular dies. The annular die data are from MSP.

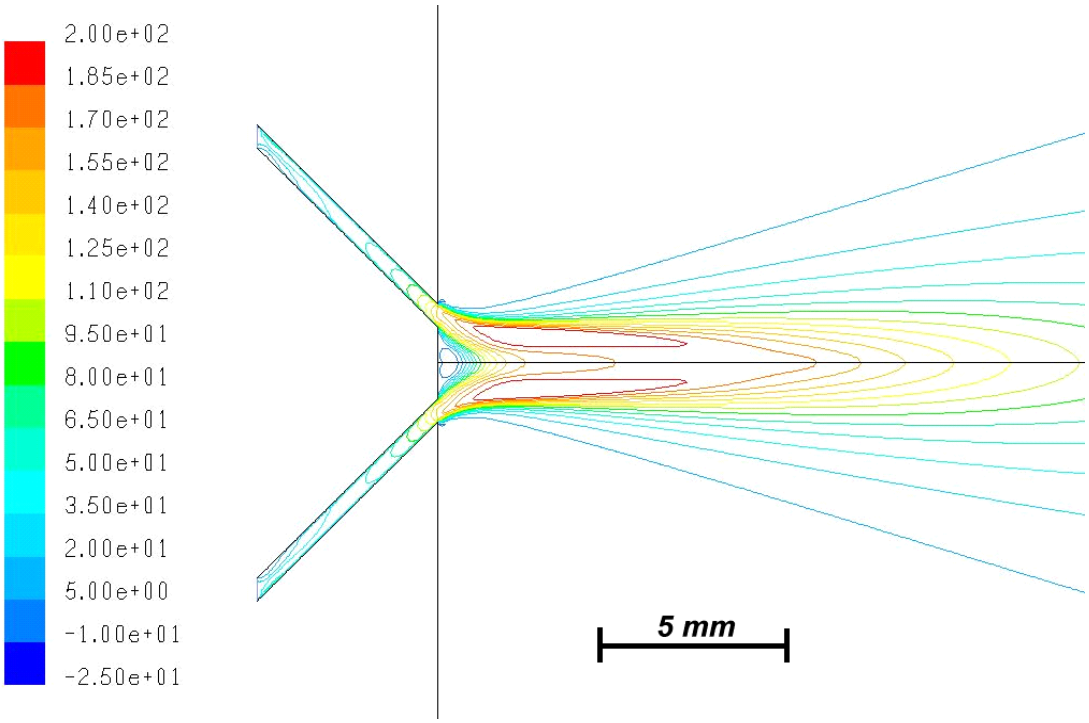

Figure 3.20. Contour plot of mean axial velocity for $\theta = 45°$ and $V_o = 34.6$ m/s.

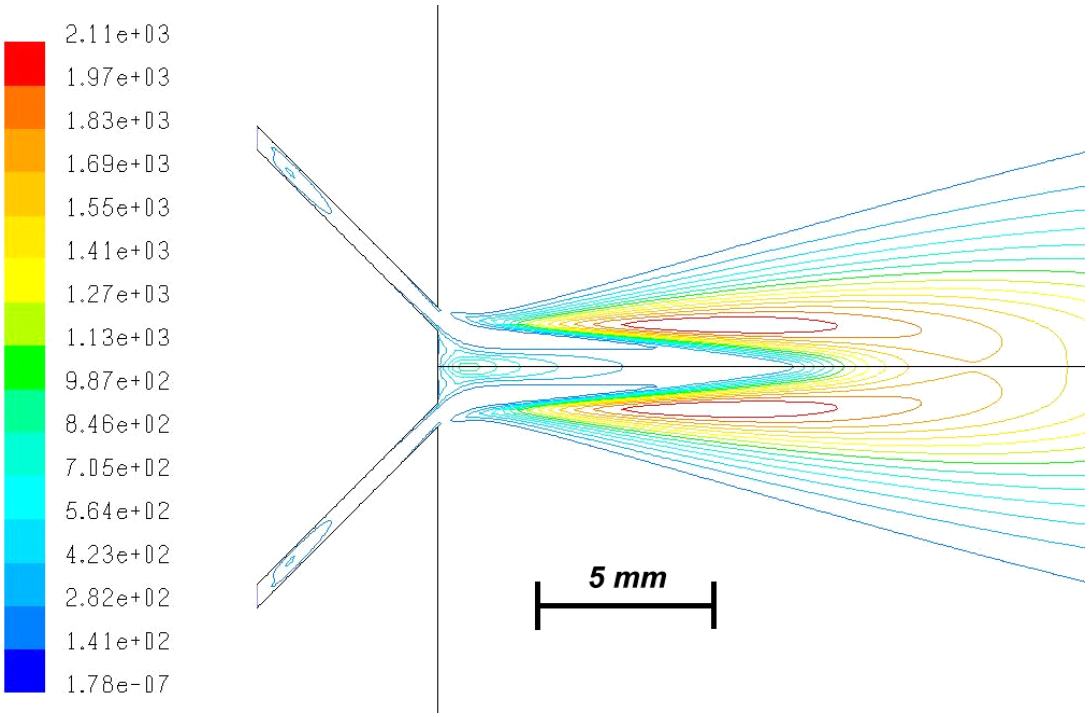

Figure 3.21. Contour plot of turbulent kinetic energy for $\theta = 45°$and $V_o = 34.6$ m/s.

Chapter 4

Ensemble Laser Diffraction for Online Measurement of Fiber Diameter Distribution during the Melt Blowing Process

(This chapter has been accepted for publication in International Nonwovens Journal as: Moore, E.M., Papavassiliou, D.V., Shambaugh, R.L. "Ensemble Laser Diffraction for Online Measurement of Fiber Diameter Distribution during the Melt Blowing Process")

4.1 Abstract

Online measurements of the fiber diameter distribution during a melt blowing process were taken using a new laser diffraction technique. This technique measured both the attenuation of the fibers as well as entanglement of the fibers into bundles at

large distances from the die. A pilot scale unit with a 20.3 cm (8 inch) slot die was used for the studies. Commercial polypropylene polymer was used. Both the spinline attenuation and fiber bundling were measured as a function of position both below and across the die face.

4.2 Introduction

Melt blowing is a process where heated air jets are used to attenuate molten polymer streams into fibers. These fibers are then collected for either direct use or further processing. A schematic of melt blowing equipment is shown in Figure 4.1. The key piece of equipment is the die, below which the heated air and polymer make contact. Because the fibers are directly laid down as a web on the collection device (with no weaving or knitting required), the material is classified as a nonwoven. Nonwovens are a large and growing industry: in 1997 nonwovens producers in the United States had sales in excess of 3.8 billion U.S. dollars (Marlow-Ferguson, 2001). Melt blown fibers are commonly used for filtration, personal hygiene, and absorption applications.

Melt blown fibers exhibit a statistical distribution in their diameters due to the somewhat chaotic process of high-speed attenuation with air. Since size distribution largely determines the finished web properties, the measurement and control of size distribution is of great industrial importance. Ensemble laser diffraction (ELD) provides a method for measuring fiber diameter distribution both while the fiber formation process is still taking place (online) and after the fiber has been formed (offline). Online measurements are important for understanding, controlling and

modeling the melt blowing process. The online measurement capability provided by ELD can only currently be matched using either laser Doppler velocimetry (LDV) or high-speed photography (and related particle imaging techniques). Both LDV and photographic techniques have limitations in their application to the melt blowing process. In LDV, the measuring volumes, which are typically 1 mm in diameter, are difficult to effectively target on a rapidly vibrating fiber stream. Since LDV only measures the velocity of the fiber, diameter data must be acquired through mass balances. These mass balance calculations require a model for the polymer density that makes the use of LDV a somewhat empirical technique for analyzing multi-hole melt blowing. The work of Bansal and Shambaugh (1996) describes the process of determining polymer density of a filament during the fiber formation process. High-speed photography has its own limitations that include (a) proper illumination by flash, lasers, or other means; (b) obtaining correct depth of field; and (c) resolving the small diameter fibers from either chemical or digital photographs. Yin et al. (1999) used a high-powered pulse laser to provide the necessary illumination for digital imaging. However, even with this sophisticated equipment, online diameter determination was only possible very near the die.

The work described herein applies ELD to the online measurement of fiber diameter during the melt blowing process. This ELD method provides data that are difficult to obtain through other methods. Furthermore, ELD provides fiber distributions in near real-time, without interfering with the fiber formation process.

4.3 Experimental Methods

4.3.1 Ensemble Laser Diffraction

Ensemble laser diffraction (ELD) works by passing a collimated laser beam through a group of fibers and measuring the scattering of the transmitted light. The radial scattering profile is directly related to the diameter distribution of the fibers present within the sampling volume. The sampling volume for the FibrSizr® unit (Powerscope, Inc., Minneapolis, MN) is a cylinder that is 12 millimeters in diameter and up to 200 millimeters in length. The sample, either a fiber mat or fiber stream, can lie in almost any orientation relative to the sampling volume. Figure 4.2 illustrates the use of the FibrSizr® unit. The scattering of the light is measured using a central sensor and a series of concentric sensor arcs. Primarily based on the Mie scattering model (Mie, 1908), the forward scattering of the light is used to measure the fiber diameter distribution of a given sample. Similar technology has already been applied to particle sizing applications (Black et al., 1996). The calculation scheme based on the scattering data is iterative; this iterative process is depicted in Figure 4.3. The raw scattering data are taken at the detector, and then the data are sent to a computer for analysis. A multiple regression technique is used to compute what fiber diameter distribution would produce the observed laser scattering. Since this method is based on the accuracy of the scattering model, calibration is necessary. The manufacturer of the unit conducted an extensive calibration of the scattering model wherein the ELD measurements were verified by both scanning electron microscopy (SEM) and optical microscopy; see Fandrey and Naqwi (2003). These

researchers found that the laser scattering technique gave very good agreement with both SEM and optical measurements.

4.3.2 Die and Extruder Unit

The experiments were conducted on a pilot scale melt blowing line at the 3M Nonwovens Technology Center in St. Paul, Minnesota. An eight-inch wide slot die of drilled design was used in this line; see 4.4. The die was oriented horizontally such that the fiber curtain was parallel to the ground. The die had 101 capillaries spread evenly across the central 4 inches of the die; air flowed through the entire 8 inches of the die width. Electrical heating was used to control the die temperature. Each polymer capillary had a diameter of 0.015 inches. Compressed air for blowing was routed first through an electric heater, and then through a four hose manifold, and finally to the die itself. Airflow was measured using Pitot sensors in the air lines, and airflow was controlled with a pressure regulator. Polymer pellets were melted and pressurized using a 19 mm (¾ inch) Brabender® extruder. The molten polymer was then fed to a gear pump that provided accurate polymer flow control. Polymer flow was measured by timed collection and weighing of fibers from the die. Fibers were collected on a solid collector that was placed 1 meter from the die face. The polymer used for the experiments was Fina Dypro® 3860 isotactic polypropylene with a nominal melt flow index of 100.

4.3.3 Operating Conditions

Line operating conditions were chosen to be representative of normal melt blowing. The polymer rates used were 1.13, 2.27, and 4.54 kg/hr (2.5, 5, and 10

lb/hr). Airflow rates used were 2500 and 3900 standard liters per minute (SLPM.) The die temperature was held at 300°C, while the air heater was set to 420°C. There were significant air temperature losses in the air lines leading to the die. The air heater temperature was set such that the air temperature at the die was approximately 300°C. The die configuration did not allow for direct measurements of the air temperature inside the die. However, measurements were taken of the air temperature of the jets at the die discharge; this temperature was 300°C.

4.3.4 Fiber Diameter Measurements

The laser scattering unit used for the ELD measurements in our experiments was the Powerscope Fibrsizr™. The unit consisted of a laser and a detector attached to a "U" frame and mounted on a movable stand; see Figure 4.5. Raw scattering data were transferred to a computer for analysis through a USB interface. Scattering data fitting and analysis were performed using included proprietary software. The instrument was located such that the detector head was as close as possible to the fiber stream without interfering with the process. The distance between the detector and the fibers is the working distance. This working distance (measured in the y direction in Figs. 4 and 5) must be kept as small as possible in order to improve the accuracy of the measurements. Since the distance between the detector and the emitter is about 1 meter, there are not any clearance problems associated with the emitter interfering with the fibers. At large working distances, the ELD technique will not resolve fibers of the smallest diameters. However, when only large diameter fibers are present in the sample, the working distance can be increased. At large distances from the die (large +z positions as shown in Figs. 4 and 5), the working

distance used was approximately 7.6 cm (3 inches). This working distance was small enough to resolve fiber diameters down to the instrument's lower limit of 1.5 microns. Due to physical clearance issues around the die, when the distance from the die (z position) was less than 8.9 cm (3.5 inches), the working distance was increased to approximately 20 cm (8 inches), which was just sufficient to clear the die; see the dotted lines in Fig. 5. With the increased working distance, measurements were taken as close as 0.64 cm (0.25 inches) from the die (z position); the die face itself interfered with closer measurements. Measurements taken at z = 8.9 cm (3.5 inches) from the die -- using both 7.6 and 20 cm working distances -- showed no difference due to using a larger working distance. The compensating factor is that, near the die, the fibers have larger diameters, and, hence, there is no need to measure smaller diameters.

Measurements were taken in two directions. First, the fiber diameter profile was measured by moving the ELD assembly in the z direction while keeping the assembly in the x=0 plane (i.e., the center of both the die face and the fiber curtain). These data provided both a measure of fiber attenuation and an approximation of fiber bundling. Second, measurements were taken across the width of the die (in the x direction) in order to determine the uniformity of the fiber diameter profiles across the width of the die.

4.4 Results and Discussion

4.4.1 Reproducibility Test

The first set of experiments was designed to evaluate the repeatability of the ELD (ensemble laser diffraction) method. Process flows were held constant at 2.27 kg/hr (5 lb/hr) of polymer and 2500 SLPM of air. Measurements were taken at increasing distances (z positions) from the die face and at the center (x=0 plane) of the fiber curtain. The mean diameter profiles determined by two typical replicate measurements for these process conditions are shown in Figure 4.6, and the standard deviations are shown in Figure 4.7. The standard deviation is an output of the ELD instrument. The standard deviation represents the width of the distribution of all fibers contained in the ELD measuring volume. As Figure 4.6 illustrates, the mean diameter data were highly reproducible from measurement to measurement, with typical differences being less than two microns. Figure 4.7 shows that the standard deviation is also reproducible from run to run (but not to the same degree as mean diameter). One important feature of Figure 4.6 is the apparent increase in mean diameter at distances (z positions) farther than 2.5 inches (6.3 cm) from the die. Since melt blown fibers are always expected to attenuate (have reduced diameter) or reach constant diameter for positions far from the die, this increase is attributed to bundling of fibers as they progress away from the die. Fiber bundling is a well-known occurrence in the melt blowing process (Yin et al., 1999). While the ELD technique does detect the bundling of fibers, the technique does not provide a quantitative measurement for the amount of bundling. In Figure 4.7 it appears that

the normalized standard deviation of the fiber distribution approaches an asymptote at approximately 10 inches (25 cm) from the die face. However, even through the normalized standard distribution is constant, the mean diameter is still increasing with further bundling as shown in Figure 4.6.

4.4.2 Variations across the Die Face

Measurements were taken across the width of the fiber curtain in order to gauge the uniformity of fiber distribution. End effects play an important role in the formation of melt blown products, and controlling the depth of the end effect is an important part of engineering a melt blowing process. Measurements across the width of the die (in the x direction) were taken at four different distances (z positions) from the die. These results are shown in Figures 4.8 and 4.9 for mean diameter and standard deviation, respectively. Observe that the fiber size is nearly constant across the die face. This suggests that the air end effects do not penetrate far enough from the ends of the air slots to affect the fiber attenuation. Thus, having two inches of fallow space (air but no polymer holes) at either end of the die was sufficient to prevent air jet end effects from affecting the fiber attenuation.

4.4.3 Spinline Profiles

To gauge the sensitivity of the ELD instrument to process changes, three measurements of the center fiber diameter profile (measurements along the z axis at x=0 and y=0) were taken at different polymer flow rates and air flow rates. The three tested polymer flow rates (2.5 lb/hr, 5 lb/hr, and 10 lb/hr) cover most of the operating range of this die at 300°C and 2500 SLPM airflow using Fina Dypro® 3860 isotactic

polypropylene. The mean diameter is shown in Figure 4.10, and the standard deviation is shown in Figure 4.11. The lower the polymer flowrate, the smaller the fiber diameter, as is expected. All three cases also show the mean diameter growth due to bundling.

Figure 4.11, the standard deviation graph, shows that, at large distances from the die face, the normalized standard deviation approaches an asymptotic value. The standard deviation becomes approximately 60 % of the measured mean fiber diameter, regardless of the polymer flow rate.

Figure 4.12 shows the mean diameter profiles for two different airflow rates. As is typical in melt blowing processes, the higher airflow rate produces finer fibers. Also, the distance at which attenuation is complete is shorter for higher airflow rates. As for the bundling effect at high z values, both airflow rates produce about the same percent increase in fiber size (versus the minimum fiber diameter at the flow rate in question).

4.5 Conclusions

Ensemble laser diffraction, or ELD, is a new technology for measuring fiber diameter distributions. This technique provides quick distribution measurements for both on-line and off-line operation. However, the ELD technique is based on a semi-empirical model for light diffraction though multiple fibers. This semi-empirical nature of this model may require calibration and verification for new applications. For the melt blowing application discussed in this paper, the ELD technique was calibrated against microscopic (off-line) measurements of fiber diameter and bundle

size. The chief advantages of ELD include (a) the large sampling volume compared to conventional LDV, (b) the nearly instantaneous response time, and (c) the ability to measure both moving and stationary fibers (i.e., on-line and off-line capability).

The mean fiber diameter showed a minimum along the spinline length. This minimum separates the attenuation region of the spinline from the bundling region. Also, the 8 inch die - with a center 4 inch zone for the fibers – had minimal variation of fiber attenuation rate across the width of the fiber curtain.

4.6 References

Bansal, V.; Shambaugh R.L. “On-Line Determination of Density and Crystallinity During Melt Spinning”, *Polym. Eng. Sci.*, **1996**, *36*(22), 2785-2798.

Black, D.L.; McQuay, M.Q.; Bonin, M.P. “Laser-based Techniques for Particle-size Measurement: A Review of Sizing Methods and Their Industrial Applications”, *Prog. Energy Combust. Sci.,* **1996**, *22*(3), 267-306.

Fandrey, C.W.; Naqwi, A.A. “Ensemble Diffraction for on- and off-line Sizing of Nonwoven Fibers”, International Nonwovens Technical Conference (INTC) 2003 Meeting, Renaissance Harbor Place Hotel, Baltimore, MD, September 15-18, 2003.

Marlow-Ferguson, R., ed. "Nonwoven Fabrics" in Encyclopedia of American Industries, 3rd ed., vol. 2, The Gale Group, Detroit, **2001**, 192.

Mie, G., “Beiträge zur Optik trüber Medien, speziell kolloidaler Metallösungen”, *Ann. Physik*, **1908,** *25*, 377-452.

Yin, H.; Yan, Z.; Bresee, R.R. “Experimental Study of the Melt Blowing Process”, *Int. Nonwovens J.*, **1999**, *8*(1), 60-65.

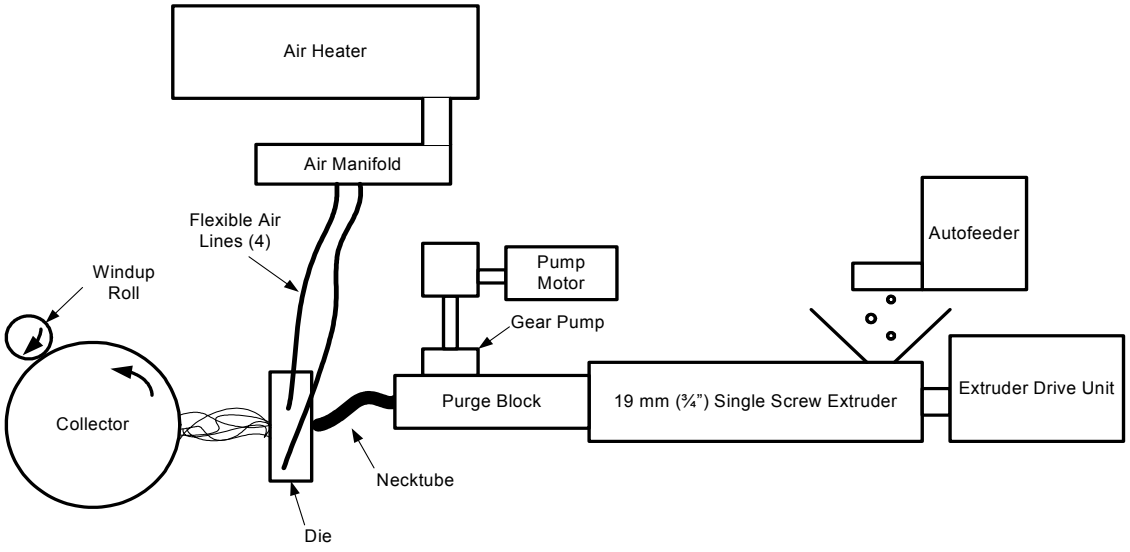

Figure 4.1. Diagram of the melt blowing process used in this work.

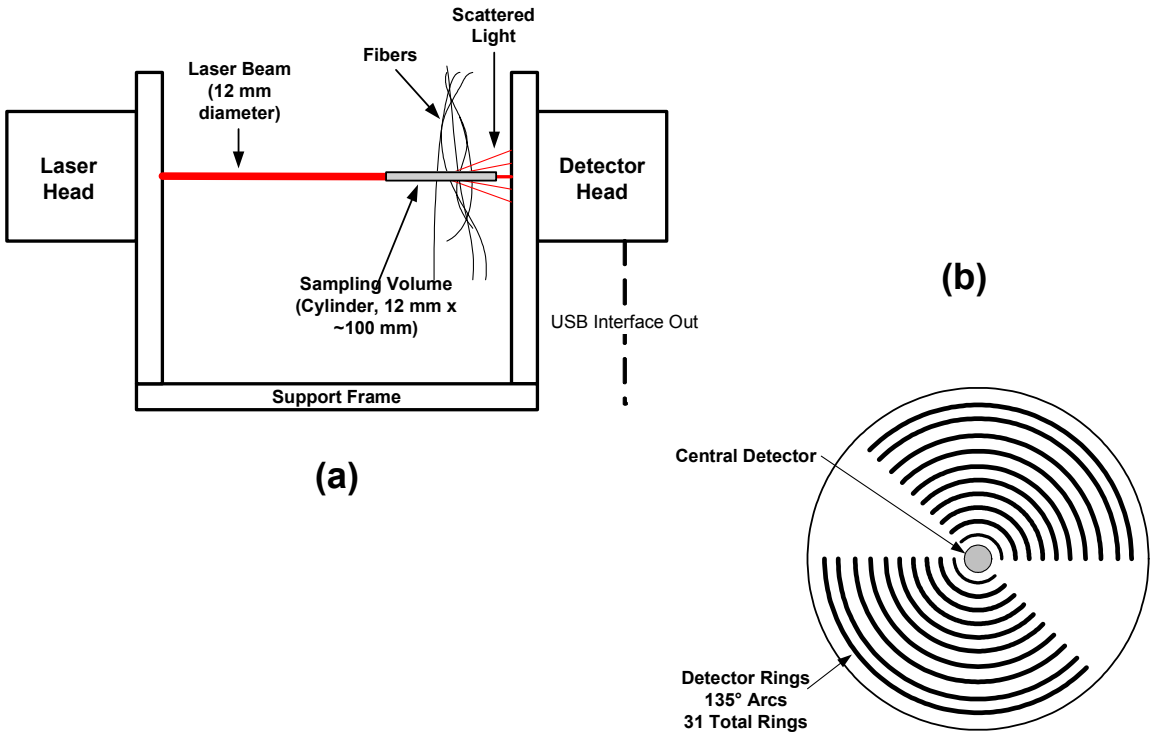

Figure 4.2. The FibrSizr™ unit: (a) overall diagram of the unit; (b) detector array.

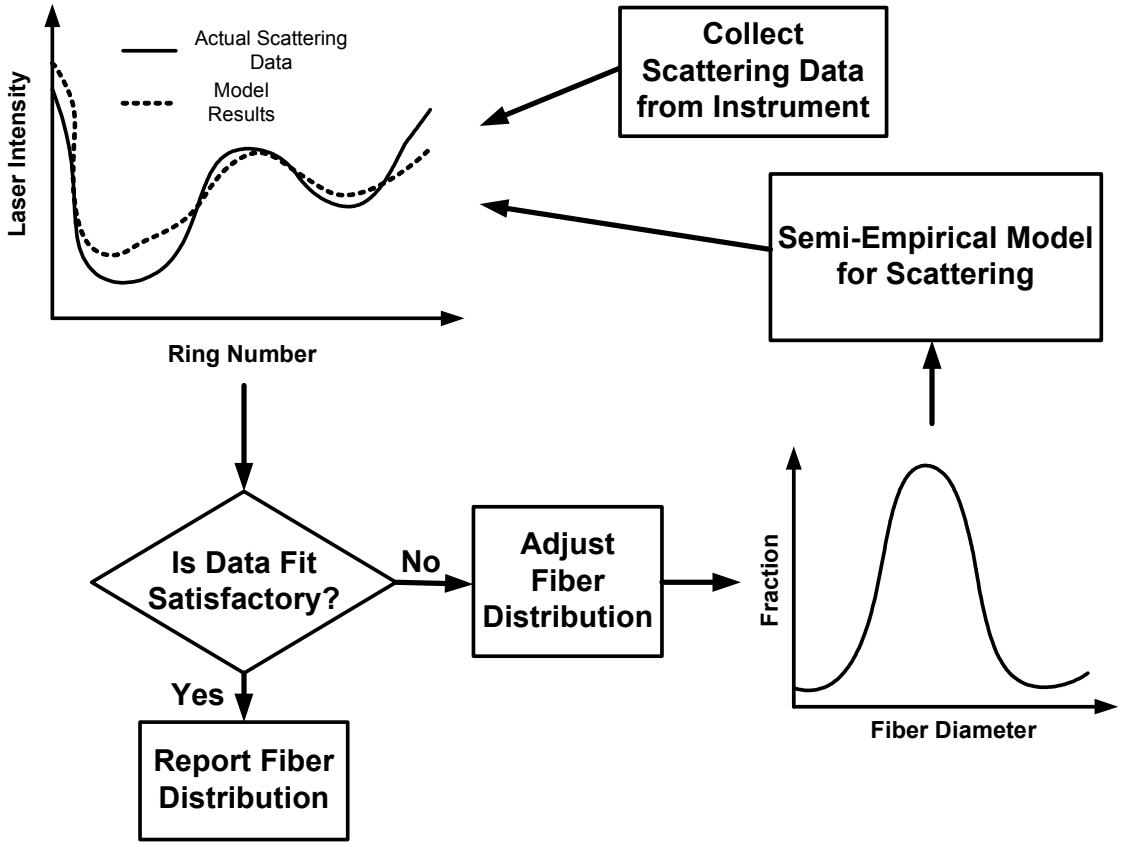

Figure 4.3. The calculation scheme used for determining fiber diameter distribution.

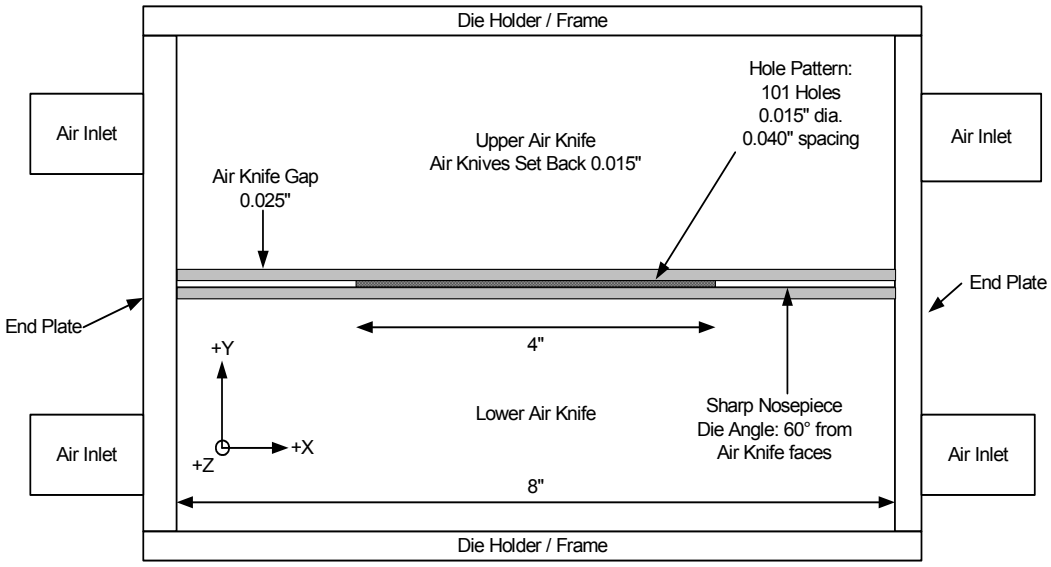

Figure 4.4. View of the face of the melt blowing die. The +z direction is perpendicular to the face, and the origin of the coordinate system is at the center of the die face.

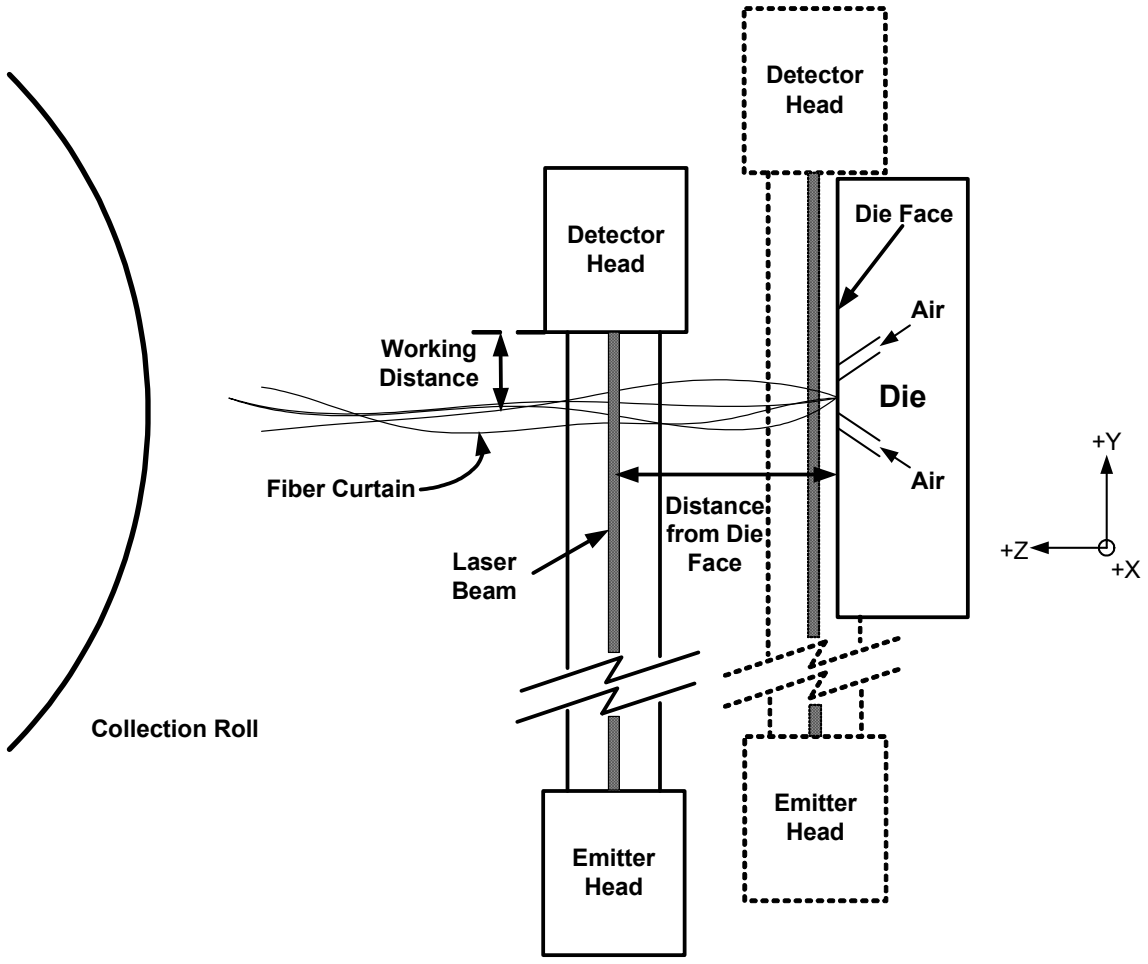

Figure 4.5. Orientation of FibrSizr™ unit relative to the melt blowing process. The distance between the emitter and collector is about 1 meter, and the working distance is optimally about 7.6 cm. However, near the die face, the working distance must be increased to about 20 cm because of clearance problems (the dotted lines show the FibrSizr™ unit in this situation).

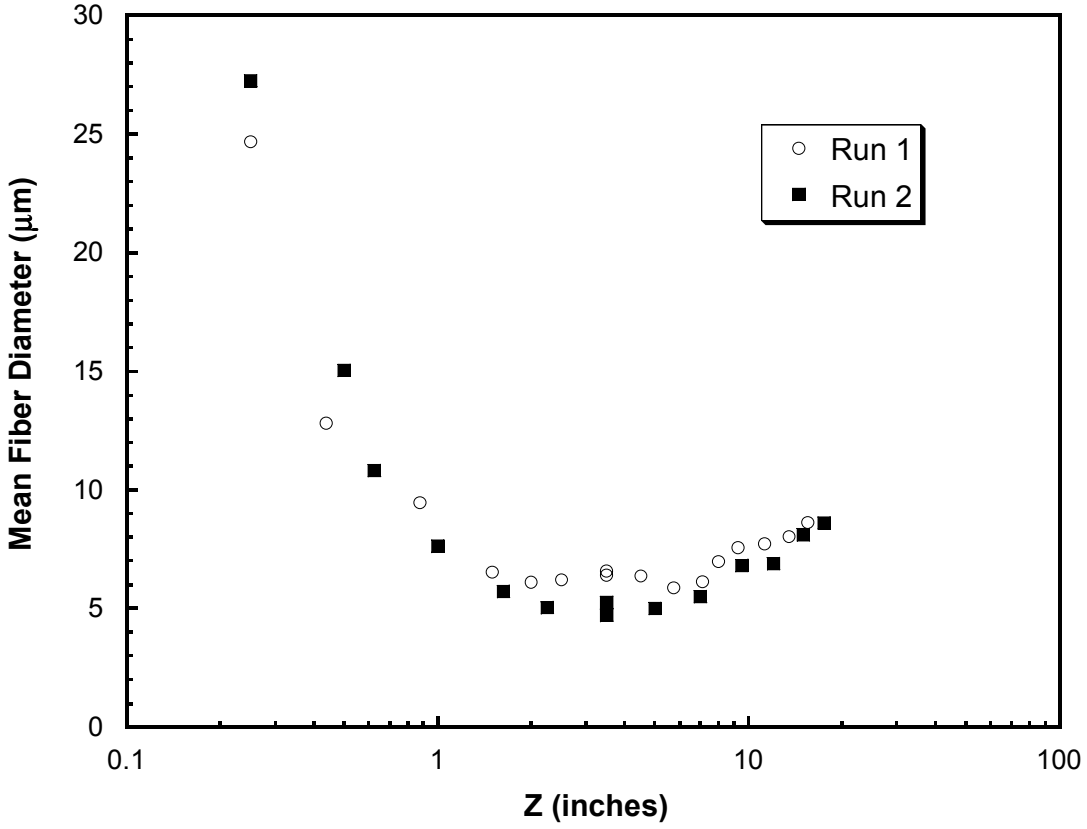

Figure 4.6. Mean diameter profiles obtained from two successive runs at 2.27 kg/hr (5 lb/hr) polymer flow, 300°C die temperature, and 2500 SLPM airflow.

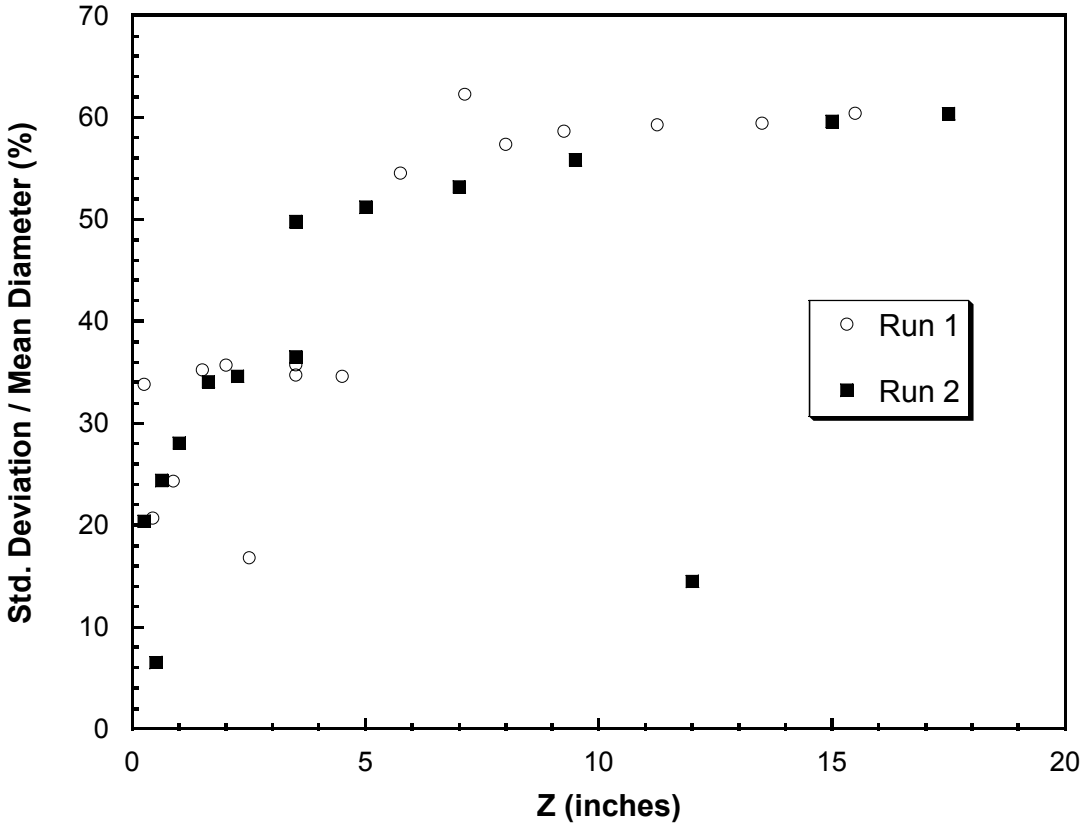

Figure 4.7. Profiles of diameter standard deviation obtained from two successive runs at 2.27 kg/hr (5 lb/hr) polymer flow, 300°C die temperature, and 2500 SLPM airflow.

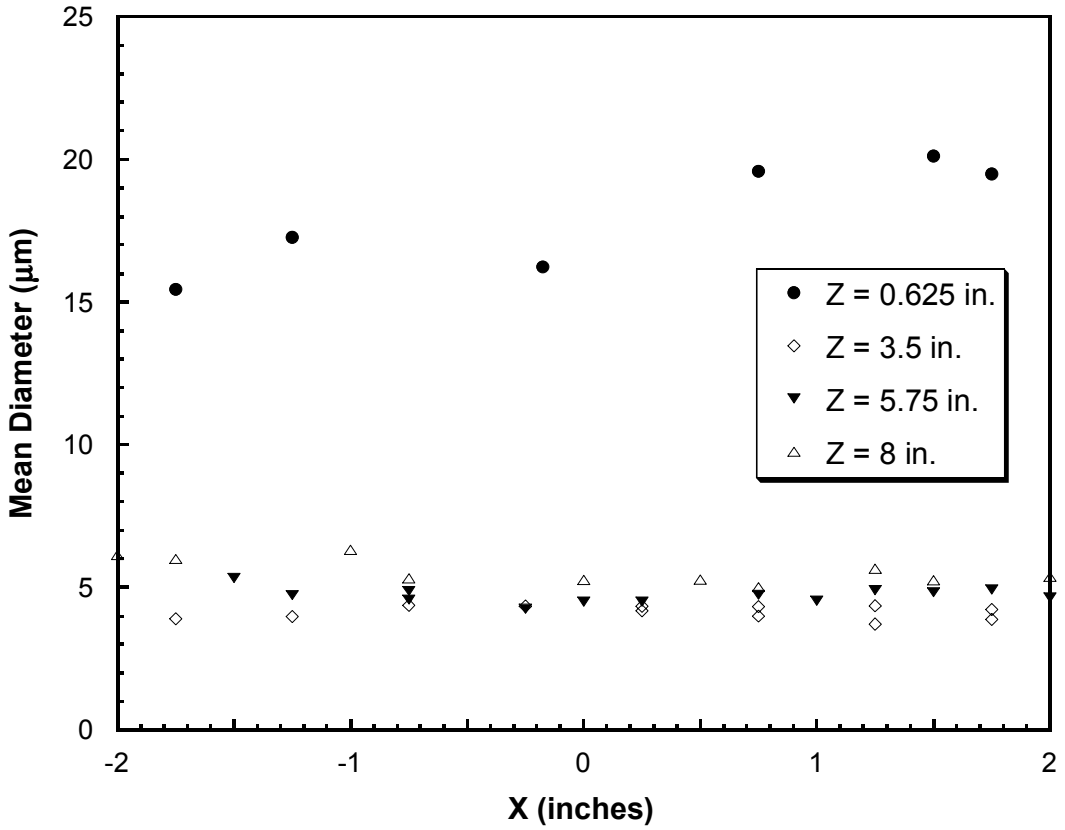

Figure 4.8. Variation of fiber diameter in the x direction for different z levels and y = 0. The run conditions were 2.27 kg/hr (5 lb/hr) polymer flow, 300°C die temperature, and 2500 SLPM airflow.

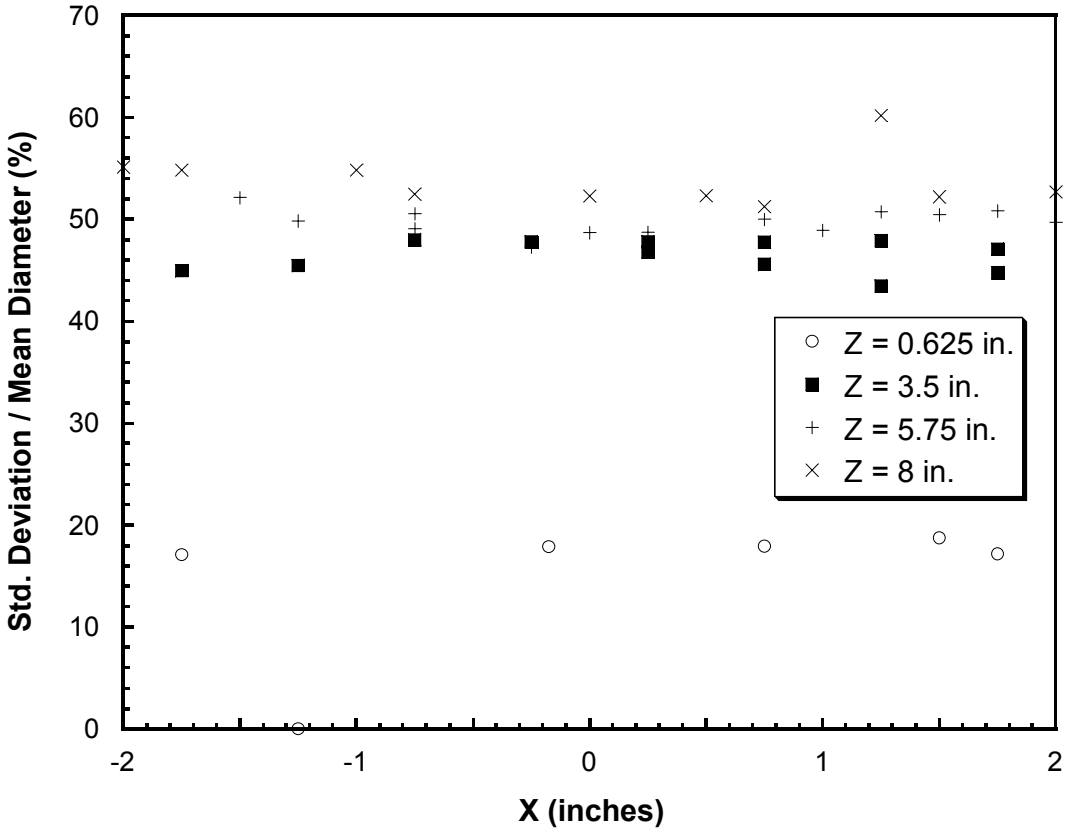

Figure 4.9. Diameter standard deviation variation in the x direction for different z levels and y = 0. The run conditions were 2.27 kg/hr (5 lb/hr) polymer flow, 300°C die temperature, and 2500 SLPM airflow.

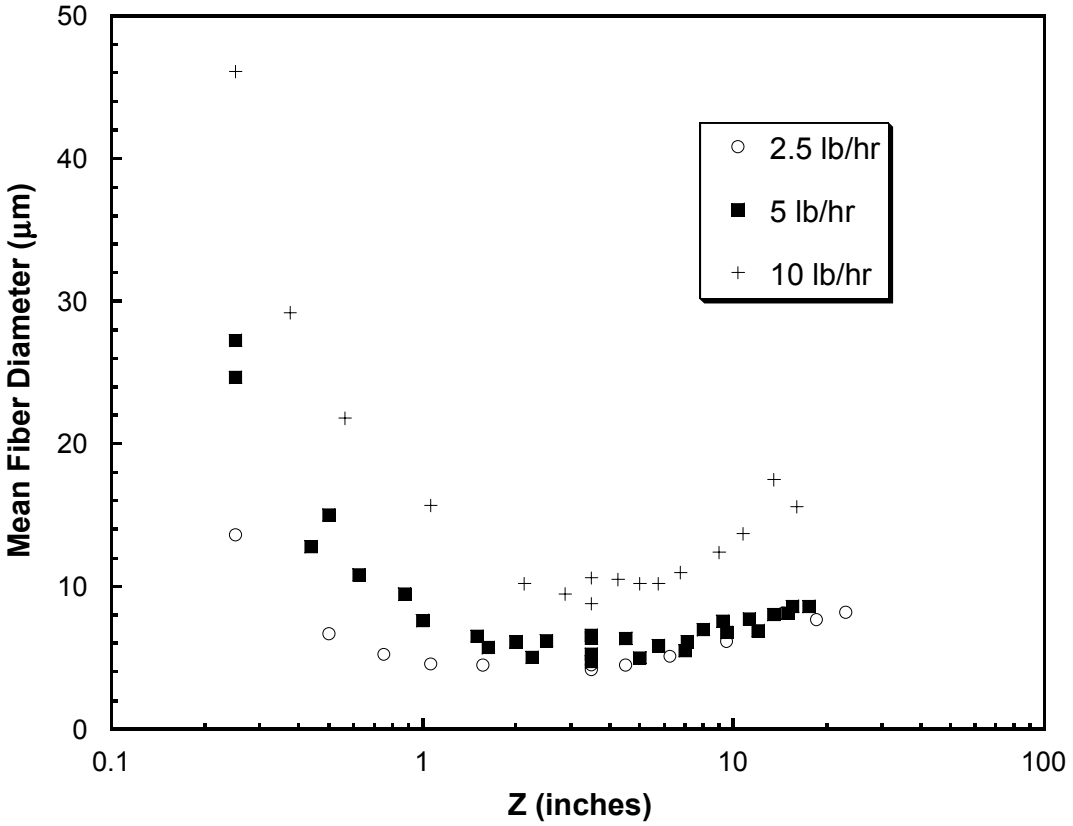

Figure 4.10. Mean diameter profiles as a function of z and for varying polymer flow rates. The die temperature was 300°C and the airflow was 2500 SLPM.

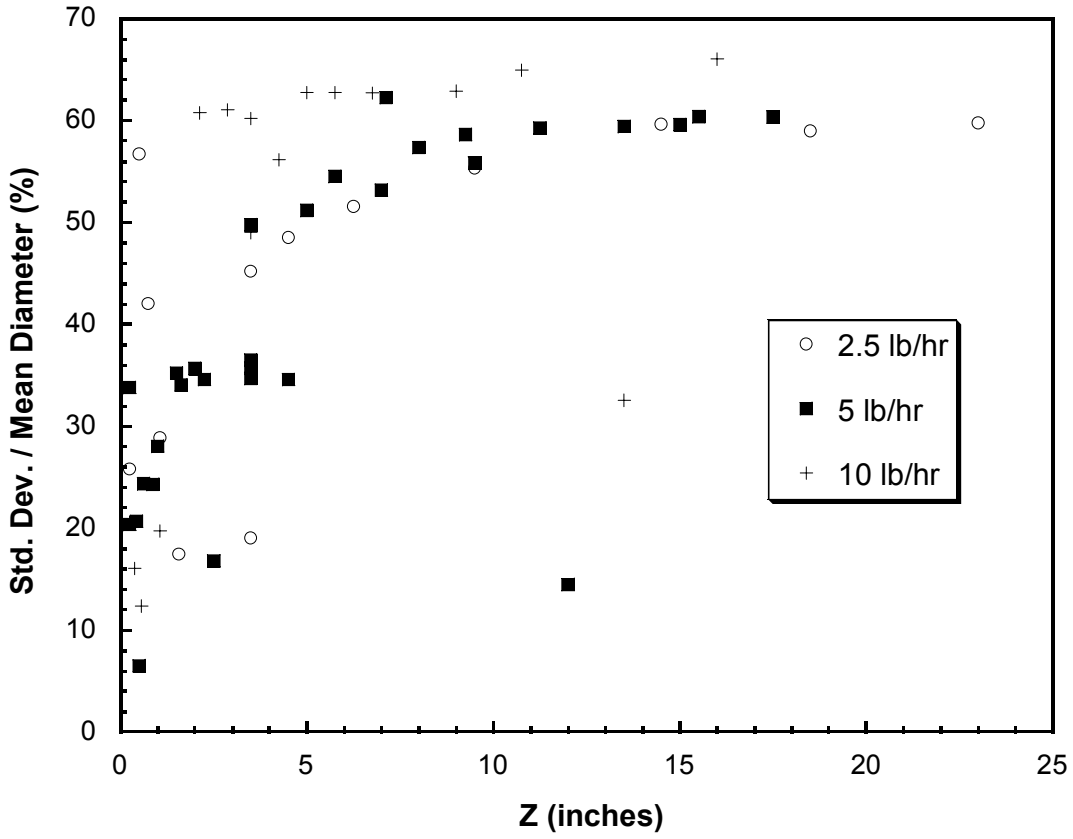

Figure 4.11. Diameter standard deviation variation as a function of z and for varying polymer flow rates. The die temperature was 300°C and the airflow was 2500 SLPM.

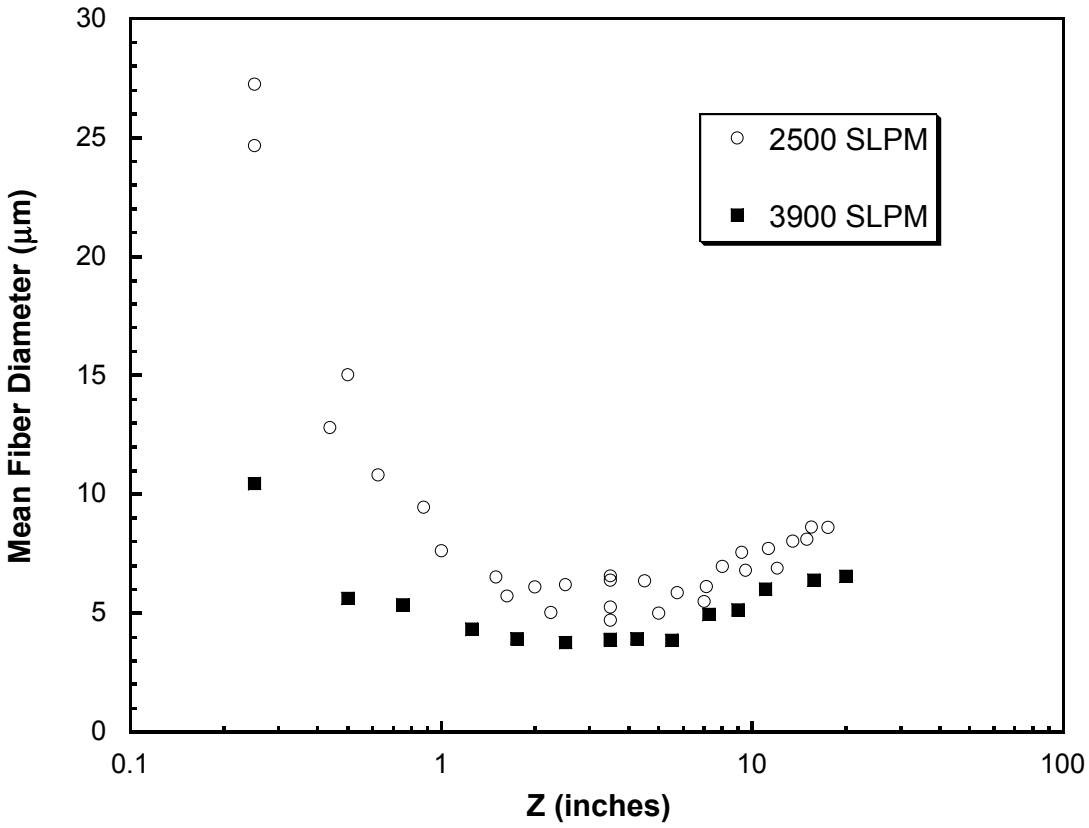

Figure 4.12. Mean diameter profiles for two different airflow rates. The polymer flow rate was 2.27 kg/hr (5 lb/hr) and the die temperature was 300°C.

Chapter 5

Air Velocity, Air Temperature, Fiber Vibration and Fiber Diameter Measurements on a Practical Melt Blowing Die

5.1 Abstract

Numerous measurements were taken on the operating behavior of a practical slot melt blowing die. The mean velocity and temperature of the melt blowing jet were measured, as well as the fiber diameter distributions of the webs produced.

Fiber vibration amplitudes during the melt blowing process were measured photographically. The light absorbance of the finished fiber mats were measured, and related to fiber diameter distribution and mat basis weight. Process conditions were varied across the operating range of the die to produce a variety of finished mats. It was found that the mean velocity and temperature decayed similarly to laboratory scale dies and rectangular jets. Fiber vibrations were found to be strongly dependent on operating temperature and air flow rate. The fiber light absorbance was found to be well correlated with the projected area of the fibers present in the mat.

5.2 Introduction

Melt blowing is a process for producing nonwoven fibers with small diameters, typically less than 30 microns. Fiber production involves using one or more jets of hot gas, usually air, to attenuate a molten polymer stream into a fine filament. The drawn fibers are typically collected on a moving collector for either direct use or further processing. Figure 5.1 illustrates a typical melt-blowing process. The end-uses for melt blown products include filtration media, absorbents, disposable wipes, and insulation (Batra et al., 1999).

There have been numerous studies on melt blowing dies, both on laboratory and commercial scales (see Chhabra and Shambaugh, 1996; Bresee and Ko, 2003; Yin et al., 1999; Yin et al., 2000). Some researchers have studied commercial scale dies, but the amount of data publicly available is limited especially with regard to air jet behavior. This work describes the flow and operating characteristics of a pilot scale melt blowing die. Measurements taken for this work include mean air velocity,

mean air temperature, fiber vibrations, final fiber diameter distribution, fiber web basis weight, and finished web light absorbance.

The dynamics of the melt blowing process are largely dependent on the air jets used. Previous studies of the flow fields in melt blowing jets have mostly focused on smaller, laboratory scale units (Uyttendaele and Shambaugh, 1989; Harpham and Shambaugh, 1996; Tate and Shambaugh, 1998.) The contribution of the present work is to provide data on a process much closer to a commercial scale than many previous publications.

5.3 Experimental Methodology

5.3.1 Process Description

The process studied in this work is a pilot-scale melt blowing line, utilizing a slot die of common design. The slot die concept is described in several patents (Keller et al., 1973; Harding et al., 1974; Buntin et al., 1974). The die used had a two-chamber air distributor design. The polymer used was Fina Dypro 3860 isotactic polypropylene. This is a commercial grade polypropylene suitable for nonwoven use, with a nominal melt flow index (MFI) of 100 g / 10 min. A ¾" single-screw extruder melted and fed the polymer to a heated positive displacement gear pump for metering and delivery to the melt blowing die. Air was supplied to the die from a central air heater, through insulated pipes and hoses, to the die. Even though the air lines were insulated, there were substantial heat losses between the heater and the die. Air heater temperature was adjusted to ensure that the initial air jet temperature matched the die temperature. All of the equipment was heated electrically. The heating in the

extruder involved multiple zone temperature controls, with the first zone of the screw extruder being water-cooled, in order to minimize polymer degradation.

The fibers were collected as a mat on a rotating smooth stainless steel drum, which wrapped the finished mats onto a floating take-up roll. Typically, collection of melt blown fibers is done on perforated or screened collectors. The choice of a smooth collector was made to facilitate future modeling work on process behavior near the collector.

5.3.2 Operating Conditions

Operating conditions were chosen to explore as much of the operable range of this die as possible. Preliminary runs were made to evaluate the operability limits of this particular die. It was found that if the air flow rate was too high, a large quantity of unbound fiber would be produced. This phenomenon is commonly referred to as 'fly', and has been studied previously by Bresee and Qureshi (2002). At low air flow rates, the polymer would not form a fibrous mat, but would melt into a nearly solid film on the collector. After preliminary studies, an experimental plan was devised that used 24 different operating conditions to study six operating variables (i.e., die temperature, polymer and air flow rate, air knife gap, distance from die to collector, and collector roll speed). Die temperature was set to 250°C, 300°C, and 350°C, with air temperature set at matching conditions. Polymer flow rates were 2.5 lb/hr, 5.0 lb/hr, and 7.5 lb/hr. The air flow rate was varied from 2000 to 5200 SLPM, with the air knife gaps set to 0.015" and 0.025". The die to collector distance was set to 8, 16, and 24 inches. Collector roll speed was set to 7.5 ft/min, 15 ft/min, and 30 ft/min. The variable combinations for the 24 experimental runs are listed in Table 5.1; each

run produced a different fiber mat for testing. Air velocity and temperature measurements were taken at operating conditions listed in Table 5.2.

5.3.3 Die Geometry

The die used was a conventional eight-inch wide stainless steel slot die. A detailed illustration of the die is shown in Figure 5.2. The overall length of the air slots was eight inches, with polymer orifices spaced evenly across the central four inches. The die had 101 polymer capillaries, each 0.015" in diameter and spaced with 0.040" between centers. The air knife gap was adjustable (0.015" and 0.025" were used for this study, as mentioned in the previous section). The die tip was sharp, meaning that the die nosepiece had a sharp edge. The angle between each of the air slots and the face of the die was 60^{o}. The air knives were set behind the tip of the nosepiece by 0.015". (Equivalently, the nosepiece was outset from the air knives by 0.015".)

A coordinate system was defined relative to the die face, as shown in Figure 5.2. The origin was defined to be the center of the die, at the tip of the nosepiece. The air slots, and the fiber curtain, were both oriented parallel to the ground. The X axis was parallel to the air slots along the die face. The Y axis was vertical, across the die face and away from the ground. The Z axis was perpendicular to the die face, again parallel to the ground. This system had the fiber curtain itself occupying the plane Y = 0.

Air was supplied to the die through four ¾" (nominal diameter) hoses, with two hoses feeding each air slot. The two air slots were not pneumatically connected to one another; the flow was adjusted to ensure equal flow through each slot.

5.3.4 Pitot Tube Measurements

Mean air velocity measurements were taken using a conventional Pitot tube that had an outer diameter of 0.7 mm and inner diameter of 0.4 mm, with a tapered tip. Dynamic pressure was read from the Pitot tube using an electronic pressure sensor, displaying pressure on an electronic display. The Pitot tube was attached to a three-dimensional manual traverse that could position the Pitot tube precisely within the flow field. The traverse had 0.001" resolution, more than sufficient to resolve the details of the flow under study. The measurement arrangement is pictured in Figure 5.3, showing the relative positions of the traverse, Pitot tube, and die. The Pitot tube was situated as far upstream of the traverse as possible. Fluctuations in the dynamic pressure readings were observed, due to the turbulence of the flow. The mean velocity was taken based on the average of the fluctuating velocity. Because of the limited response time of the small-diameter tube used in this study, quantitative turbulence measurements were not possible. Nondimensionalization was done based on the nominal velocity at the die face, which was calculated from the mass flow of air through the die and the ideal gas law. The definition of V_o is

$$V_o \equiv \frac{Q_{std} \cdot \rho_{std} \cdot R \cdot T_{Ambient}}{2 \cdot W \cdot L \cdot P_{std} \cdot MW_{Air}} \qquad (1)$$

where the values of the shown parameters are ρ_{std} = 1.289 kg/m^3 (ideal gas density at 0°C, 101325 Pa), P_{std} = 101325 Pa, R = 8.314 J/ (mol K), and MW_{Air} = 0.0289 kg / mol.

5.3.5 Air Temperature Measurements

Mean air temperature measurements were taken using a J-type thermocouple, 1 mm in diameter. The thermocouple was mounted to the same three-dimensional traverse used for the positioning of the Pitot tube. Temperature was read from the thermocouple using a commercial thermocouple reader. When taking readings, the thermocouple was held in place until the temperature reading was constant within 1° C.

Nondimenisionalization was accomplished using the excess temperature, θ, which is defined as the difference between the measured temperature and the ambient temperature

$$\theta \equiv T - T_{Ambient} \qquad (2)$$

The excess temperature of the die, θ_o, was defined similarly

$$\theta_o \equiv T_o - T_{Ambient} \qquad (3)$$

5.3.6 Fiber Vibration Measurements

Fiber vibration plays an important role in the formation of melt blown webs. The amplitude of the vibrations affects the bundling of fibers, their laydown patterns, as well as the actual attenuation of the fibers themselves. Quantifying the vibration of the fibers is a technical challenge, one amplified by the operating conditions of typical melt blowing processes. Chhabra and Shambaugh (1996) studied the behavior of a laboratory melt blowing process using LDV and photographic techniques. They were able to measure both the amplitude and the frequency of the vibrations present in the laboratory process. A photographic technique similar to that used in Chhabra

and Shambaugh was used in the present work to investigate the amplitude of fiber vibrations on a die operating at industrial conditions. The increased speed of the process (approximately ten times of that in Chhabra and Shambaugh's work) poses increased challenge. At lower operating speeds this photographic technique can also be used to measure the diameter of the fibers during the melt blowing process. Yin et al. (1999) also studied online fiber diameters using pulse laser illuminated photography, and still encountered difficulty measuring online fiber diameter. The increased speeds of this work make such diameter determinations impossible, however the vibrations can still be measured.

Fiber vibration was measured photographically, using a commercial 35 mm camera and film. The camera used was a Nikon™ N90s camera, equipped with a Nikkor 105 mm macro lens, using Kodak ISO 400 color film. Exposure time was set at $1/60^{th}$ of a second. Lighting was done using two sources, ambient lighting and a stroboscope. Ambient lighting was fluorescent bulbs, as is common in the laboratory environment. The stroboscope used was a General Radio model 1546 stroboscope. The stroboscope frequency was set at 4500 flashes/minute, resulting in 1.25 average flashes per exposure. Flash duration was approximately 1.2 μs. The macro lens was set to a 5:1 reduction, and focus was achieved by moving the camera to the correct distance. With the lens reduction, the resulting 4"x6" prints were nearly life size. Precise length calibration was achieved using photographs containing rulers with known gradations.

Photographs resulting from this technique show a clearly defined fiber wedge, as shown in Figure 5.4. The width of the fiber wedge was measured as a function of

distance from the die face. Multiple exposures of each distance and operating conditions allow for an average cone width to be determined. This wedge width is a measure of the vibration amplitude of the fibers during the melt spinning process.

5.3.7 Fiber Diameter Measurements

Fiber diameter distribution was measured using optical microscopy. An Olympus BX-41 microscope with digital image capture was used. Images were taken using two different magnifications and lighting conditions. First, a 10x objective lens and transmitted light was used to image the larger fibers. Second, a 50x objective lens and reflected light was used to provide images of smaller diameter fibers, typically five microns and less. Each magnification and lighting was calibrated using a micrometer slide with ten micron gradations. The digital images taken had a resolution of 1.076 μm/pixel and 5.405 μm/pixel for the 10x and 50x objectives, respectively. Fiber diameter was measured by measuring the number of pixels in the width of the fiber using a commonly available image manipulation package. For each of the fiber samples between 31 and 59 individual fibers were measured. These relatively large measurement counts allowed for an estimate of fiber diameter distribution as well as mean diameter for each fiber sample. Fiber diameter distribution was characterized by the mean fiber diameter and the distribution standard deviation (DSD), which provides a measure of the width of the fiber diameter distribution. It is well known that melt blown fibers exhibit a statistical diameter distribution; diameter distribution is important to finished web properties, such as pressure drop.

5.3.8 Light Absorbance Measurements

The absorbance of the collected fiber mats was measured using the technique described by de Rovere and Shambaugh (2001). This technique uses two tubesconnected end to end, between which the fiber mat is placed (see Figure 5.5). In one end a controlled amount of light is projected, while on the other end a light meter measures the intensity of the transmitted light, with the fiber sample in between. For this work, the tubes were made of cardboard, each 10.0 cm long with a 5.0 cm inner diameter. The light was provided by a Nikon MKII fiber optic light, and was measured using a Lutron LX-101 lux meter. Figure 5.5 illustrates this measurement technique. Along with the sample, a sheet of transparent polypropylene film was also placed between the two tubes, to act as a support for the fiber webs. Measurements were taken at the center of the web in order to avoid edge effects.

When taking measurements, an initial measurement was taken with no sample, only the transparent support sheet. The light was then adjusted until the initial illumination (I_o) was 8,000 lux, to within 50 lux. After loading the fiber mat into the device, the intensity of light transmitted through the sample (I) was measured. After measurement, the measured 5 cm diameter circle was cut from the web, and weighed to an accuracy of +/- 0.1 mg. For each fiber mat, measurements were taken on five different areas of the mat.

Calculations were made based on the principles of light transmission, with absorbance defined as $A = - \log_{10}(I / I_o)$. The absorbance of each fiber mat was reported, as well as the standard deviations of both the absorbance and the basis weight. These results are listed in Table 5.2.

5.4 Results

5.4.1 Pitot Tube and Thermocouple Measurements

Mean velocity decay measurements were taken by sweeping the Pitot tube along three lines perpendicular to the die face (and parallel to the Z axis). The first line originated at X = 0 and Y = 0 (the center of the die face), and the direction of the sweep was away from the die face. The origins of the second and the third lines were at X = 2 inches and Y = 0, and X = 4 inches and Y = 0, respectively. Readings were taken with 2600 SLPM of air flow and die temperatures of 300°C and 350°C. Figure 5.6 shows the nondimensionalized velocity profiles for the three different sweep lines. Distance from the die is nondimensionalized using Z(h), which is a combination of the initial jet width and the ratio of the jet air density over the density of ambient air. This form for distance is based on the one suggested by Obot et al., (1986) for round nozzles. Notice that in the region of well developed air flow, Z(h) > 10, the velocity profiles are in good agreement. However in the very near field, Z(h) < 3, there are some differences in the flow profile. Fitting a power law expression to the combined data provides the following single correlation, which is valid for Z(h) > 5:

$$\frac{V}{V_o} = 1.864 \cdot Z(h)^{-0.6321} \qquad (4)$$

This power law form for the velocity decay is similar to that for other cases of turbulent jets. It is important to note that the decay exponent (-0.6321) has a greater absolute value than the exponent of -0.5 predicted for a single plane jet (Schlichting,

1979). The decay constant is also greater in magnitude than the –0.532 measured by Tate and Shambaugh (1998) for a laboratory single hole slot die at low velocity.

Temperature profiles are shown in Figure 5.7 for the same three sweeps. While the profiles for the center and edge of the die show excellent agreement, the profile with X = 2 inches shows a significant difference. Throughout the middle development of the jet, the X = 2 inches profile shows a significantly cooler temperature profile. Taking all the temperature data, including at X = 2 inches, a power law equation does provide a good fit, despite the cooler profile at X =2 inches. Equation 5 shows the least squares power law that correlates the dimensionless excess temperature to position; this equation is valid for all Z(h) > 5.

$$\frac{\theta}{\theta_o} = 1.3491 \cdot Z(h)^{-0.4703} \qquad (5)$$

It is important to note that while the velocity decay profiles at X = 0, 2, and 4 inches are the same; the mean velocity across the face (in the X direction) is <u>not</u> constant. Figure 5.8 shows the mean air velocity and the mean air temperature below the die face for a typical sweep in the X direction keeping Y and Z constant. Note the two peaks in velocity and temperature at approximately X = +/- 3.5 inches. These end velocity peaks are a well known occurrence in three-dimensional rectangular jets (Trentacoste and Sforza, 1967). This same dual peak behavior has also been observed in melt blowing slot jets (Harpham and Shambaugh, 1996). Aside from the two end peaks, the velocity profile in the X direction is relatively flat; the air jet does not appear to spread in the X direction. The data below a heated die (300°C and 350°C) showed that the maximums of both the V and θ end peaks were, on average,

1.26 and 1.27 times the average value of those quantities for the middle four inches of the die, respectively. Even though the width of these peaks did vary from 0.5 to 1.0 inches, no clear trend was observed with increasing Z values. Peak positions also varied from X = +/- 3.25 to 3.75 inches, but as with peak width, no trend was observed with increasing Z values.

5.4.2 Fiber Vibration Measurements

The effect of operating parameters on the fiber vibration amplitude was explored photographically. For each experiment, the width of the fiber cone was plotted as a function of the distance from the die. A linear equation was fitted to each run condition. The fitted line was forced to pass through the origin of the axes (i.e., to have a zero intercept) and the slope of the line was defined as the spreading coefficient. Due to the chaotic nature of the process, there was some data scattering for each measurement, but even with this experimental uncertainty, some qualitative trends become apparent.

The die temperature has a dramatic effect on the fiber vibrations. The spreading coefficient of the cone increases with die temperature, as shown in Figure 5.9. This spreading rate increases from 0.100 at 250°C to 0.327 at 350°. An increasing trend of this type was predicted by the modeling work of Marla and Shambaugh (2003). Air velocity has a strong impact on the vibration of the fiber during melt blowing. It is expected that as the blowing air velocity increases, the increased turbulence will increase the fiber vibration amplitude. Marla and Shambaugh (2003) also reached this conclusion through modeling work. This trend

is observed in Figure 5.10. While there is much scatter in the data, the trend is present; the mean vibration amplitude increases with increasing air flow rate.

The effect of polymer flow rate and the effect of die to collector distance (DCD) on fiber vibration were also explored. It was found that there was no statistically significant effect of either operating variable on the spreading rate of the fiber wedge. The conclusion that DCD has little effect on fiber vibration is not a surprising result, as Yin et al., (1999) also experimentally found that fiber velocity and diameter were not significantly affected near the die by the presence of a collector.

5.4.3 Fiber Diameter

Fiber diameter was measured for each of the 24 fiber mats. The mean diameter, N, and the diameter standard deviation (DSD) of each fiber mat is reported in Table 5.2. The mean diameters varied from 3.5 μm to 13.9 μm, and the DSD varied from 1.66 to 5.25 μm.

Some qualitative trends can be obtained from the data. As air flow increased, fiber diameter decreased. Polymer flow rate and mean diameter are directly related. . Figure 5.11 shows the DSD as a function of mean diameter, showing that DSD generally increases with mean diameter. Figure 5.12, however, shows that the DSD normalized with the mean diameter actually decreases with increasing mean fiber diameter. As the air flow to polymer flow ratio increases, the fiber diameters reduce, and, thus, the air turbulence would be more likely to introduce some randomization in

the fiber attenuation process. This randomization leads to the increase in normalized DSD with decreasing diameter.

5.4.4 Fiber Mat Light Absorption Measurements

Mat light absorbance was measured for all the fiber samples collected. A graph of absorbance versus basis weight is shown in Figure 5.13. It is apparent from the figure that the basis weight is not the only factor in the light absorption properties of the webs. However, a general trend of increased absorbance with increasing basis weight is observed. It is important to note, that while this data seems scattered, the actual measurements have a small standard deviation. For each fiber sample the standard deviations observed for the light absorbance is, with only one exception, less than 5% of the mean value. This error in light absorbance is actually smaller than the observed standard deviations in the basis weight measurements, which varied from 3% to 13% of the mean basis weight.

de Rovere and Shambaugh (2001) correlated the absorbance data of melt spun fiber samples based on the projected area of the fibers present in the mat. They found that one correlation could adequately describe the behavior of melt spun polypropylene fibers. However, their work did not use non-dimensionalized variables. The present work uses a non-dimensional projected area. The projected area in a given mat is defined as

$$PA = \frac{4 \cdot BW}{\pi \cdot D_{mean} \cdot \rho_p} \qquad (6)$$

This formulation eliminates all units so that mats of various sizes can be compared directly. Applying this technique to the present samples, a single model curve of the following form can fit the data well:

$$A = k \cdot \frac{PA}{PA + k'} \qquad (7)$$

This model is based on the Beer-Lambert law. Least squares fitting of the current data to this model produced constants k = 1.6896 and k' = 20.0810. These constants are different than those proposed by de Rovere and Shambaugh (k = 1.156 and k' = 5.0481). This difference was expected, as the fiber diameters for the melt blown webs are approximately an order of magnitude smaller than the melt spun fibers studied by de Rovere and Shambaugh. Figure 5.14 shows the current data, as well as the model described in Equation 7 and the one described in de Rovere and Shambaugh. The current model fits the data better than that of de Rovere and Shambaugh. It is important to note that the highest projected area measured by de Rovere and Shambaugh was only 17.5 while the present data extend to three times that value.

As shown in the work of de Rovere and Shambaugh (2001) the actual fiber diameters are crucial to the light absorption properties of nonwoven mats. The mats obtained from the melt blowing process have a statistical distribution of fiber diameters. In order to quantify the effect of diameter distribution, the absorbance of the mats must be related to the diameter of the fibers. In order to simplify the calculations, it was decided to discretize the diameter distribution in 1 μm increments. The resulting histogram was used to generate a more accurate projected area for each

mat. The contribution to projected area of each fiber diameter range was summed to find the second order projected area estimate, as shown in Equation 8. Due to the polydispersity of the fiber diameters, PA_2 is larger than PA.

$$PA_2 = \sum_i \frac{4 \cdot BW}{\pi \cdot D_i \cdot \rho_p} \cdot \chi_i \qquad (8)$$

This technique allows for the distribution of fiber diameters to be accounted for in estimating the absorbance of a fiber mat. The actual absorbance still follows the form given in Equation 7. Figure 5.15 compares the absorbance vs. PA curves using both PA and PA_2. The constants for Equation 7 using PA_2 are k = 1.7537 and k' = 23.5989, only slightly different from the values obtained using only PA. The correlation of covariance (R^2) of the two models is 0.91074 when using PA, and 0.92663 when using PA_2. While there is a slight improvement in the fit when using PA_2, this improvement is small. It is safe to conclude that while polydispersity may have some effect on the light absorbance of melt blown fibers, using only the mean diameter provides accurate results. Other effects that were not studied in this work (i.e. bundling of fibers and shot formation) are contributing more to the light absorption properties than the polydispersity of fiber diameters.

5.5 Conclusions

A detailed study of the operating behavior of a pilot scale melt blowing die was done. Both the aerodynamics of the die and the finished mat properties were examined.

It was found that the aerodynamics of this larger die are similar to those of smaller dies studied previously. The air velocity and temperature behavior follows the trends observed with both rectangular jets and smaller melt blowing dies. Velocity and temperature end effects were found to penetrate approximately 1 inch from the ends of the air slots. The end effects of the air slot resulted into higher mean velocities and temperatures closer to the end of the slots than at the middle of the jet.

Fiber vibration amplitudes were studied photographically. It was found that there is a strong correlation between vibration amplitude and die temperature. A weaker, but expected correlation was found for air velocity dependence.

Fiber diameter was found to respond as expected to changes in operating conditions. It was found that the normalized distribution standard deviation (DSD) increased with decreasing diameter.

Fiber light absorbance was measured, and it was found that the amount of absorbance was strongly dependent on the basis weight and mean diameter. Using projected area calculations it was found that the distribution of fiber diameters has little effect on the light absorbance properties of melt blown polypropylene mats.

5.6 Nomenclature

Roman Characters

A = Light absorbance

BW = Basis weight of fibers (g/m^2)

D_{mean} = diameter of fibers

DSD = Standard deviation of fiber diameter distribution (μm)

I = Transmitted light intensity (lux)

I_o = Initial light intensity (lux)

L = Air knife gap (mm)

MW_{Air} = Molecular weight of Air (kg / mol)

N = Number of measurements taken of diameter

PA = Projected area of fibers in mat based on mean diameter (m^2 / m^2)

PA_2 = Projected area of fibers in mat based on fiber diameter distribution (m^2 / m^2)

P_{Std} = Ambient pressure (Pa)

Q_{Std} = Air flow through the die (Standard L / min)

R = Universal gas constant (J / mol K)

T = Temperature (°C)

$T_{Ambient}$ = Ambient temperature (°C)

T_o = Die temperature (°C)

V = Mean velocity in the Z direction (m/s)

V_o = Nominal mean initial jet velocity (m/s)

W = Width of slot jets (cm)

X = Distance along slots, away from center of die

Y = Distance above nosepiece

Z = Distance away from die face

Z(h) = Nondimensional distance from die face = $(Z\ \rho_0^{0.5}) / (h\ \rho_\infty^{0.5})$

h = Combined jet initial width, two times air knife gap plus the nosepiece width

k = Empirical constant for light absorbance model

k' = Empirical constant for light absorbance model

t = Light transmittance

Greek Characters

χ_i = Fraction of fibers with diameters between i and i-1 microns

θ = Excess temperature (°C)

θ_o= Die excess temperature (°C)

ρ_{std} = Air density at STP (kg / m^3)

ρ_p = Polymer density (kg / m^3)

ρ = Air density at die temperature (kg /m^3)

ρ_∞ = Air density at ambient conditions (kg/m^3)

5.7 References

Batra, S.K.; Cook, F.L.; Goswami, B.; Vaughn, E.; Wadsworth, L.C.; Walsh, W.K., eds. The Nonwoven Fabrics Handbook. INDA, **1999**.

Bresee, R.; Ko, W. "Fiber Formation During Melt Blowing", *Int. Nonwovens J.*, **2003**, 12(2), 21-28.

Bresee, R.; Qureshi, U. "Fiber Motion Near The Collector During Melt Blowing: Part 2 – Fly Formation", *Int. Nonwovens J.*, **2002**, 11(3), 21-27.

Buntin, R.R.; Keller, J.P.; Harding, J.W. "Nonwoven mats by melt blowing." U.S. Patent 3,849,241, **1974**.

Chhabra, R.; Shambaugh, R.L. "Experimental Measurements of Fiber Threadline Vibrations in the Melt Blowing Process". *Ind. Eng. Chem. Res.*, **1996**, *35*, 4366-4374.

de Rovere, A.; Shambaugh, R.L. "Melt Spun Hollow Fibers for use in Nonwoven Structures", *Ind. Eng. Chem. Res.*, **2001**, *40*, 176-187.

Harding, J.W.; Keller, J.P.; Buntin, R.R. "Melt-blowing die for producing nonwoven mats.", U.S. Patent 3,825,527, **1974**

Harpham, A.; Shambaugh, R.L. "Flow Field of Practical Dual Rectangular Jets", *Ind. Eng. Chem. Res.*, **1996**, *35*, 3776-3781.

Keller, J.P.; Prentice, J.S; Harding, J.W. "Process for producing melt-blown nonwoven synthetic polymer mat having high tear resistance.", U.S. Patent 3,755,527, **1973**.

Marla, Vishnu T.; Shambaugh, R.L. "Three-Dimensional Model of the Melt-Blowing Process", *Ind. Eng. Chem. Res*. **2003**, *32*, 6993-7005.

Obot, N.T.; Graska, M.L.; Gandhi, F. "Velocity and Temperature Fields in Turbulent Jets Issuing from Sharp-Edged Inlet Round Nozzles", *Ind. Eng. Chem. Fundam.*, **1986**, *25*, 425.

Schlichting, H. Boundary Layer Theory, 7th Ed., McGraw Hill, **1979,** pg. 734.

Tate, B.D.; Shambaugh, R.L. "Modified Dual Rectangular Jets for Fiber Production", *Ind. Eng. Chem. Res.*, **1998**, *37*, 3772-3779.

Trentacoste, N.; Sforza, P. “Further Experimental Results for Three-Dimensional Free Jets”, *AIAA J.*, **1967**, *5*(5), 885-891.

Uyttendaele, M.A.J.; Shambaugh, R.L. “The Flow Field of Annular Jets at Moderate Reynolds Numbers”, *Ind. Eng. Chem. Res.* **1989**, *28*, 1735-1740.

Yin, H; Yan, Z; Bresee, R. “Experimental Study of the Meltblowing Process”, *Int. Nonwovens J.*, **1999**, *8*(1), 121-138.

Yin, H.; Yan, Z.; Ko, W.; Bresee, R. “Fundamental Description of the Melt Blowing Process”, *Int. Nonwovens J.*, **2000**, *9*(4), 25-28.

Sample	To	Air Flow Rate	Polymer Flow Rate	Air Knife Gap	DCD	Collector Speed	Vo
	°C	*SLPM*	*lb/hr*	*inches*	*inches*	*ft / min*	*m/s*
1	300	3000	2.5	0.025	16	15.0	406.5
2	300	3000	5.0	0.025	16	15.0	406.5
3	300	3000	7.5	0.025	16	15.0	406.5
4	300	2191	5.0	0.025	16	15.0	296.9
5	300	4640	5.0	0.025	16	15.0	628.8
6	300	5910	5.0	0.025	16	15.0	800.9
7	300	3023	2.5	0.015	16	15.0	682.8
8	300	3023	5.0	0.015	16	15.0	682.8
9	300	3023	7.5	0.015	16	15.0	682.8
10	300	1968	5.0	0.015	16	15.0	444.5
11	300	4188	5.0	0.015	16	15.0	945.9
12	300	5131	5.0	0.015	16	15.0	1159.0
13	300	2927	5.0	0.015	8	15.0	661.1
14	300	2927	5.0	0.015	24	15.0	661.1
15	300	2927	5.0	0.015	16	7.5	661.1
16	300	2927	5.0	0.015	16	30.0	661.1
17	350	2823	5.0	0.015	16	15.0	693.2
18	250	3023	5.0	0.015	16	15.0	623.2
19	250	2604	5.0	0.025	16	15.0	322.1
20	300	2695	5.0	0.025	16	7.5	365.2
21	300	2695	5.0	0.025	16	30.0	365.2
22	300	2695	5.0	0.025	8	15.0	365.2
23	300	2695	5.0	0.025	24	15.0	365.2
24	350	2150	5.0	0.025	16	15.0	316.8

Table 5.1. Operating Conditions.

Sample	Mean D	DSD	DSD / Mean	Absorbance	Basis Weight
	μm	μm	%		g/m2
1	3.495	1.687	48.27	0.9758	66.16
2	7.611	3.734	49.06	0.8102	90.25
3	11.004	3.563	32.38	0.6434	132.36
4	12.145	5.004	41.20	0.5840	81.84
5	5.807	3.577	61.61	0.9848	101.99
6	3.850	1.977	51.36	1.0971	106.04
7	4.686	3.036	64.79	0.9798	66.52
8	6.634	2.644	39.85	0.8551	101.86
9	10.492	4.505	42.94	0.7683	151.20
10	12.136	5.245	43.22	0.6045	94.55
11	3.877	1.710	44.12	1.0965	117.80
12	4.176	1.657	39.69	1.1985	124.94
13	8.480	4.238	49.97	0.7038	79.30
14	6.329	2.233	35.28	0.8706	116.03
15	8.314	3.443	41.41	1.0300	208.79
16	7.548	4.073	53.96	0.5776	49.63
17	3.463	2.261	65.29	1.3255	124.64
18	11.659	5.039	43.22	0.5161	90.03
19	13.923	4.266	30.64	0.4398	81.09
20	9.808	3.644	37.15	0.9146	182.46
21	8.539	3.907	45.75	0.5167	44.15
22	8.847	3.928	44.39	0.7336	71.09
23	9.806	2.826	28.82	0.7373	112.14
24	4.636	2.581	55.67	1.0170	50.56

Table 5.2. Mean Diameter, DSD, Absorbance, and Basis Weight for each fiber sample.

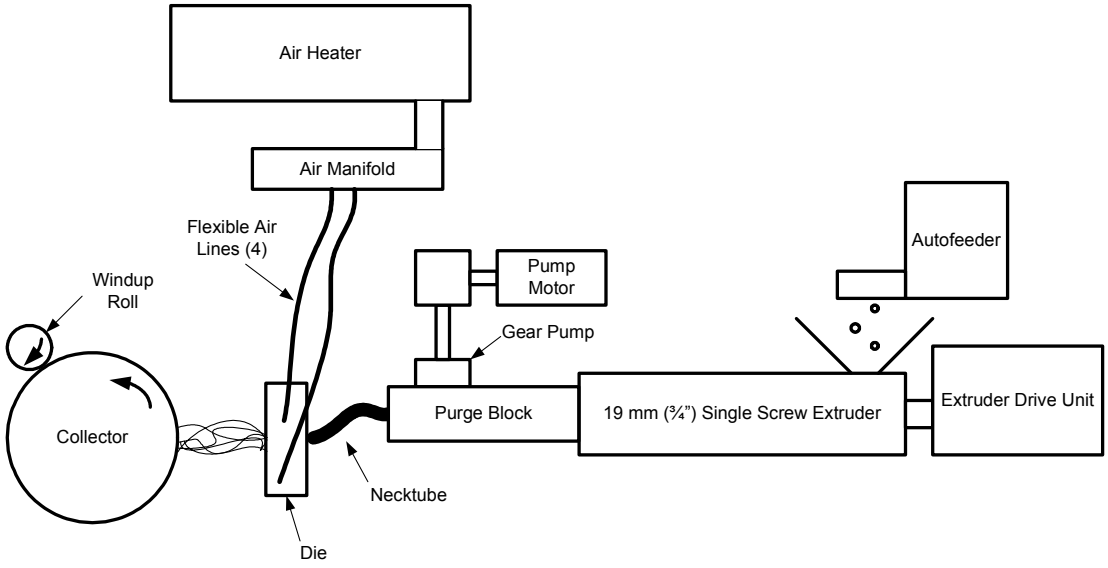

Figure 5.1. Diagram of the melt blowing process used in this work.

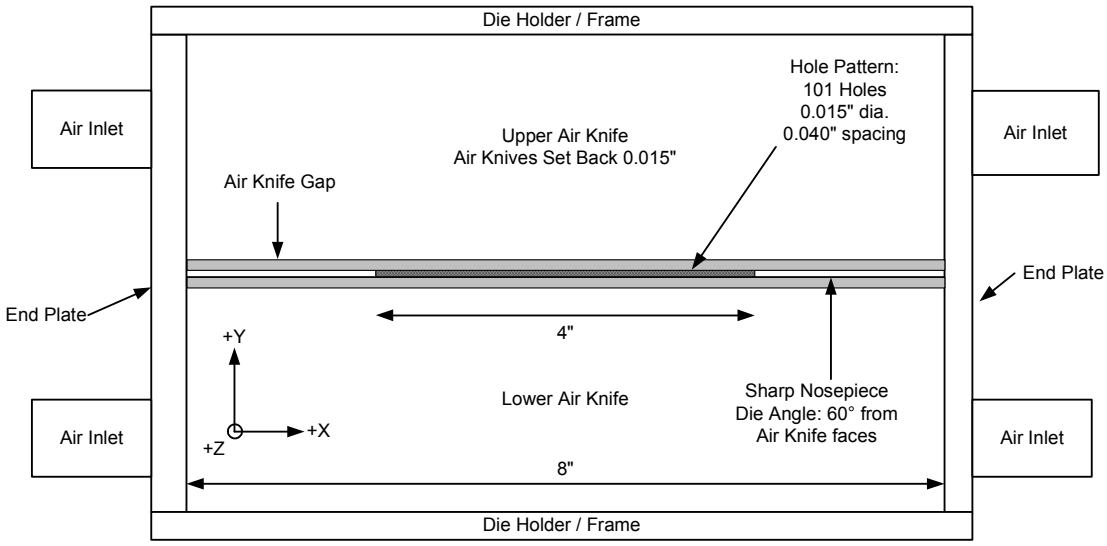

Figure 5.2. View of the face of the melt blowing die. The +z direction is perpendicular to the face, and the origin of the coordinate system is at the center of the die face. White represents metal, light grey represents air orifices, dark grey represents the area where the polymer capillaries are located.

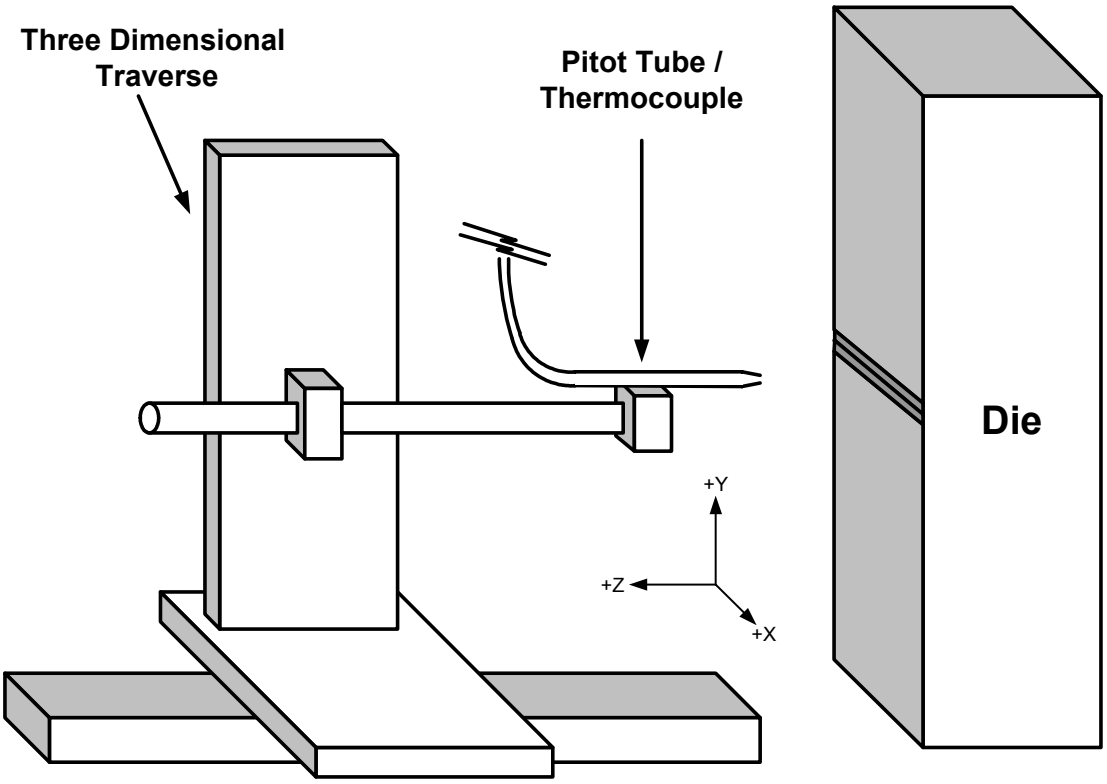

Figure 5.3. Pitot tube and thermocouple setup used.

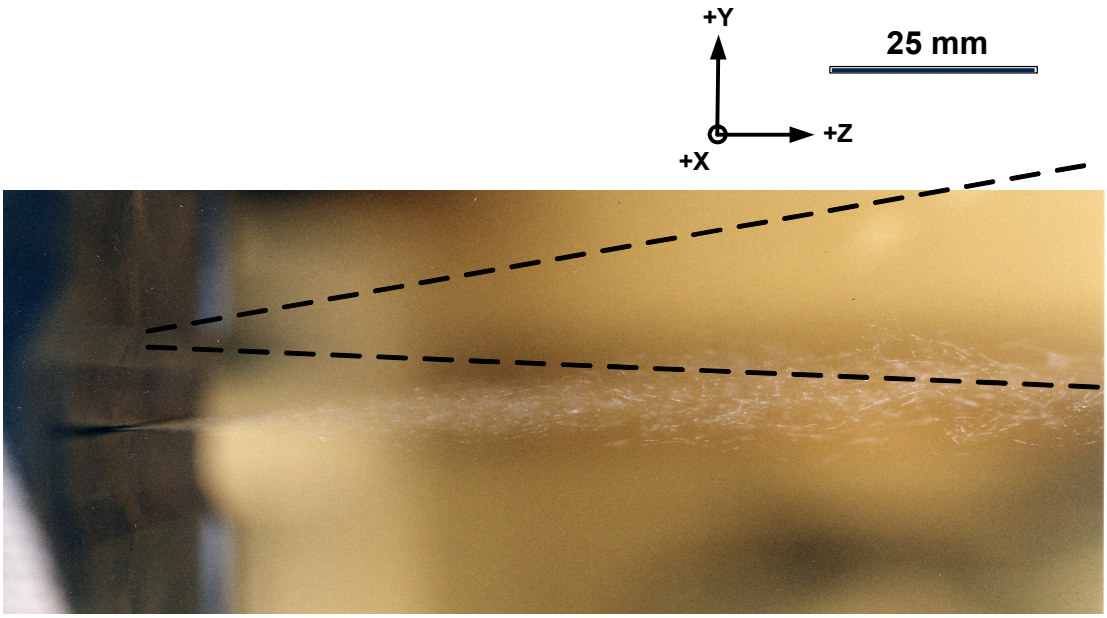

Figure 5.4. Photograph showing the fiber wedge near the die face.
Operating conditions: 5 lb/hr polymer flow, 2000 SLPM air flow, 300°C Die

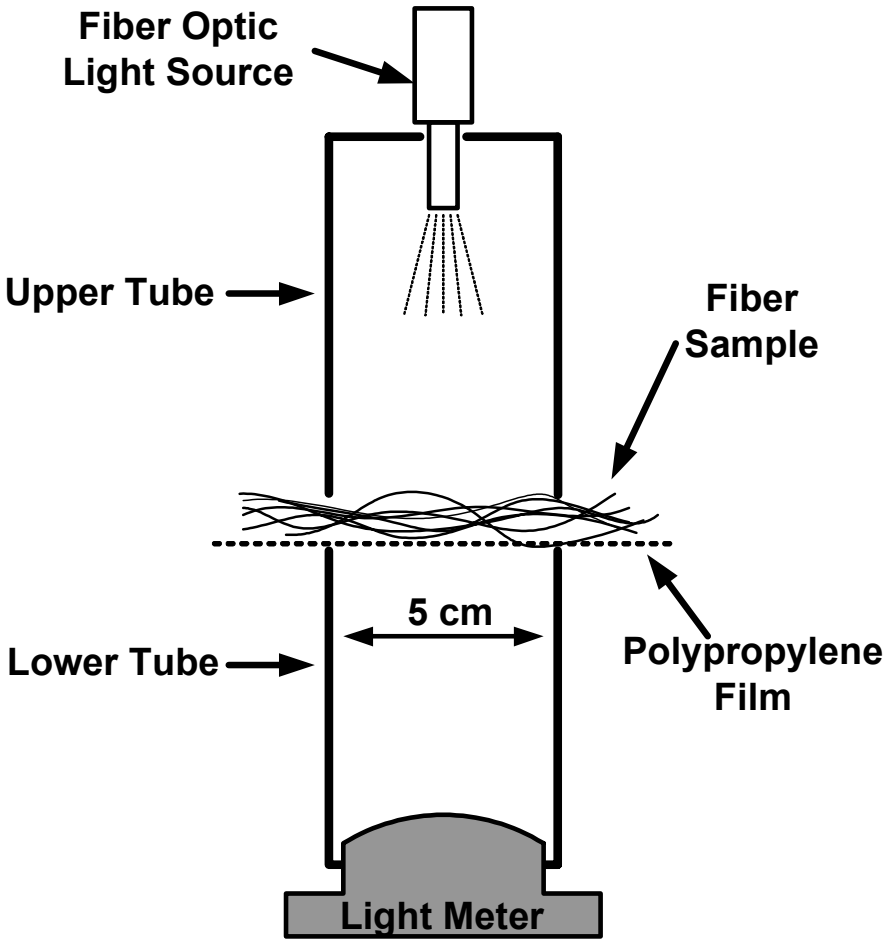

Figure 5.5. Light absorption apparatus used.

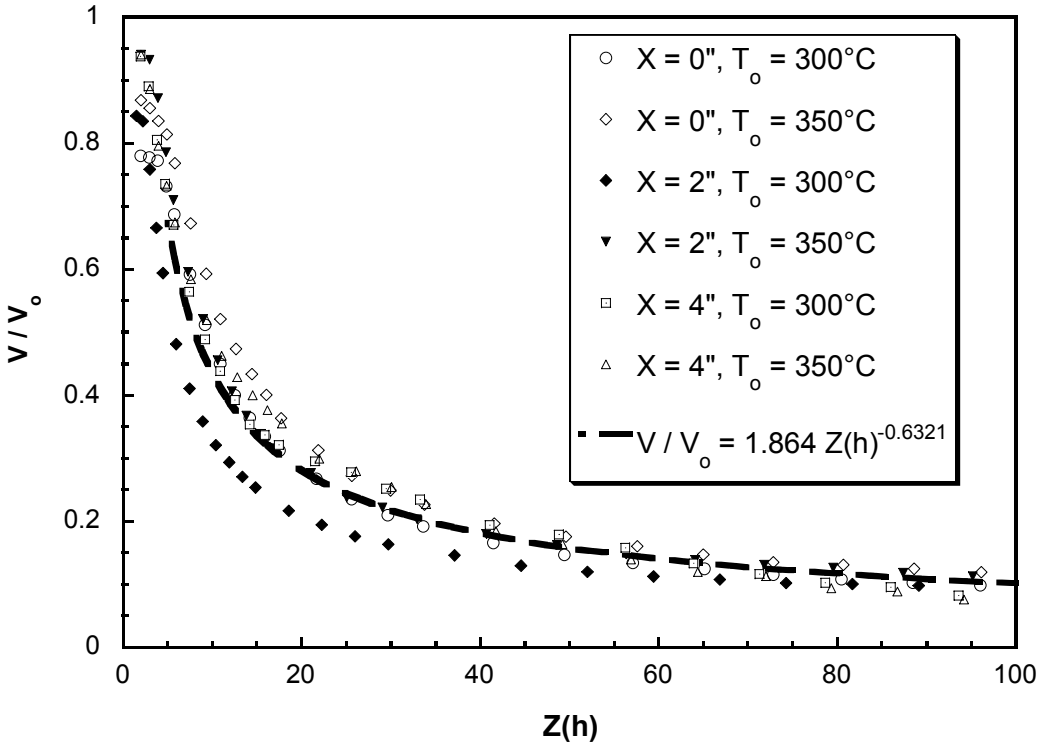

Figure 5.6. Velocity decay profiles. 0.025" air knife gap, 2500 SLPM air flow.

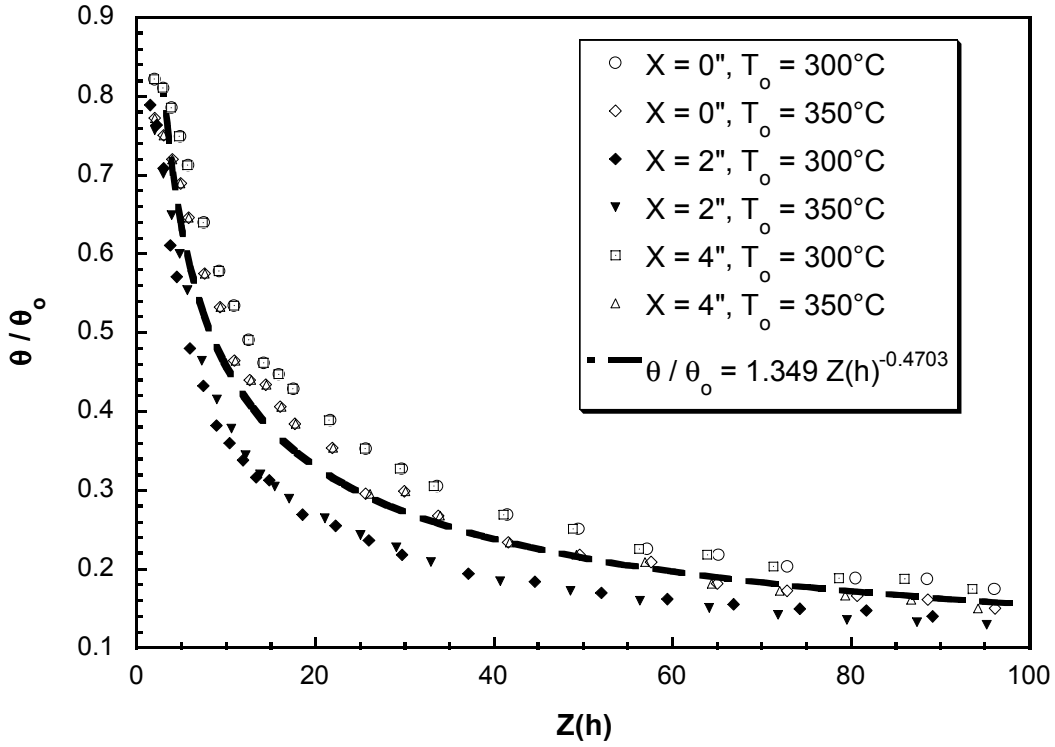

Figure 5.7. Temperature decay profiles. 0.025" air knife gap, 2500 SLPM air flow.

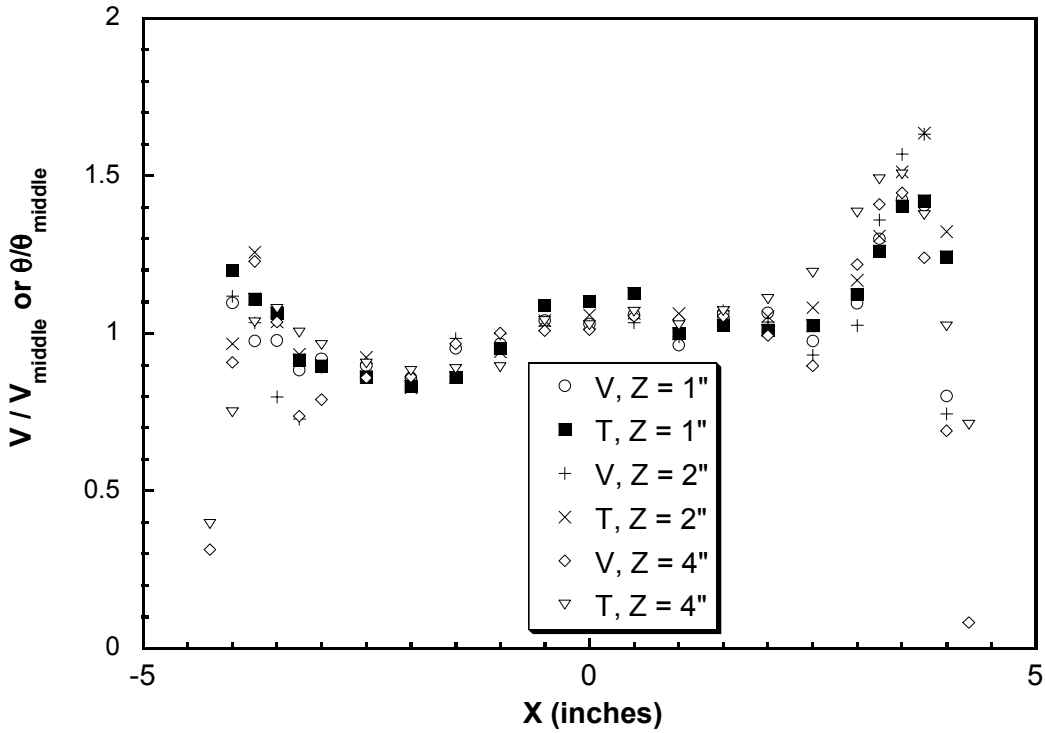

Figure 5.8. Horizontal velocity and temperature profile. 2500 SLPM air flow, 300°C die temperature, 0.025" air knife gap

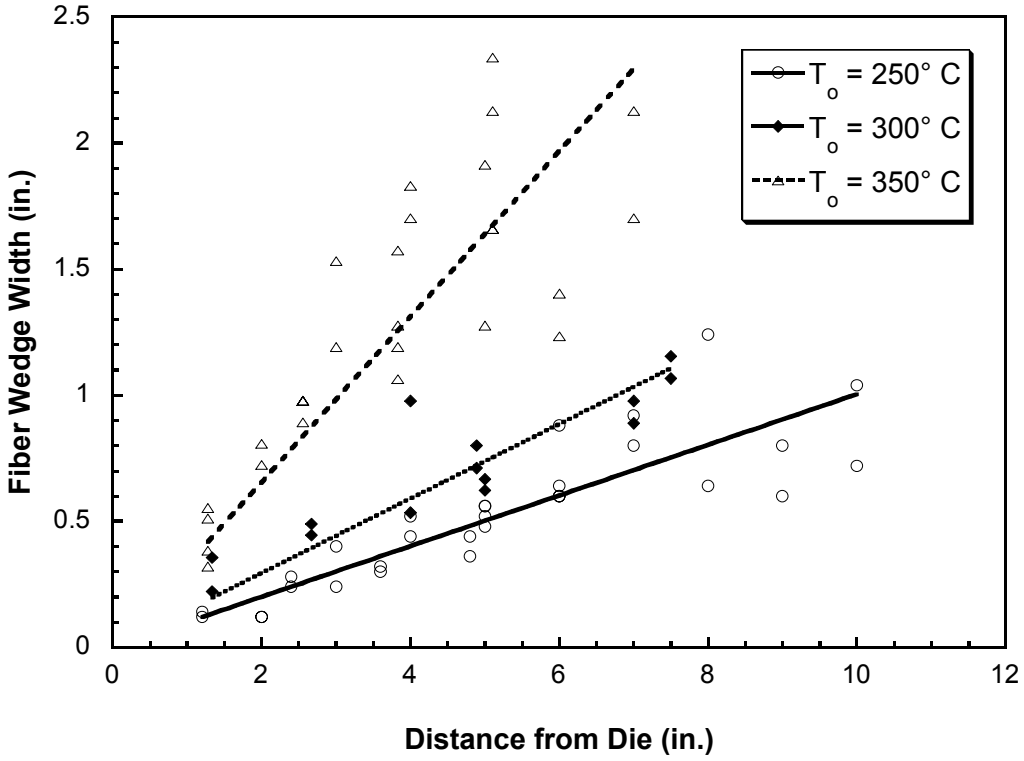

Figure 5.9. Fiber wedge width at various die temperatures. Air knife gap 0.025", Air flow 2500 SLPM

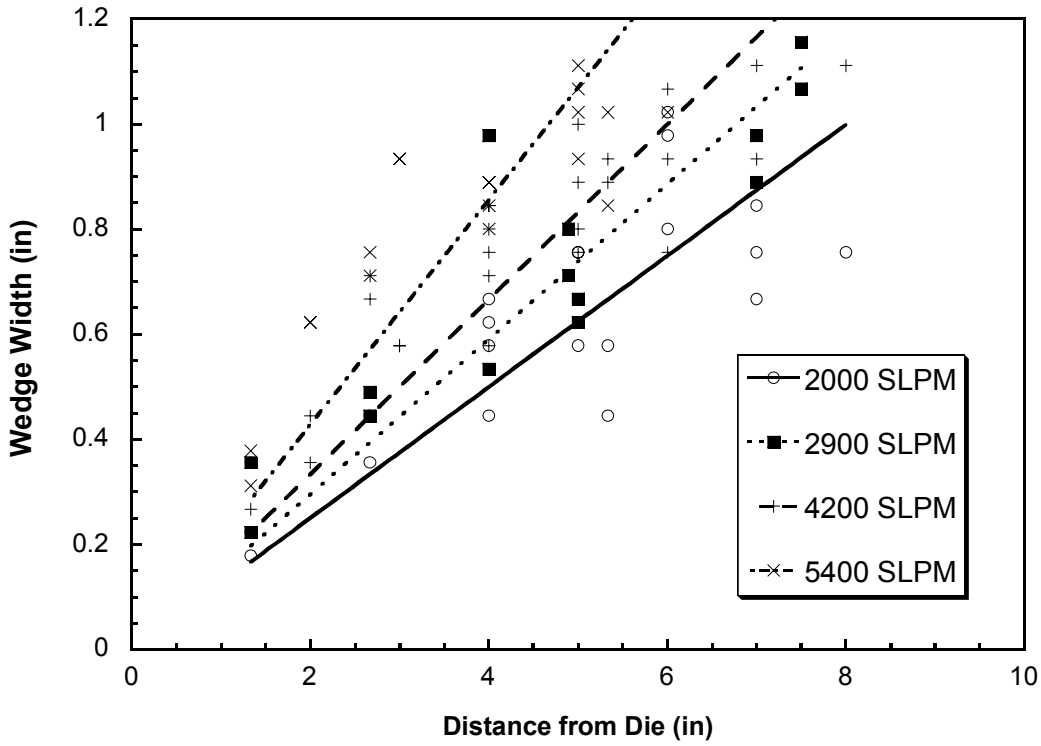

Figure 5.10. Fiber wedge width various air flow rates. 5 lb/hr polymer flow, 300°C die, 0.025" air knife gap

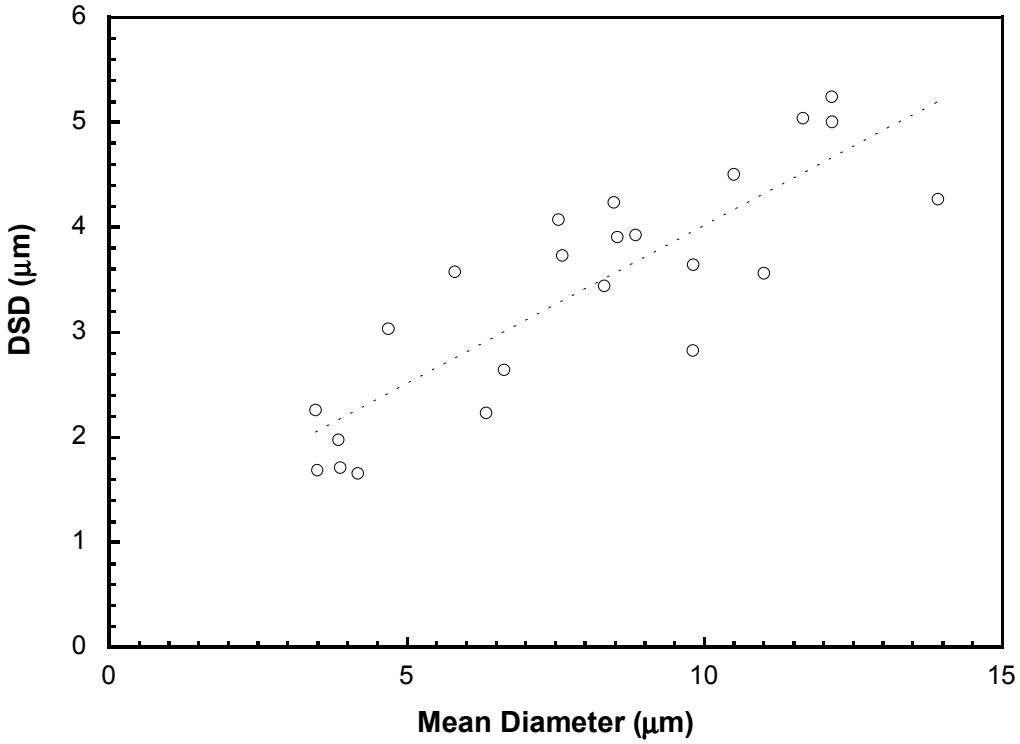

Figure 5.11. Diameter standard distribution (DSD) versus mean diameter.

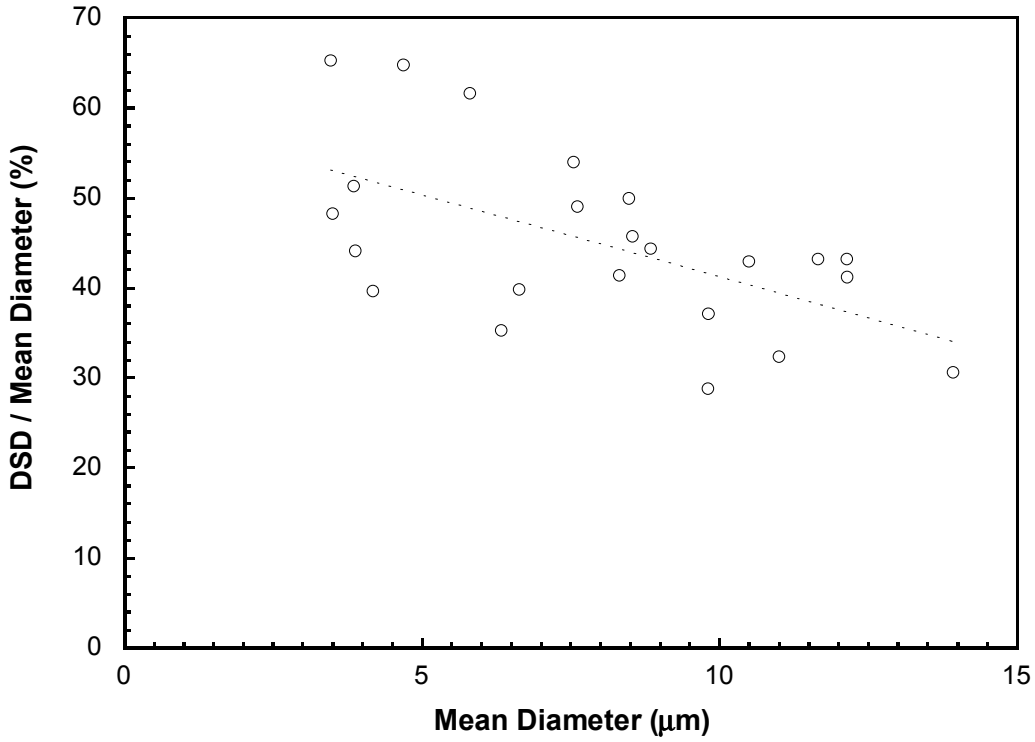

Figure 5.12. Normalized DSD versus mean diameter.

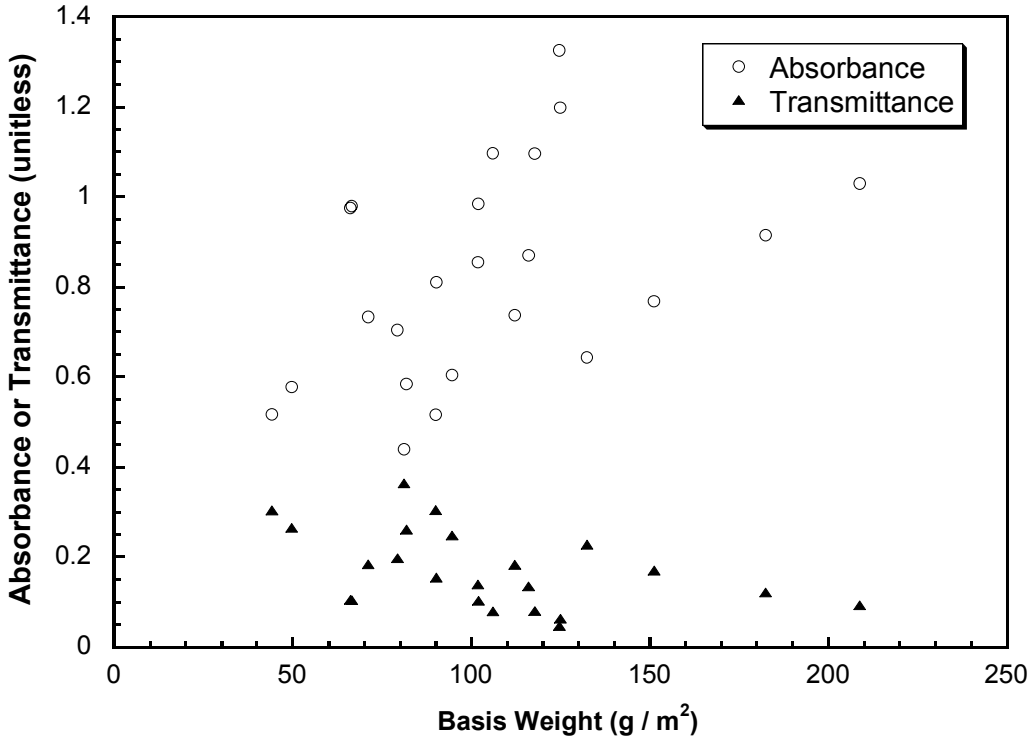

Figure 5.13. Absorbance and transmittance versus basis weight.

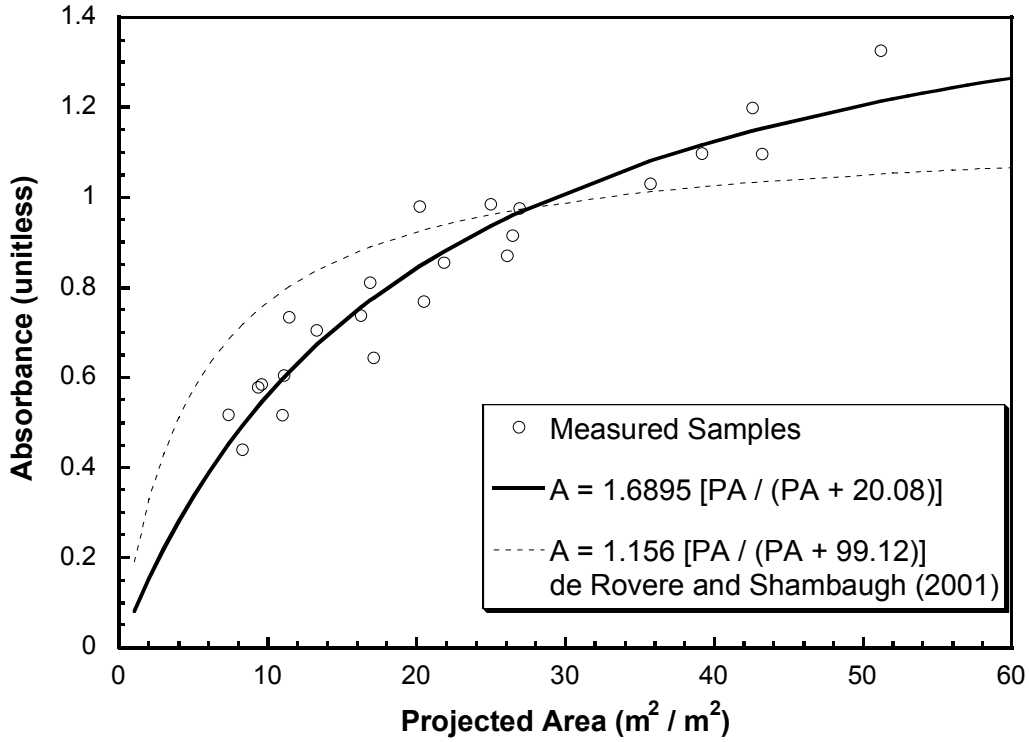

Figure 5.14. Absorbance versus projected area based on the mean diameter.

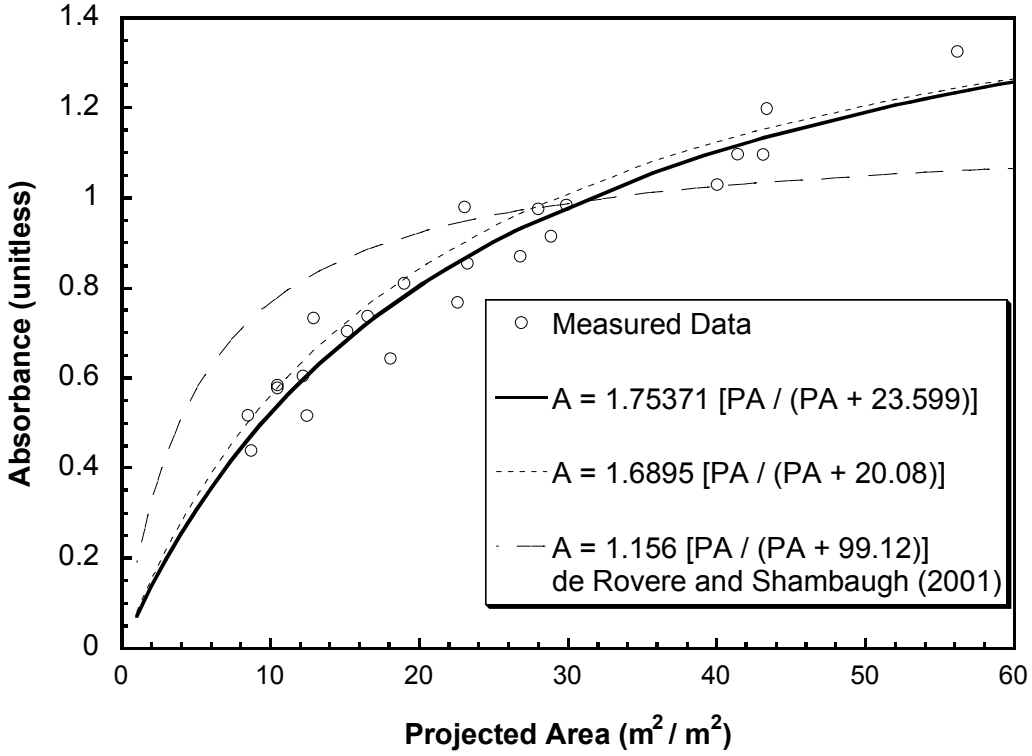

Figure 5.15. Absorbance versus Projected Area based on discretized diameter distribution.

Chapter 6

Experimental and Computational Study of the Aerodynamics of Swirling Nozzles for Deposition of Adhesives

6.1 Abstract

Swirl nozzles are used in the manufacturing industry for the deposition of adhesives in controlled patterns. The aerodynamics of swirl nozzles are a complex form of turbulent jet flow. Complications arise from locally high velocities, flow rotation, small dimensions, and complex geometry. The present work is a combined experimental and computational study of the flow field that results from a commercial swirl nozzle. A small-diameter Pitot tube was used to characterize the flow field of a swirl nozzle experimentally. The experiments also served to provide a standard for

the validation of computational studies of the same die. The computational analysis examined the effect of changing several design parameters, including the air flow rate, the orifice twist angle, and the jet pattern radius on the flow. It was found experimentally that the swirl nozzle jets have a higher decay constant than either circular or annular jets. Computations showed that the compressibility effects in the far field flow region were negligible and that high twist angles would prevent the merging of the individual jets into a single jet. For the cases in which a merging point exists, it was found that changing the radius of the jet orifice pattern did change the location of the merging point but did not prevent the merging of the jets.

6.2 Introduction

Swirl nozzles (Ziecker et al., 1988) represent a very specific class of melt blowing dies. They are used to deposit controlled quantities of adhesive, in a specific pattern, onto a substrate. The adhesive is melted, then pumped to the nozzle using conventional melt adhesive handling equipment. At the nozzle, air jets are used to deposit the adhesive onto the substrate. A variety of different melt adhesives may be used for this process. The patterns that may be applied using this technique vary; the swirl nozzles studied here produce interconnected loops on a flat substrate (curly-ques). Other nozzles can produce different patterns, including sinusoids and step waves. Applications for swirl nozzles include disposable diapers, cardboard boxes, and upholstery, among others. This process is illustrated in Figure 6.1.

Numerous researchers have studied and developed models for the melt blowing process (Rao and Shambaugh, 1993; Uyttendaele and Shambaugh, 1990;

Shambaugh, 1988). Marla and Shambaugh (2003) have developed a computational model that accounts for three-dimensional fiber formation and motion during the melt blowing process. This model requires the air flow field produced by a die to be known *a priori*. In conventional melt blowing, polymer streams are attenuated to a very small diameter, typically 1-30 microns, using air jets that are typically slot jets (commonly called Exxon dies; see Harding et. al., 1974) or annular dies (often called Schwarz dies; see Schwarz, 1983. In contrast, the primary purpose of a swirl nozzle is not necessarily to attenuate the adhesive stream, but to control the deposition pattern of the adhesive. Another important difference between conventional melt blowing and swirl nozzles is the interaction of multiple polymer streams. Melt-blowing dies can have thousands of holes within one die assembly; these multiple polymer streams interact, often with multiple individual fibers forming bundles or ropes before deposition. Swirl nozzles can also be used in groups (Allen and Fetcko, 1997), but in general they do not allow adhesive streams to interact; such interaction would hinder the controlled deposition. Despite the differences, the same fundamental principles apply to both systems; a stream of polymer (or adhesive) is deposited onto a collector (or substrate) using the drag force of one or more air jets to provide the attenuating force.

The die under experimental study in the present work is a single swirl nozzle die of commercial design (Nordson CF Nozzle Part Number 152456). A single adhesive orifice is at the center of the die, with six air jets surrounding it in an equally spaced radial pattern, as shown in Figure 6.2. The radius of this pattern is 2.11 mm , from the center of the polymer orifice to the center of any of the air orifices. The

polymer orifice sits at the tip of a cone, which is analogous to an outset nosepiece in a melt blowing die. Each of the six air jets is tilted in such a manner as to produce the swirling air pattern necessary for operation. For the purpose of convenient description, the angle of the air jets with respect to vertical will be described as by two separate angles, as seen in Figure 6.3. The first angle is the die angle, α, which is the angle between the vertical direction Z and the projection of the die hole on the RZ plane (Figure 6.3b). The second angle, the twist angle ϕ, is the angle between the vertical direction Z and the projection of the die hole on a plane perpendicular to the RZ plane (Figure 6.3c). The die under experimental study has a die angle $\alpha = 30°$, and a twist angle $\phi = 10°$. A die hole design such as this, i.e., involving a twist angle, leads to the formation of a twisting air flow pattern that directs the adhesive into a helical shape, depositing a 'curly-que' pattern onto the substrate.

6.3 Experimental Methods

Mean velocity was measured using a conventional Pitot tube setup. The Pitot tube used had an outer diameter of 0.7 mm and an inner diameter of 0.4 mm, with a tapered tip. The Pitot tube was attached to a three dimensional traverse, which could position the tube with 0.0254 mm resolution, as shown in Figure 6.4. Dwyer model 25 and 26 liquid manometers were used to measure the dynamic pressure at the Pitot tube. The model 25 and 26 manometers had ranges of –1.27 to 76.2 millimeters of water and –2.54 to 165.1 millimeters of water respectively. Static pressure was assumed to be the ambient pressure. The dynamic pressure was converted to velocity using Equation 1, which assumes ideal gas behavior.

$$V = \sqrt{\frac{2\gamma}{\gamma - 1} \frac{P_o}{\frac{MW \cdot P_o}{R_{ig} \cdot (T + 273.15)}} \left[\frac{P}{P_o}^{\frac{\gamma - 1}{\gamma}} - 1 \right]} \qquad (1)$$

It is well known that the angle between the Pitot tube and the mean flow direction (the angle of attack) can affect the measurement accuracy. Chue (1975) reported that this effect causes errors of less than 1% for angles less than 18°. Preliminary computational results predicted that for the measurements reported here the angle of attack is less than 18°. An additional factor that can complicate the Pitot tube measurements is the proximity of the die. At close distances to the die, the Pitot tube itself can influence the flow significantly. This interference makes the data obtained too close to the die inaccurate. Preliminary runs indicate that this interference is significant when the Pitot tube tip is closer than Z = 7.62 mm.

Coordinates are defined using a cylindrical coordinate system. . The origin of the coordinate system is set at the center of the jet orifice pattern. This places the origin inside the polymer capillary; however, it still serves as the most convenient place. The positive Z-axis runs directly away from the die face towards the ground. The R-axis is the distance away from the center of the die, parallel to the ground. The θ-axis is the rotation around the center of the die, with θ = 0° passing through one of the jet orifices at the die face.

Pitot tube measurements were taken along a total of five different lines. The first line was the centerline, which is the line of R = 0, with the Pitot tube moving away from the die face. Two lines were taken along θ = 0°, the first at Z = 8.19 mm, and the second at Z = 14.54 mm. These two passes are called the *across* passes, as

these lines pass directly underneath the jet orifices. The final two passes, the *between* passes, were taken at $\theta = 30°$, with Z = 8.19 mm and Z = 14.54 mm. The distances of Z = 8.19 mm and Z = 14.54 mm were chosen because those distances are exactly 0.25 inches (6.35 mm)and 0.50 inches (12.7 mm) respectively from the die tip, which served as the most convenient reference point on the nozzle.

6.4 Computational Methods

6.4.1 Geometry and Grid Generation

The six holed arrangement of the dies under study presented an obviously axisymmetric problem. Using rotational periodicity, a wedge shaped computational domain was constructed, representing $1/6^{th}$ of the total domain under study. The complex die geometry prohibited the use of an entirely hexagonal grid, as the polymer orifice cone prevents accurate hexagonal gridding near the die face. While a totally hexagonal grid is impossible due to geometry, a totally tetrahedral grid is impractical due to computational cost. Preliminary simulations showed that grids with as many as 2 million tetrahedral cells were insufficient to achieve grid independence, resulting in an unreasonable computational cost. Therefore, hybrid grids were generated that would consist of both types of cells; tetrahedral cells near the die face and hexagonal cells over the rest of the domain. The built in capabilities of the grid generation software used (Gambit™. from Fluent, Inc.) provided the means to accomplish this. Figure 6.5 shows the initial grid generation scheme, which places most of the cells near the die face. This initial grid generation method resulted in grids that were approximately 235,000 cells. Each change in geometric parameters,

either pattern radius or ϕ, required a new grid to be generated. The exact number of cells varied slightly with changes in the die geometry. In order to establish grid independence, two finer grids with 584,144 cells and 733,422 cells were generated. The initial, 235,000 cell grid did not match the results of the finer grids, hence improvement was necessary. However, in order to keep the computational time within a manageable range, the area close to the die face was refined, because that is the area where most of the flow changes happen. The area of the grid with $Z < 50.8$ mm and $R < 6.25$ mm was refined, resulting in grids that had approximately 340,000 cells. Figure 6.6 shows the centerline velocity profiles of the 340,000 cell grid against both of the higher resolution grids, the match is nearly perfect. With such good agreement across these three different sized grids, the grid with 340,000 cells was selected for the solution runs.

6.4.2 Turbulence Modeling

Selection of the most effective turbulence model for a given problem is one of the biggest challenges in Computational Fluid Dynamics (CFD). Many different turbulence models have been developed, with varying amounts of complexity, applicability, and accuracy. For industrial flows, the most commonly used models are based on the Reynolds Averaged Navier-Stokes (RANS) equations (Wilcox, 1994; Pope, 2000; Durbin and Petterson Reif, 2001). The RANS based models have reasonable computational cost, and can be accurate enough for simulating many different flows. However, RANS models require empirical equations and constants in order to close the system of averaged momentum equations. The choice of

equations and constants can have dramatic effects on the results generated through RANS based CFD. More advanced models for the study of turbulent flows are available, notably Large Eddy Simulation (LES) and Direct Numerical Simulation (DNS), however these models have far too much computational expense to be applied to the present work.

The k-ε model for RANS closure is one of the most widely applied models in CFD. This two-equation model provides reasonably good answers to many different problems. Previous work with melt blowing jets, from Krutka et al.,(2002, hereafter referred to as KSP; 2003) and Moore et al.(2004, hereafter referred to as MSP) has shown that k-ε modeling is not particularly accurate in the case of melt blowing jets. The present work re-examines that result for swirl nozzles.

In an effort to improve the accuracy of their simulations, KSP and MSP calibrated the Reynolds Stress Model, RSM (Launder, 1975) using experimental data for slot and annular melt blowing jets, respectively. They found that the RSM model could give good results for the centerline mean velocity decay. MSP also showed that with appropriate calibration the RSM model could also give reasonably accurate estimates of the jet spreading rate for an annular jet and compressible flow.

6.4.3 Calculation Procedure

Calculations were done using the commercial software package FLUENT® version 6.1, from Fluent, Incorporated. Due to the locally high velocities the flow was assumed to be compressible. The coupled-implicit solver, using ideal gas air density, was chosen to handle the compressible nature of the flow near the die face. Thermal properties, other than density, were assumed constant at their ambient

values. With nearly isothermal flow, the assumption of constant thermal properties is accurate. Numerous preliminary runs were conducted experimenting on the numerical stability of the RSM turbulence model applied to the case of a swirl die. It was observed that the RSM turbulence model would diverge consistently when using 2^{nd} order upwind discretization. The k-ε model on the other hand, was quite stable under 2^{nd} order upwind discretization. KSP has showed that for slot dies, the RSM model produced better results than the k-ε model when both models were utilizing 2^{nd} order upwind discretization. However, due to this stability constraint, the present computation work was done with 2^{nd} order upwind discretization for the k-ε model, and 1^{st} order upwind discretization for the RSM model.

Boundary conditions were set similarly to the work of MSP and KSP. Inlets were set as mass flow inlets, with a static temperature of 300 K. Outlets were set to be pressure outlets, with backflow temperatures of 300 K. The upper surface, as well as the die faces were set as no-slip walls, isothermal at 300 K. The turbulence intensity was set for the inlets and outlets at 10%, with 0.457 mm hydraulic diameter for the inlets and 25.4 mm hydraulic diameter for the outlets.

Initial calculations were performed using the standard k-ε model and 1^{st} order upwind discretization. After the simulation achieved a moderate level of convergence, the turbulence model was changed to the final model, and discretization was changed, if necessary (to 2^{nd} order upwind for the k-ε model). Computationally, this is a relatively large problem for a workstation, with a typical case consuming 50 to 100 hours using a 2.2 GHz Xeon™ processor. The amount of memory needed varied depending on case (and turbulence model), but 1000 MB was typical. As

expected, the k-ε cases required substantially less time and memory to run, because of the simpler turbulence model.

6.5 Results

6.5.1 Pitot Tube Measurements

The velocity profile along the centerline (i.e., the line of R = 0) is very important, because the polymer fiber is mostly moving in that region, and it can provide the jet decay. Measurements taken at two different air flowrates are shown in Figure 6.7. It is important to note the generally poor data at locations where Z < 6.5 mm, this due to interference of the Pitot tube on the flow. These measurements are considered unreliable, and do not indicate the true flow near the nozzle face. Normalization is done by dividing the mean velocity by the mass flow rate of the air through the die, as shown in Figure 6.8. This normalization brings the results of two different air flow rates to a single curve. Fitting the data where Z > 12.7 mm to a power law expression results in Equation 2, which is also shown on Figure 6.8. Note that the decay exponent (-0.7511) is larger in magnitude than the value observed for circular jets (-0.5,Schlichting, 1979) or observed in conventional annular melt blowing dies (-0.532, see Tate and Shambaugh, 1998).

$$\frac{V}{\dot{m}} = 1807.45 \cdot Z^{-0.7511} \qquad (2)$$

This increased decay constant is most likely due to higher levels of turbulence generated by the multiple interacting jets. It has been seen that melt blowing jets in

general produce higher decay constants than analogous simple jets (KSP; MSP; Uyttendaele and Shambaugh, 1989). It makes physical sense that this much more complex, multiple jet geometry should have even higher levels of turbulence, resulting into increased centerline velocity decay constant.

The radial profile measurements are also presented. As shown in the work of MSP and KSP, the CFD techniques used here do not always give accurate results with respect to jet merging and spreading. Figure 6.9 shows the profiles for the radial profile with $\theta = 0°$. It is important to note the change in jet shape with distance. At Z = 8.19 mm, the jet still has peak velocities away from the centerline, while at Z = 14.54 mm, the peak velocity is at the centerline. This suggests that at large distances, the jet will decay in a manner similar to circular and annular jets.

6.5.2 CFD Simulations

6.5.2.1 Effect of turbulence model

Determining the most effective turbulence model is of great importance. Even small changes in the turbulence model can cause very large changes to the flow solution. Using the Pitot tube data as a reference, the k-ε and RSM model results were compared. Centerline velocity profiles, as shown in Figure 6.10, show that the k-ε model seems to fit the experimental data better than the RSM model. Of particular note is the difference in the peak velocity shape near Z= 6.35 mm. The k-ε model shows a single, well defined velocity peak, while the RSM model shows two clearly defined velocity peaks separated by a local minimum. The experimental data in this range is not as reliable; hence a definitive conclusion as to the actual peak shape cannot be reached. There does not appear to be a physical reason that would

result in two mean velocity peaks along the centerline. It is also important to note that the k-ε model fits much better than the RSM model in the middle region, Z = 10 to 40 mm. In the far field, Z > 40 mm, the two turbulence models give approximately the same results, and are a good match with experiments at least as far as Z = 50 mm.

Radial velocity profiles show similar model dependence to the centerline velocity profiles. Figure 6.11 shows the radial velocity profile at Z=8.19 mm. Note that while the RSM velocity peak is still away from the centerline, the k-ε velocity peak is on the centerline, indicating that the six individual jets have merged in one. Experimental data also show that the jet has not entirely merged by Z = 8.19 mm. In this respect, the RSM model accounts for the initial jet development better than the k-ε model. The jet behavior at Z = 14.54 mm as shown in Figure 6.12, shows similar behavior, with the k-ε model merging quicker than the RSM model. At this point however, the k-ε model still fits the experimental data a little better. It is important to note that while the passes at θ = 0° and θ = 30° do show slightly different behavior, the differences are minor, and the vertical component of the velocity is nearly independent of θ at distances beyond Z = 8.19 mm.

6.5.2.2 Effect of air flow rate

Air flow through the die is a large factor in the operating characteristics of a swirl nozzle. The deposition pattern can be controlled through the air flow with extreme values producing unacceptable results (i.e., either no swirl or too much swirl). The effect of air flow rate is studied, and it is found that while the magnitude of the air velocity has the expected dependence, the general flow pattern does not show any strong dependence. Figure 6.13 shows four cases run with 0.12 g/s and

0.24 g/s air flow; while the magnitude of the velocity profile changes the shape of the velocity profile is nearly the same for all cases. Normalization of the centerline velocity profile, using the mass air flow rate through the die, shows that the normalized velocity profiles are nearly identical for both flow rates (Figure 6.14). It is safe to conclude that with subsonic inlet velocities, the far field jet development is only weakly affected by compressibility effects.

6.5.2.3 Effect of twist angle

Three different twist angles were studied using CFD, $\phi = 10°$ (same as the experimental nozzle), 20°, and 40°. The effect of increasing the twist angle on the centerline velocity profiles can be seen in Figure 6.15. The profile changes with increasing ϕ are rather dramatic, particularly for the $\phi = 40°$ case. While the $\phi = 10°$ case shows a profile not unlike an annular jet (see MSP), the $\phi = 40°$ case shows an entirely different flow pattern, even at large distances from the die face. At large twist angles the jets no longer merge, rather the individual jets retain most of their identity but still interact with each other. The radial velocity profiles for increased twist angles are shown in Figures 6.16 and 6.17. The figures show that while for the $\phi = 10°$ and $\phi = 20°$ cases the jets eventually merge into a single jet, the $\phi = 40°$ case shows little sign of merging. This result implies that there is some maximum twist angle at which the jets will merge, and that this limit is between 20° and 40°. Figures 6.18a, 6.18b, and 6.18c show the path lines emanating from the inlet for $\phi = 10°$, 20°, and 40°, respectively. The change from merging to diverging behavior is apparent from the shape of the plots. These figures also help illustrate the centerline behavior of each of the jets. In particular, for the $\phi = 40°$ case the jets really never cross the

centerline of the flow. The entrainment of the individual jets causes an inflow, and negative V_z, along the centerline.

6.5.2.4 Effect of air orifice pattern radius

The air orifice pattern radius was changes from the experimental 2.11 mm to 1.65 mm and 3.18 mm to explore the effect on the air flow field. The effect of changing the air orifice pattern radius is shown in Figures 6.19, 6.20, and 6.21. Figure 6.20 shows the centerline velocity profiles for all three cases. The basic shape is constant for all three cases, however the peak velocity changes substantially with changing pattern radius. In the far field the velocities do approach each other, as expected. Given the inherent similarities between this case and an annular jet, it was attempted to normalize die distance with the pattern radius. (This is equivalent to normalizing an annular jet by it's outer diameter, see MSP.) This resulted in even more disparity between the three cases; hence it is not always accurate to apply circular or annular jet flow analysis to the overall flow field of a swirl nozzle.

The initial jet development was also examined. Figure 6.20 shows a z-velocity radial profile with Z = 8.19 mm. It is apparent that the change in pattern radius affects the distance required for the jets to merge. At Z=8.19 mm, both of the smaller pattern radius cases have effectively merged, while the 3.18 mm case still have not fully merged. At Z=14.54 mm all three cases exhibit jets that have merged, showing that the merging is not prevented by the change in pattern radius.

6.6 Conclusions

The flow field of a commercial swirl nozzle was studied experimentally. CFD analysis was performed on a commercial nozzle geometry and several design variants. It was found that in some limited respects, conventional circular jet analysis techniques may be applied to the swirl nozzle. It was found that the standard k-ε model, using 2nd order upwind discretization generally provided more accurate results than the Reynolds Stress Model using 1st order upwind discretization. Compressibility effects were found to be negligible in the far field flow development. For the experimental die geometry it was found, both experimentally and through CFD that the centerline velocity profile can be normalized by the mass air flow rate. By varying the twist angle, the swirl nozzle jets transition from merging behavior to diverging behavior by $\phi = 40°$.

6.7 Nomenclature

$\dot{m}$ = Mass flow rate of air through the air orifices (g / s)

MW = Molecular weight of air (g / mol)

P = Dynamic pressure (Pa)

P_o = Static pressure (Pa)

R = Radial Coordinate (cm)

R_{ig} = Ideal gas constant (J / mol K)

T = Air Temperature (°C)

V_z = Mean velocity in the Z direction (m /s)

Z = Vertical coordinate (cm)

Greek Characters

α = Die angle, see Figure 6.3 (°)

ϕ = Twist angle, see Figure 6.3 (°)

γ = Specific heat ratio

θ = Polar coordinate (°)

6.8 References

Allen, M.A.; Fetcko, J.T. "Modular melt blowing die" U.S. Patent 5,618,566, **1997**.

Chue, S.H. Pressure Probes for Fluid Measurement. *Prog. Aerospace Sci.*, *16* (2), **1975**.

Durbin, P.A.; Petterson Reif, B.A. *Statistical Theory and Modeling for Turbulent Flows*; John Wiley and Sons Ltd.:West Sussex, England, **2001**.

Harding, J.W.; Keller, J.P.; Buntin R.R. "Melt-blowing Die for Producing Nonwoven Mats", U.S. Patent 3,825,380, **1974**.

Krutka, H.M.; Shambaugh, R.L.; Papavassiliou, D.V. Analysis of a Melt-Blowing Die: Comparison of CFD and Experiments. *Ind. Eng. Chem. Res.*, **2002**, *41*, 5125-5138.

Krutka, H. M.; Shambaugh, R. L.; Papavassiliou, D. V. Effects of Die Geometry on the Flow Field of the Melt Blowing Process. *Ind. Eng. Chem. Res.,* **2003**, *42*(22), 5541-5553.

Launder, B.E., G. J. Reece, and W. Rodi. Progress in the Development of a Reynolds-Stress Turbulence Closure. *J. Fluid Mech.*, **1975**, *68*, 537-566.

Marla, Vishnu T.; Shambaugh, R.L. Three-Dimensional Model of the Melt-Blowing Process. *Ind. Eng. Chem. Res*. **2003**, *32*, 6993-7005.

Moore, E.M.; Shambaugh, R.L.; Papavassiliou D.V. Analysis of Isothermal Annular Jets: Comparison of CFD and Experimental Data. *J. Appl. Polym. Sci*., **2004**, in press.

Pope, S.B. *Turbulent Flows*; Cambridge University Press: Cambridge, United Kingdom, 2000.

Rao, R.S.; Shambaugh, R.L., "Vibration and Stability in the Melt Blowing Process." *Ind. Eng. Chem. Res.*, **1993**, *32*, 3100-3111

Schlichting, H., Boundary-Layer Theory 7th ed., McGraw-Hill, pp. 729-735, **1979**.

Schwarz, E.C.A. "Apparatus and Process for Melt-Blowing a Fiberforming Thermoplastic Polymer and Product Produced Thereby", U.S. Patent 4,380,570, **1983**.

Shambaugh, R.L. A Macroscopic View of the Melt Blowing Process for Producing Microfibers. *Ind. Eng. Chem. Res.* **1988**, *27*(12), 2363-2372.

Tate, B.D.; Shambaugh, R.L. "Modified Dual Rectangular Jets for Fiber Production", *Ind. Eng. Chem. Res.*, **1998**, *37*, 3772-3779.

Uyttendaele, M.A.; Shambaugh, R.L. "The Flow Field of Annular Jets at Moderate Reynolds Numbers." *Ind. Eng. Chem. Res.*, **1989**, *28*, 1735-1740.

Uyttendaele, M.A.; Shambaugh, R.L. "Melt Blowing: General Equation Development and Experimental Verification", *AIChE J.,* **1990**, *36*, 175-186.

Wilcox, D.C., Turbulence Modeling for CFD, DCW Industries, La Canada, California, **1994.**

Ziecker, R.A.; Boger, B. J.; Lewis, D.N. "Adhesive Spray Gun and Nozzle Attachment", U.S. Patent 4,785,996, **1988**.

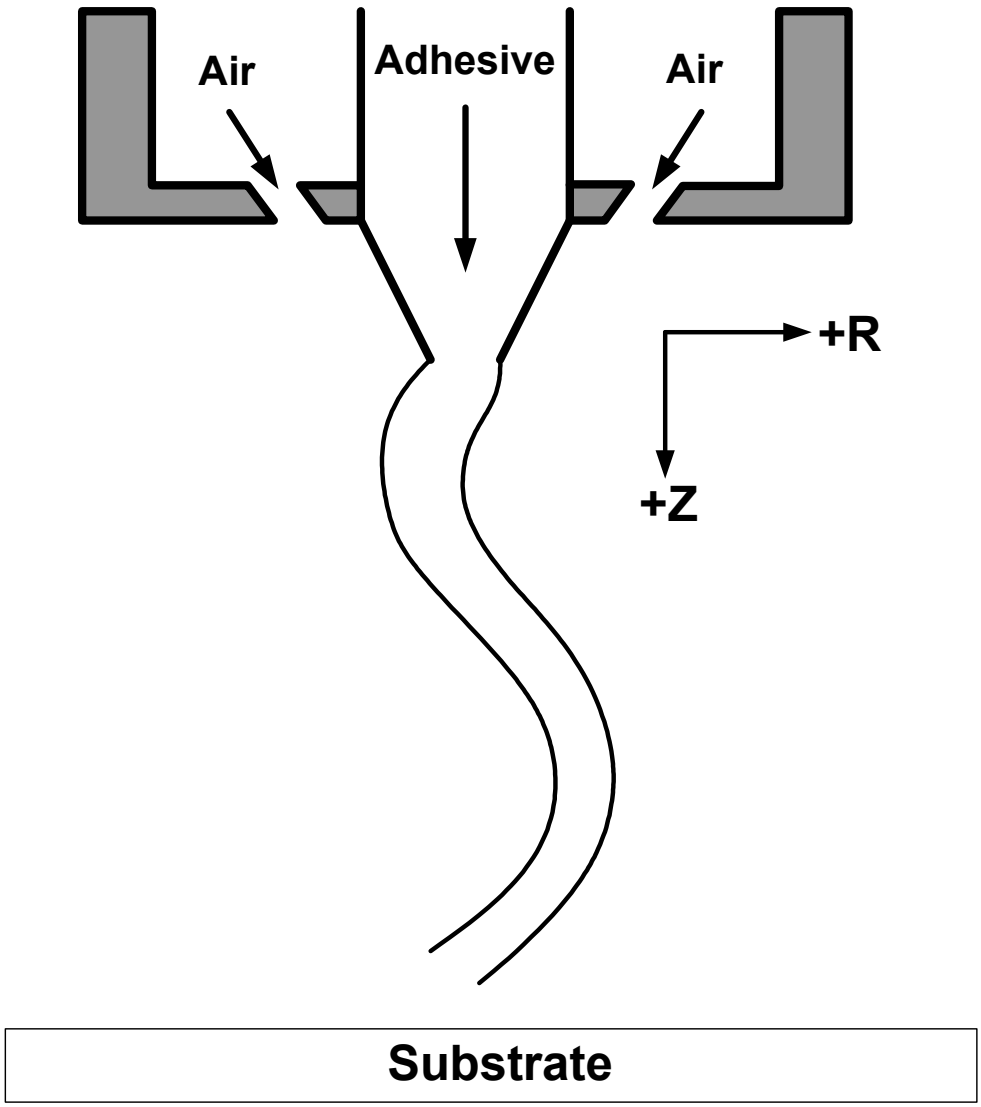

Figure 6.1. Diagram of the operation of a swirl nozzle.

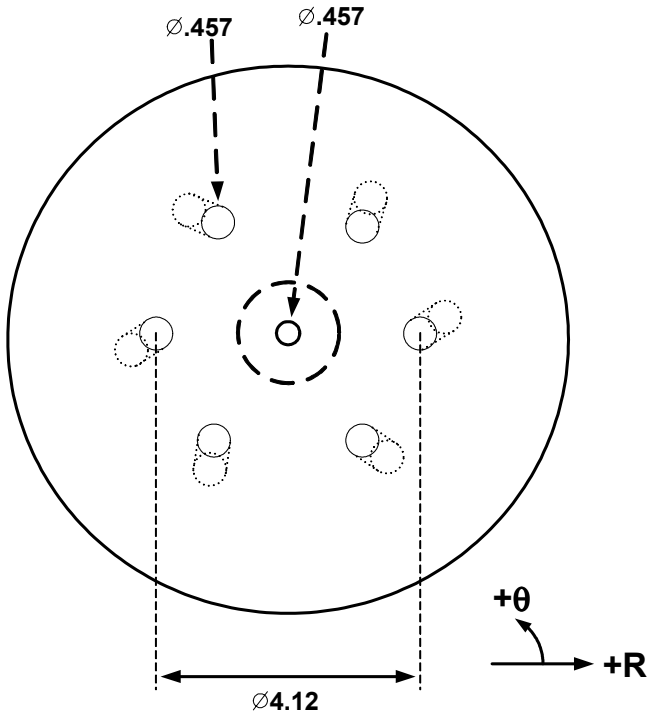

(a.)

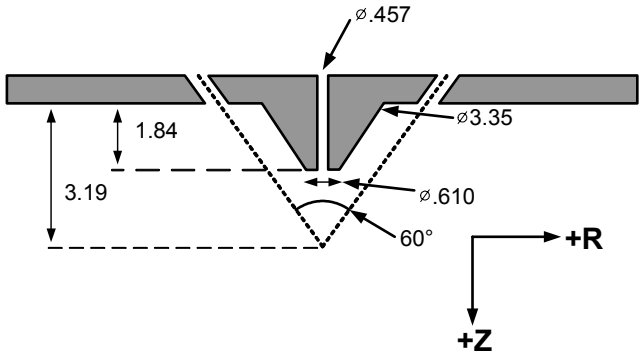

(b.)

Figure 6.2. a. Bottom view of the nozzle experimentally studied. b. Cross sectional view of the swirl nozzle experimentally studied. All linear dimensions in millimeters.

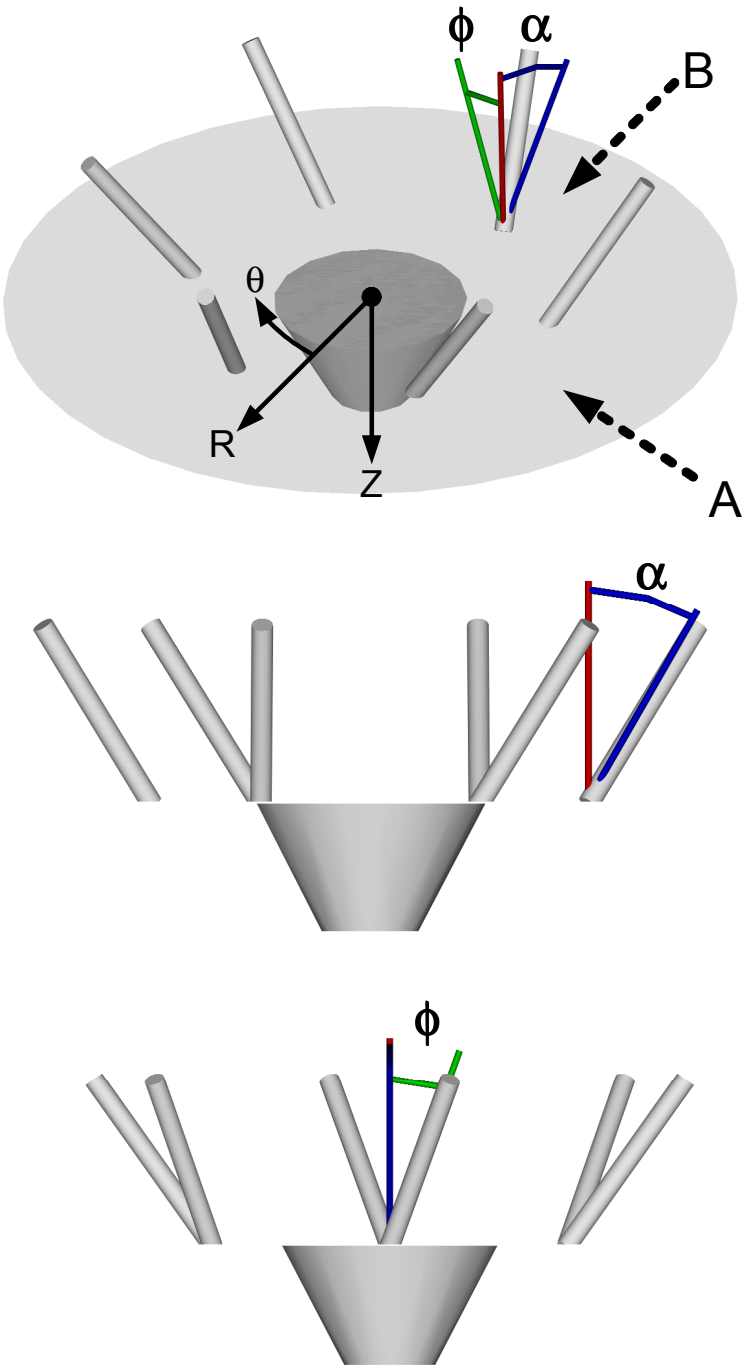

Figure 6.3. Three views of the die angles in a six hole swirl nozzle. Top – Perspective View, Middle – View from axis A, Bottom – View from axis B.

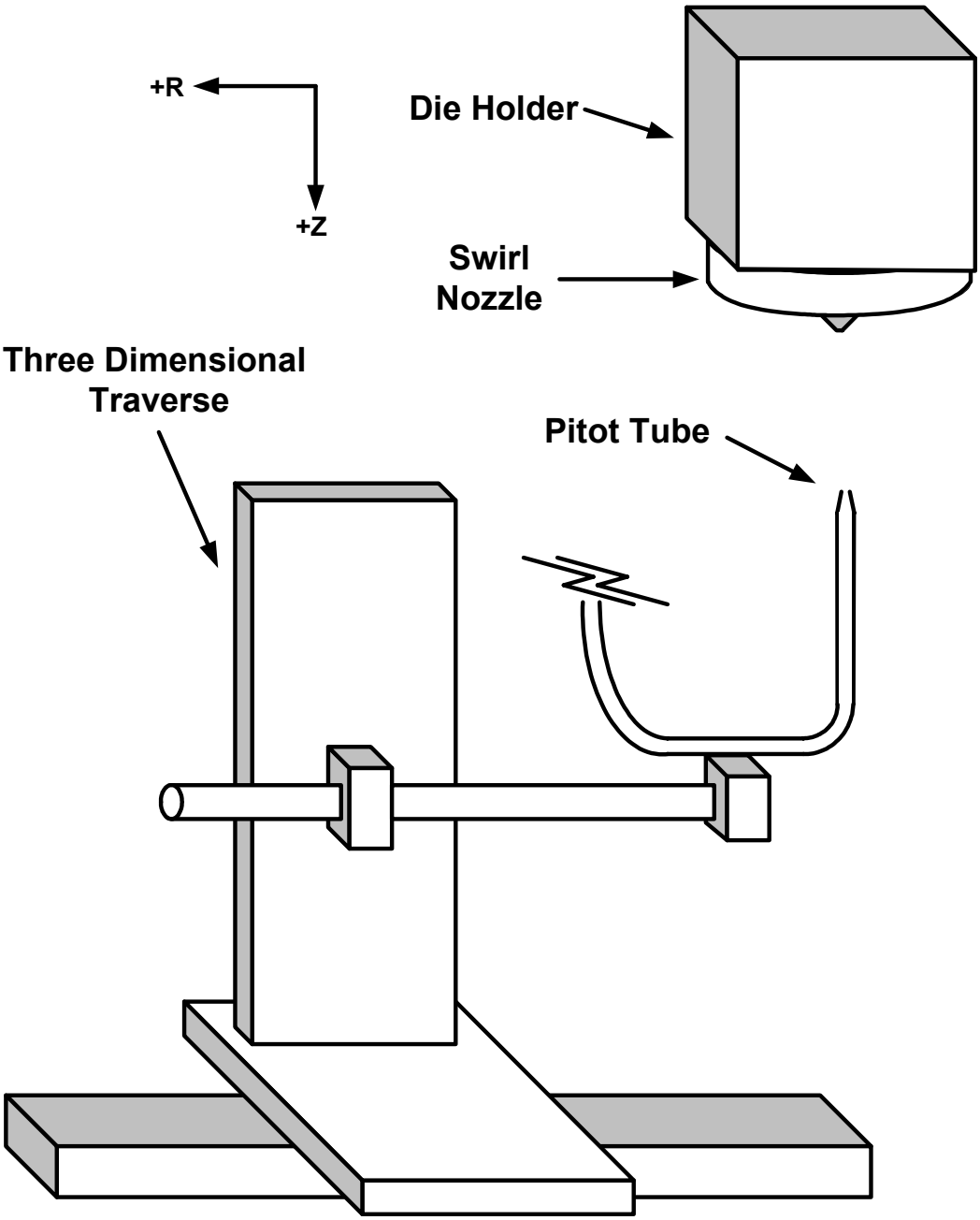

Figure 6.4. Experimental Pitot tube apparatus to collect velocity data.

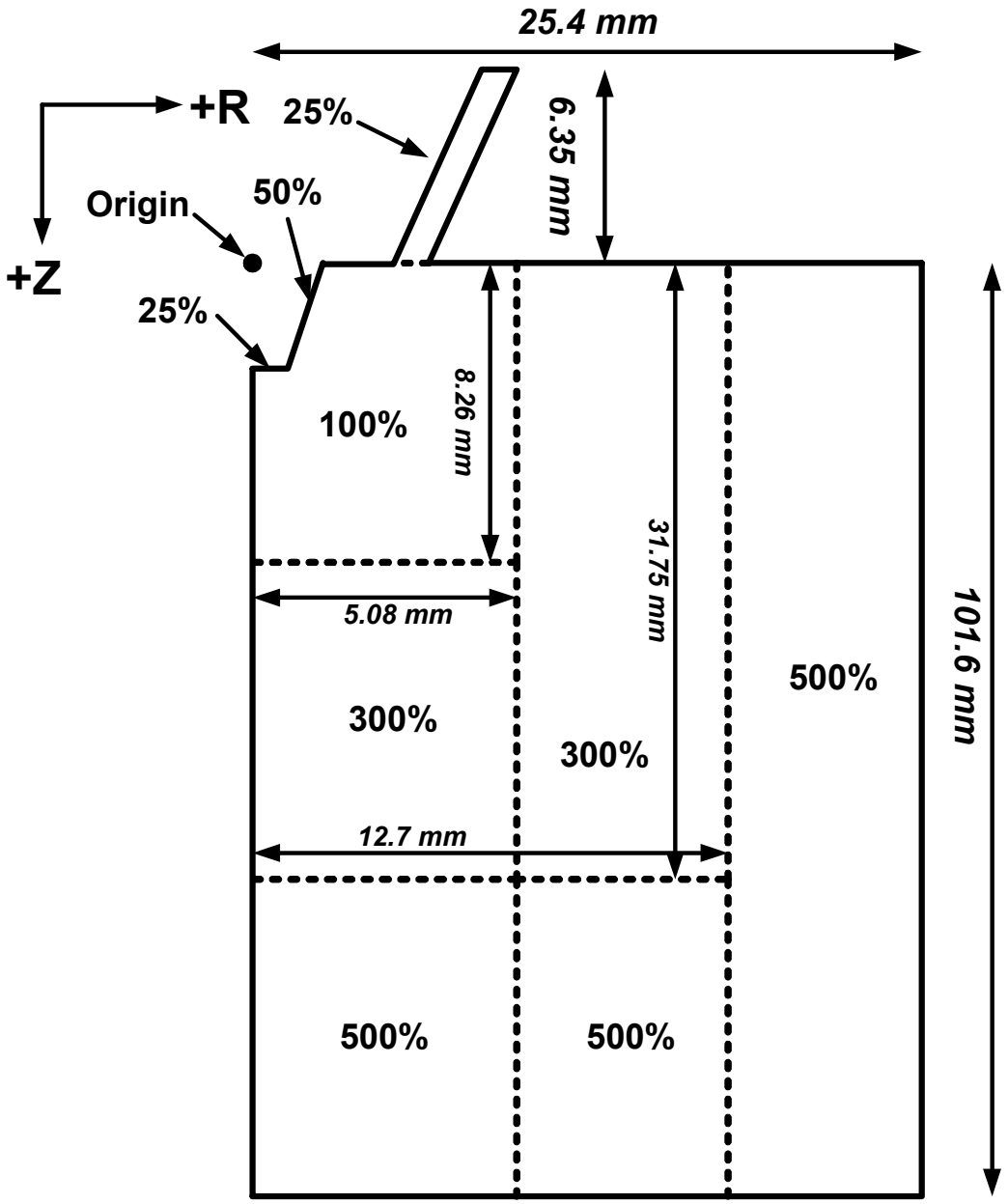

Figure 6.5. Initial computational domain generated. Dimensions are in inches, and each region has the grid sizing (as a percentage of 0.305 mm). The inlet region and region of 100% grid sizing use tetrahedral grids, all other regions use hexahedral grids.

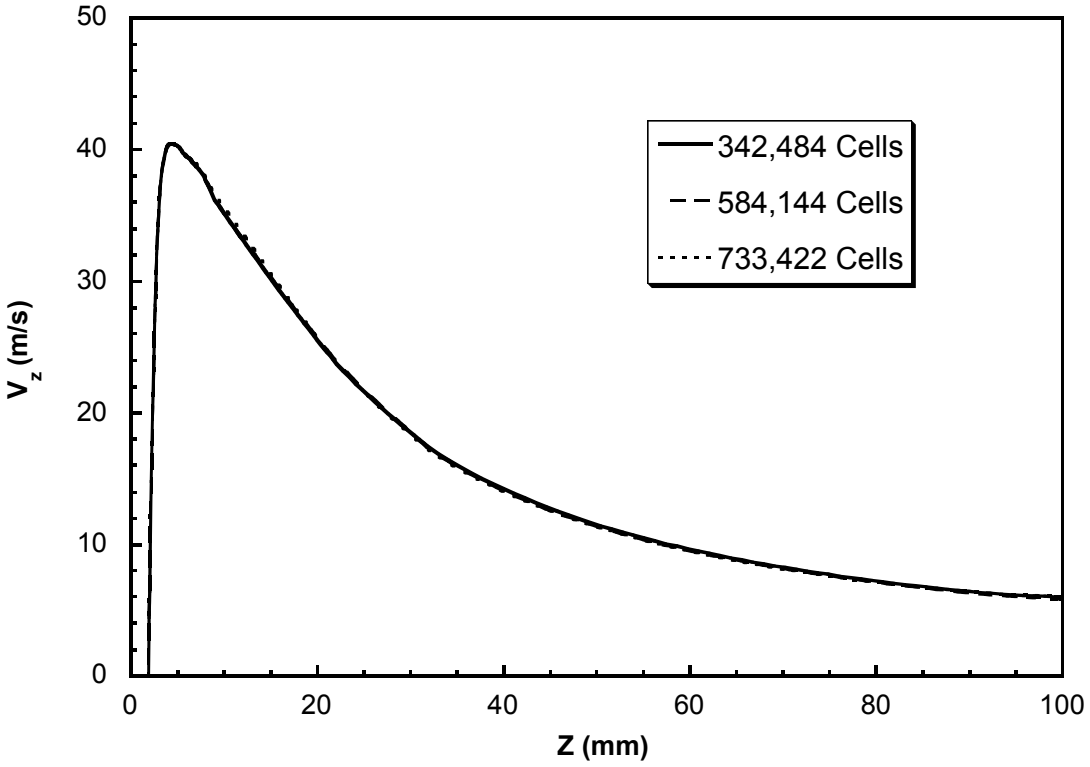

Figure 6.6. Centerline Z-velocity profiles. Three different levels of grid refinement. Air flow = 0.12 g/s, k-ε turbulence model. Experimental die geometry.

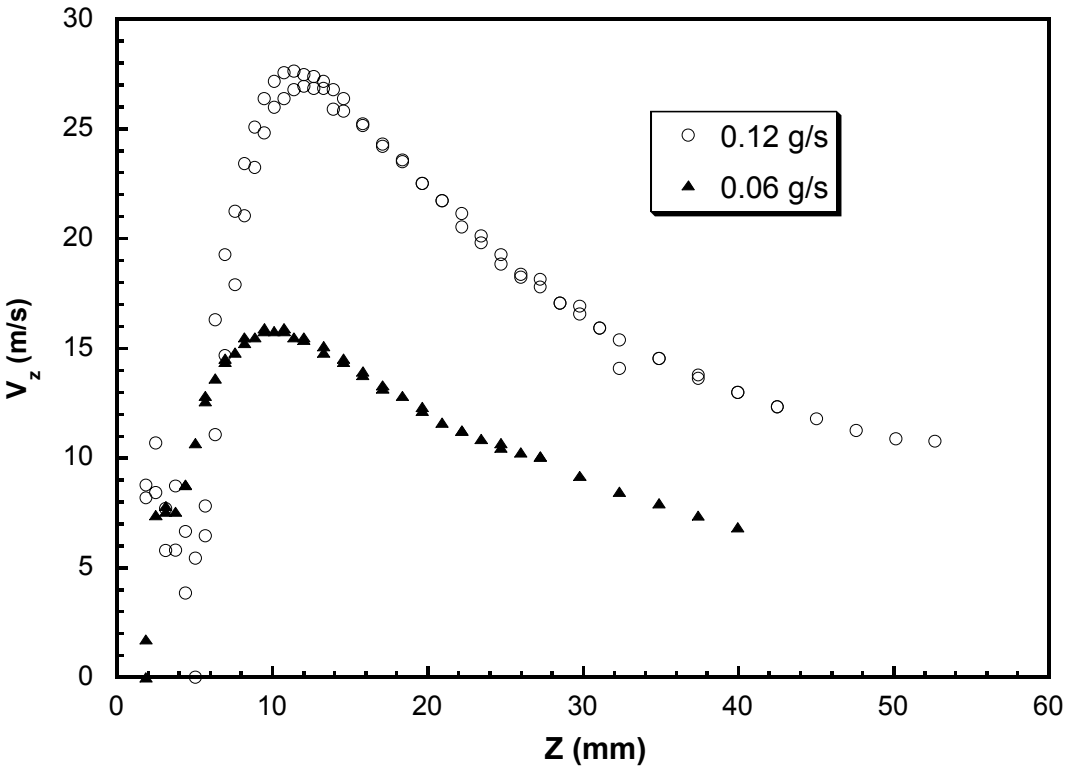

Figure 6.7. Centerline Z-velocity profiles measured with the Pitot tube at two different air flow rates.

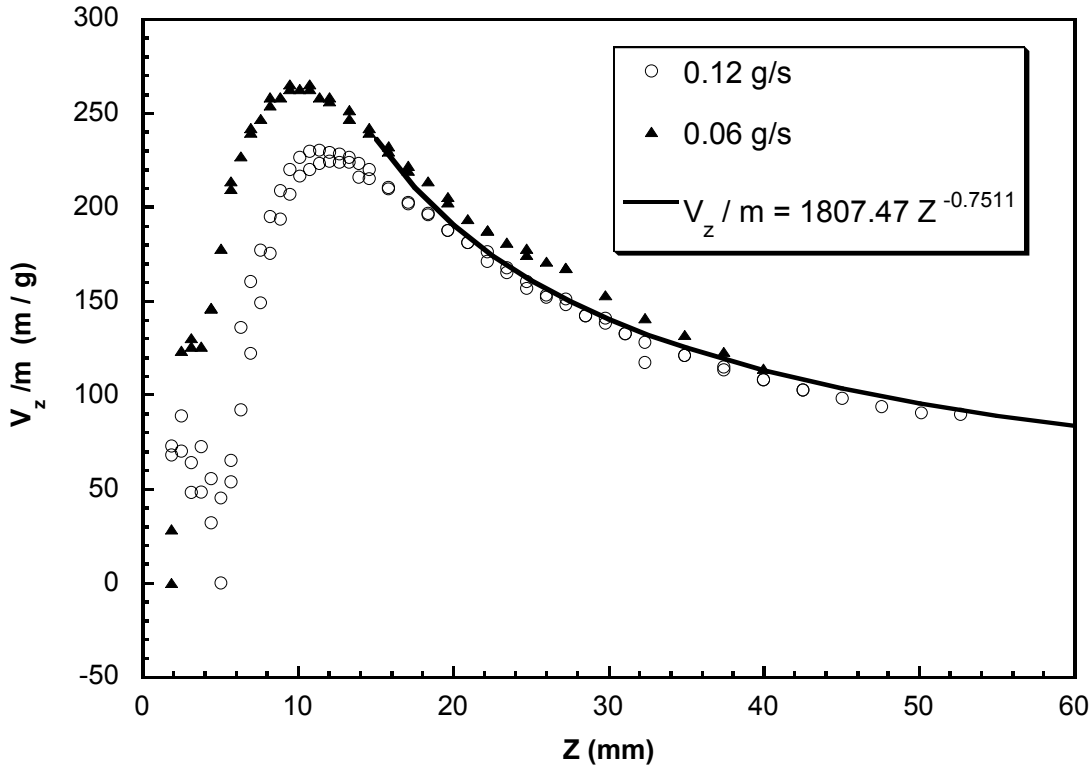

Figure 6.8. Centerline Z-velocity profile, normalized, with best fit curve.

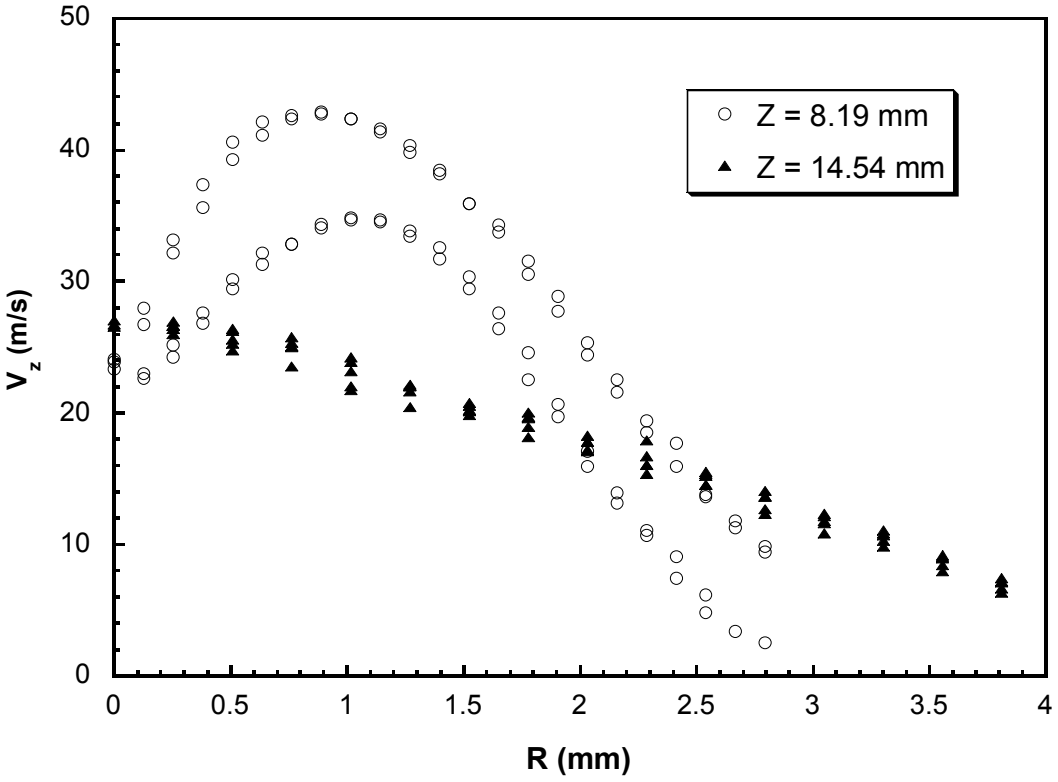

Figure 6.9. Radial Z-Velocity profiles. Taken at two different Z lines with θ = 0° and flow rate of 0.12 g/s.

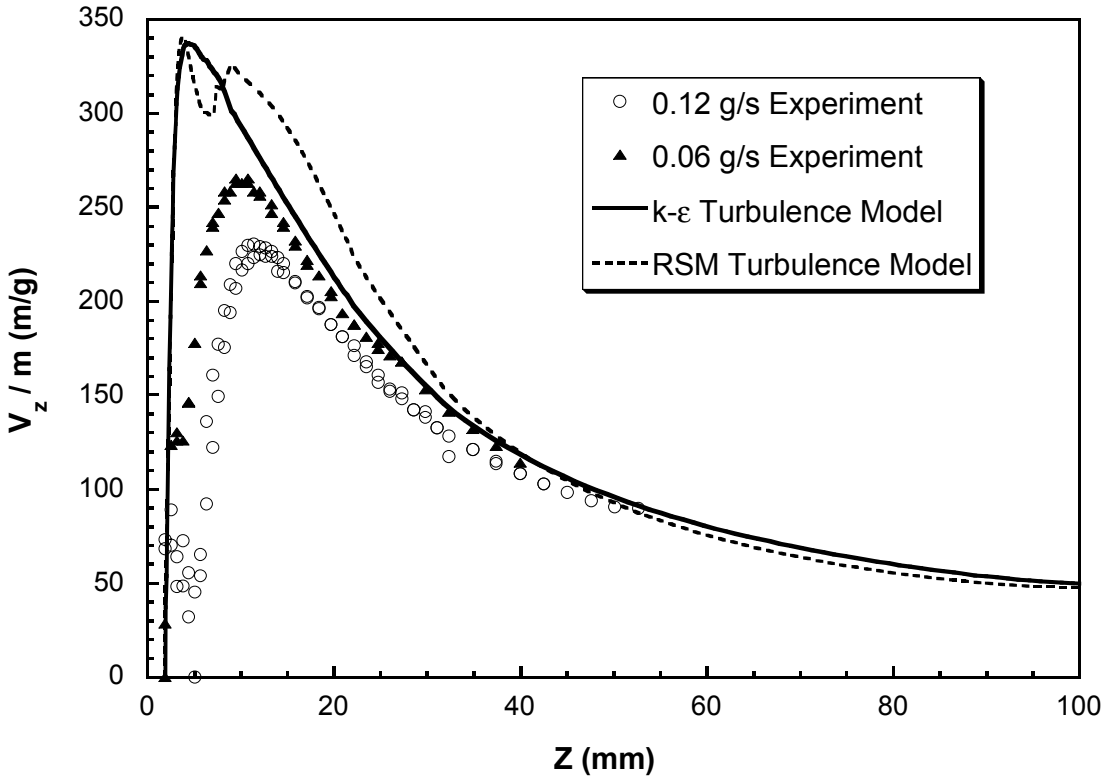

Figure 6.10. Centerline Z-Velocity profiles, normalized: Experiment, k-ε turbulence, RSM turbulence.

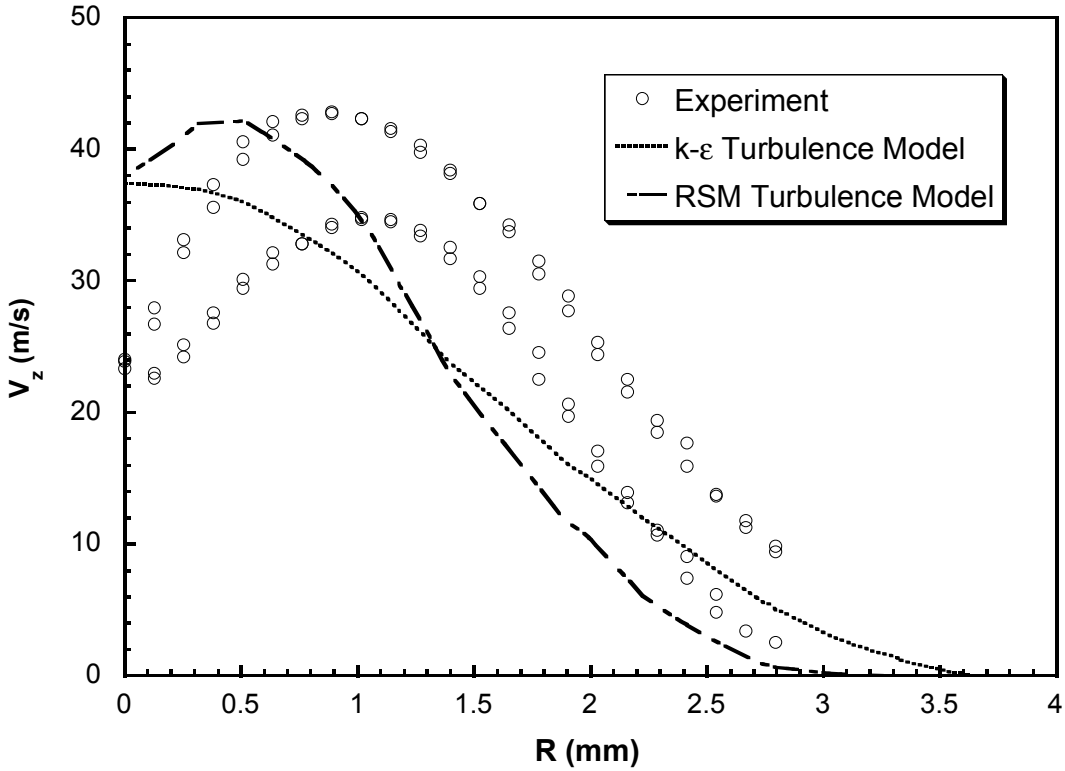

Figure 6.11. Radial Z-Velocity profiles, Z = 8.19 mm, θ = 0°: Experiment, k-ε turbulence, RSM turbulence.

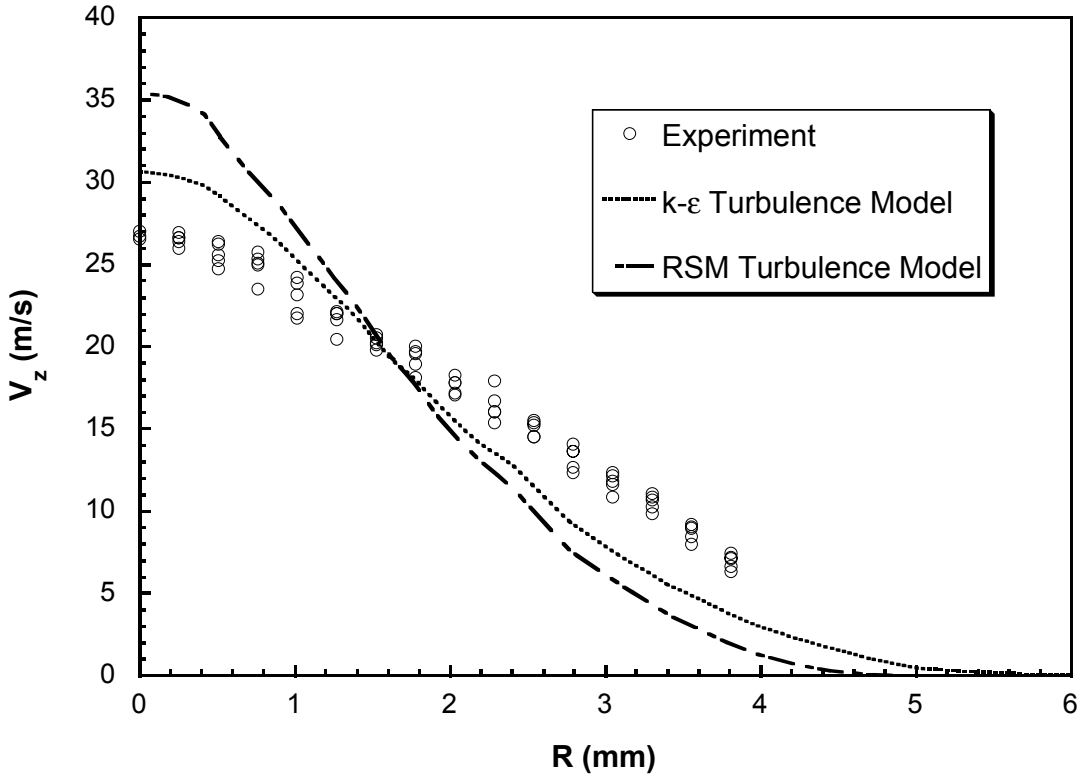

Figure 6.12. Radial Z-Velocity profiles, Z = 14.54 mm, θ = 0°: Experiment, k-ε turbulence, RSM turbulence.

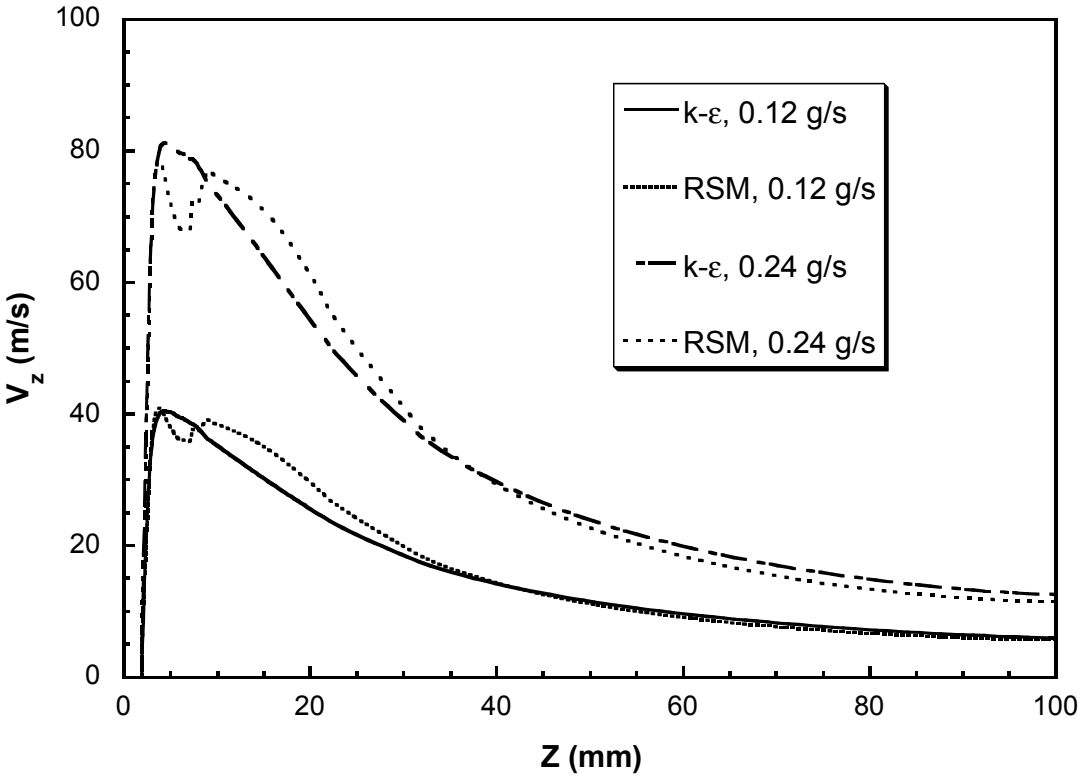

Figure 6.13. Centerline velocity profiles, two flow rates: k-ε turbulence and RSM turbulence.

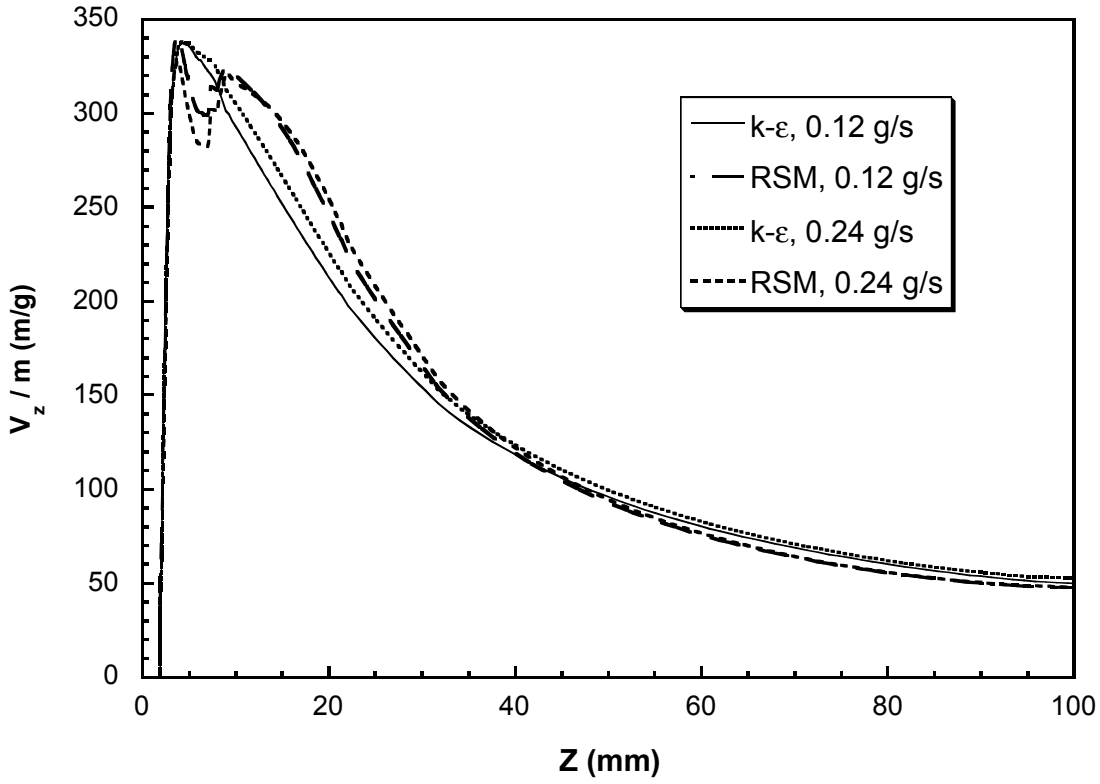

Figure 6.14. Centerline velocity profiles, normalized: k-ε turbulence and RSM turbulence.

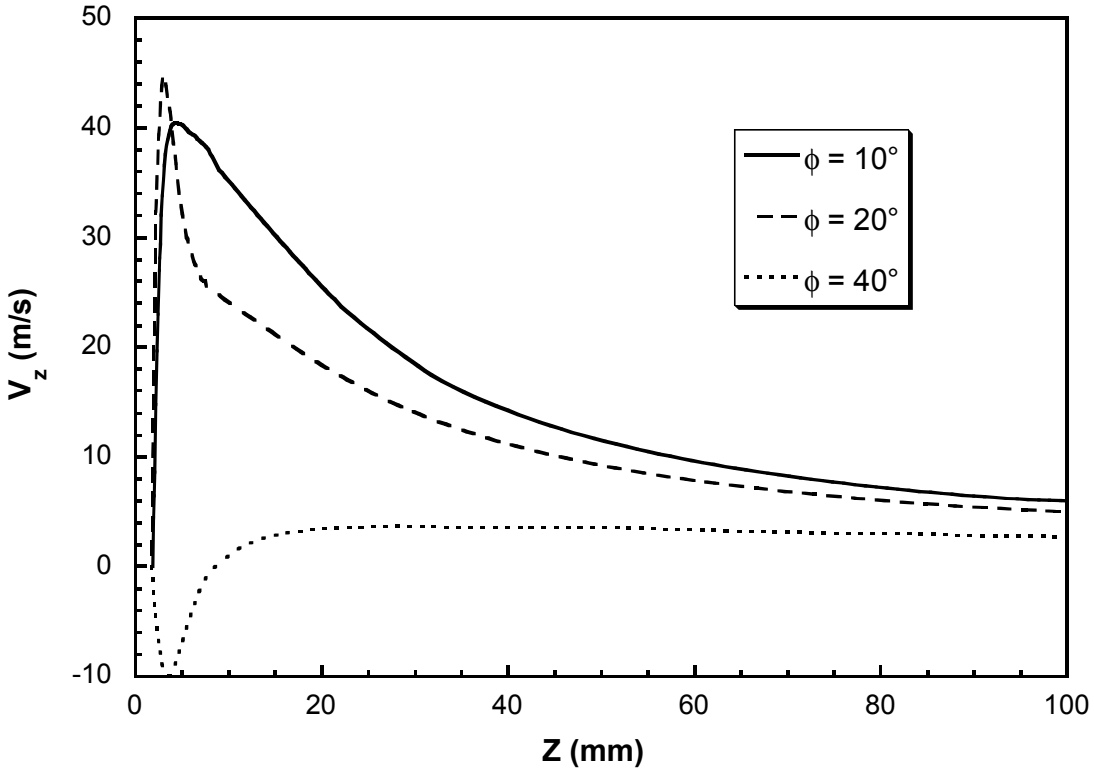

Figure 6.15. Comparison of centerline velocity profiles, varying twist angles (ϕ). 0.12 g/s air flow, k-ε turbulence.

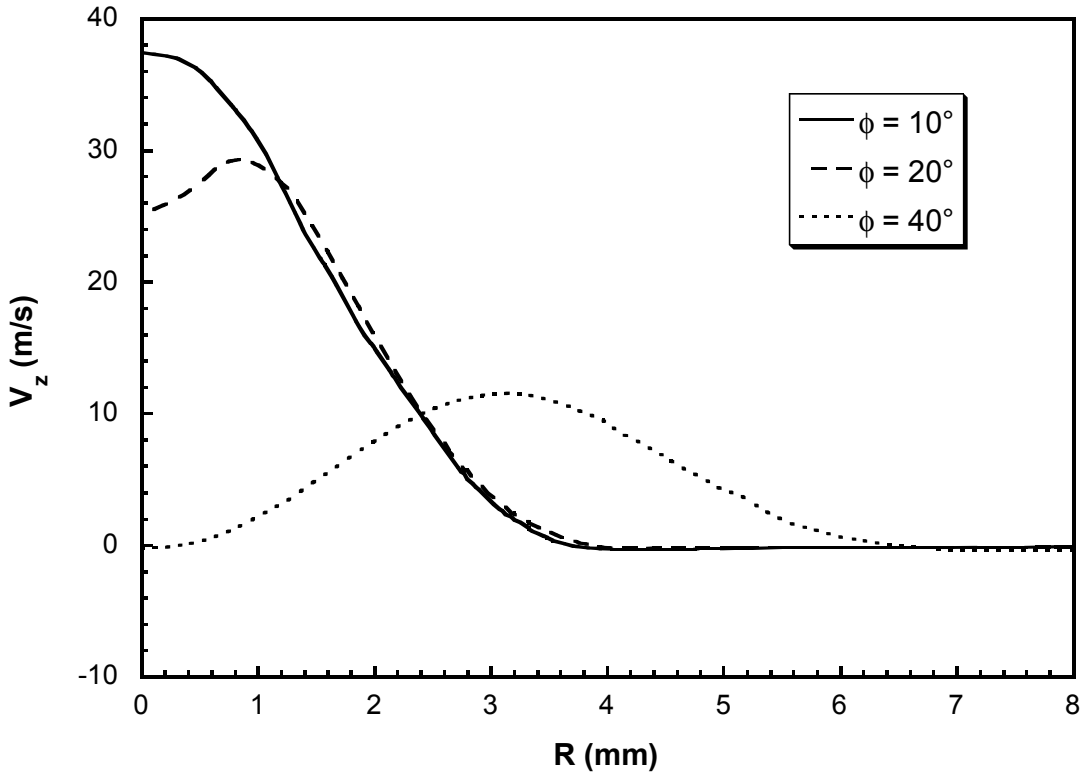

Figure 6.16. Comparison of radial z-velocity profiles, varying twist angles (ϕ). Z = 8.19 mm, $\theta = 0°$, 0.12 g/s air flow, k-ε turbulence.

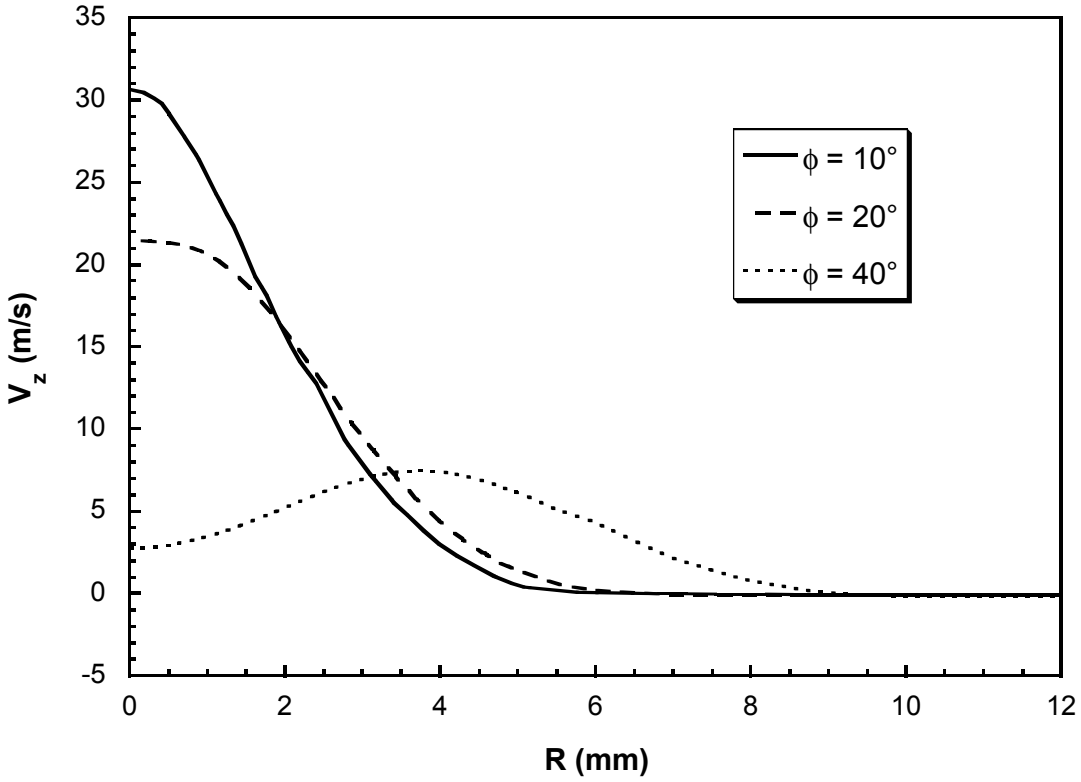

Figure 6.17. Comparison of radial z-velocity profiles, varying twist angles (ϕ). Z = 14.54 mm, $\theta = 0°$, 0.12 g/s air flow, k-ε turbulence.

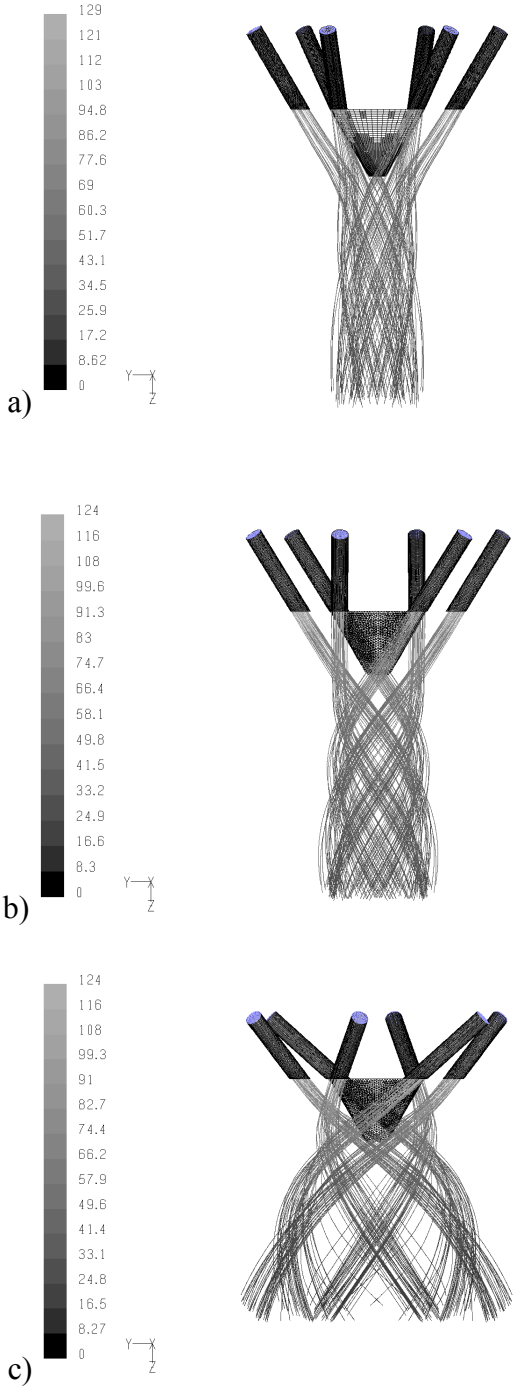

Figure 6.18. Pathlines from the inlet various twist angles. Pathlines colored by mean velocity magnitude. 0.12 g/s air flow. a. $\phi = 10°$ b. $\phi = 20°$ c. $\phi = 40°$

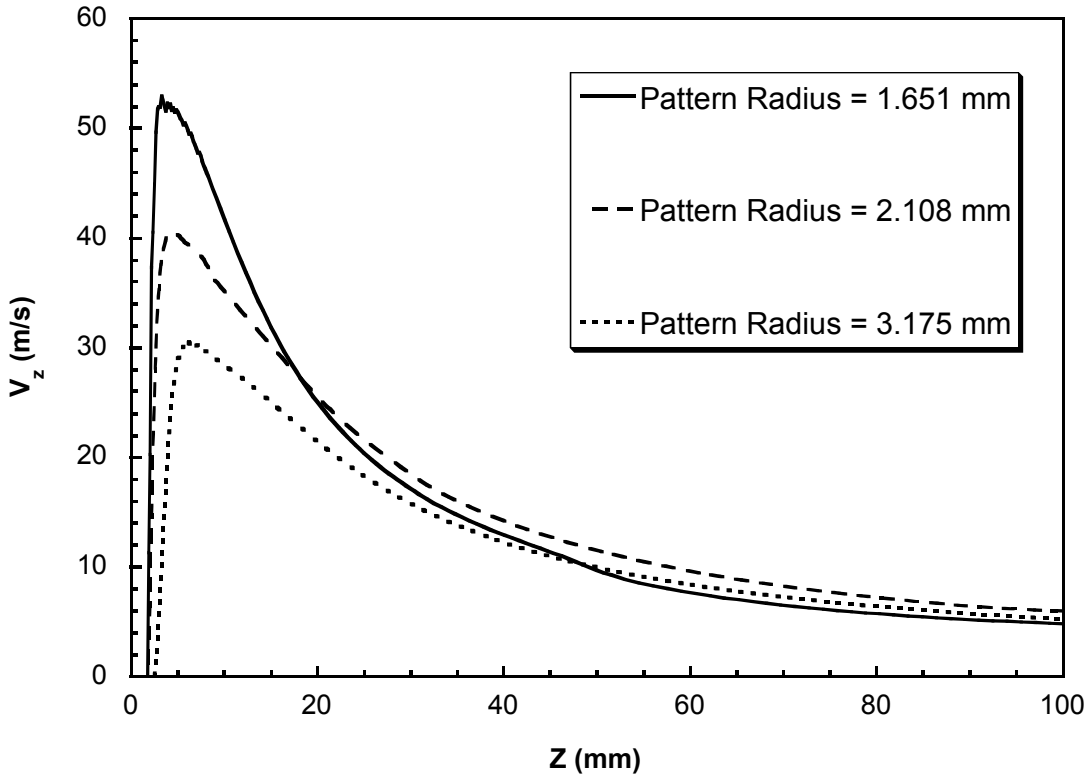

Figure 6.19. Comparison of Centerline velocity profiles, varying pattern radius. 0.12 g/s, k-ε turbulence.

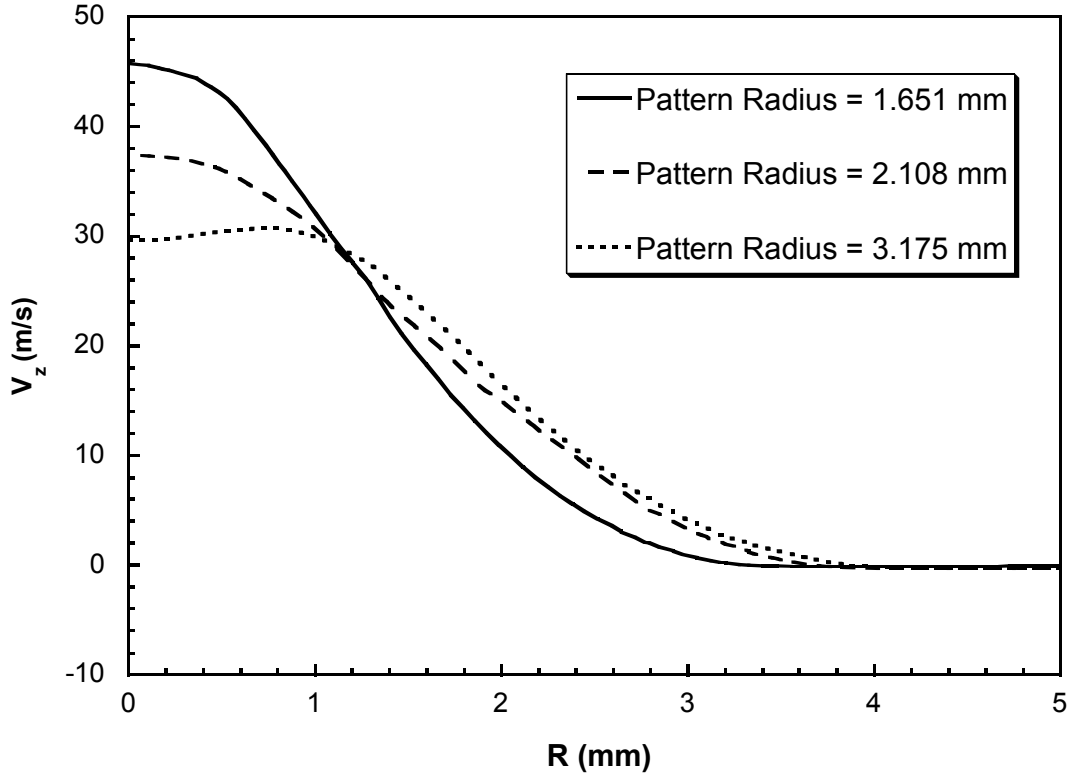

Figure 6.20. Comparison of Radial Velocity Profiles Z = 8.19 mm, 0.12 g/s, k-ε turbulence.

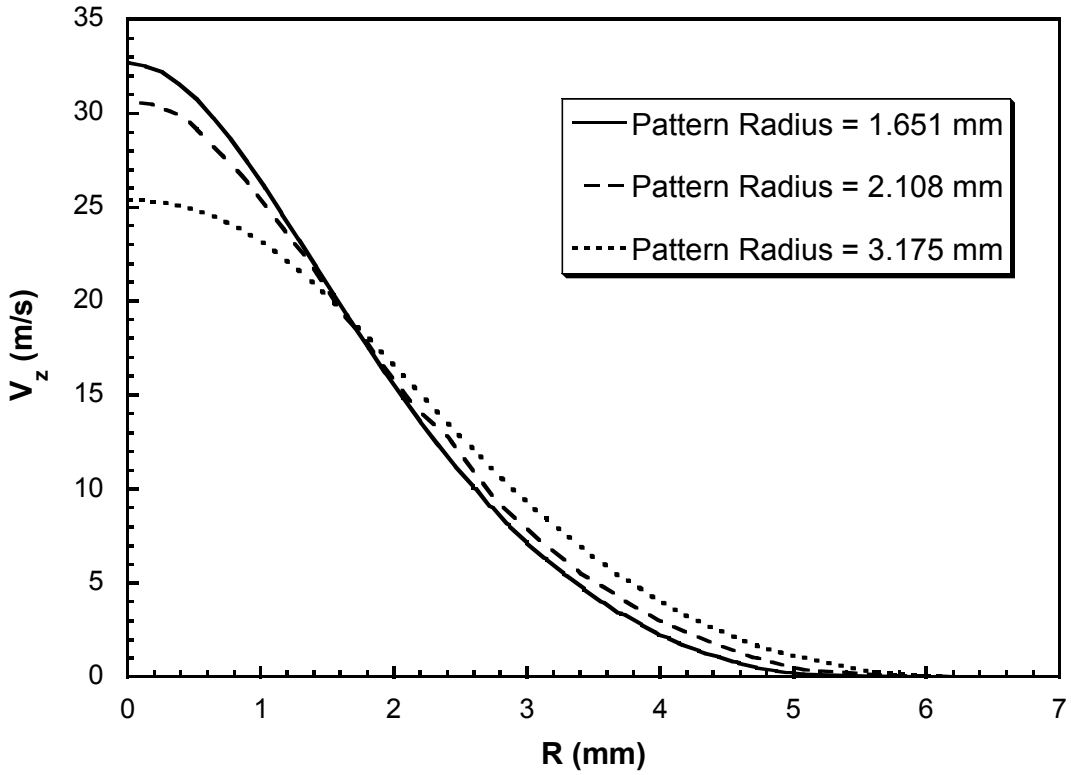

Figure 6.21. Comparison of Radial Velocity Profiles Z = 14.54 mm, 0.12 g/s, k-ε turbulence.

Chapter 7

Conclusion

7.1 Conclusions

This work has studied the aerodynamics and operating characteristics of melt blowing dies, both experimentally and computationally. Computational work focused on the development of computational fluid dynamic (CFD) techniques for the quantitative simulation of annular melt blowing flows, including swirl nozzles. Experimental work collected data on the aerodynamics and operating characteristics of a pilot scale melt blowing die of commercial design. This experimental work will be used to further develop the modeling and simulation techniques for melt blowing processes.

Simulation of melt blowing jets using CFD looked at the behavior of melt blowing jets both within and outside the range of available experimental data. It was found that for annular melt blowing jets, a properly configured Reynolds Stress Model (RSM) for turbulence gives a very good match with experimental data, for

both centerline velocity as well as jet spreading. An empirical correlation for the centerline velocity profile of a compressible annular melt blowing jet was developed, matching both CFD results and experimental data. A design study was performed on the effect of taper on the flow field of annular melt blowing dies. The taper angle of an annular jet was found to have a relatively minor effect on velocity, but a large effect on the turbulence generated near the die face. For swirl nozzles, experimental data was collected, and a CFD technique appropriate for the complex geometry was developed. The swirl nozzle work represents some of the first detailed CFD studies of a fully three-dimensional melt blowing geometry, and presented numerous challenges. Ultimately, a technique was developed that agreed with experimental data in the far field, and a study of die design parameters was performed. It was found that increasing the twist angle of a swirl nozzle could cause the air jets to transition from converging behavior to diverging behavior.

Due to the amount of CFD analysis that has been done to date on melt blowing geometries, it is now possible to construct a table of recommended techniques for accurate simulations. Table 7.1 shows the recommended turbulence models and constants for three classes of melt blowing dies. The results for slot dies are from the work of Krutka et al. (2002). It is clear from the table that all the techniques match the centerline profiles fairly well. There is, however, some difficulty in the accurate prediction of the jet spreading rate.

Experimental work included studies of the aerodynamics of melt blowing dies and swirl nozzles. Photographic measurements were taken of the viber vibration amplitudes during the melt blowing process. Also a new ensemble laser diffraction

(ELD) technique was applied to measure the fiber diameter distribution during the operation of a pilot scale melt blowing die. Aerodynamic data explored the three-dimensional flow field of a slot melt blowing die and related the operating characteristics to finished fiber properties. ELD showed both fiber attenuation and bundling during the melt blowing process, also it showed that for the die under study the fiber diameter was independent of the fiber's position along the length of the die. Light abosrbtion measurements showed that the absorbance was accurately modeled using only the mean diameter, with the diameter distribution playing only a minor role.

7.2 Suggestions for Future Work

The study of melt blowing dies has progressed to the point where simulations can be used not only to understand, but also to predict the performance of melt blowing die deigns. With the modeling work of Marla and Shambaugh (2003), the next logical step is to begin the process of coupling the aerodynamic model with the fiber dynamics model. The initial formulation of this coupled model will probably involve a scripted interface between the existing fiber dynamics model and CFD results files. Such formulation would have the disadvantage of assuming that the fiber has no effect on the air flow, but would allow for unsteady flow behavior to affect the fiber. Ultimately, one would like to simulate both the air and fiber together within one computational framework. The inherent complexity of a model like this will require considerable time and effort to develop.

Experimentally, the aerodynamic study of melt blowing dies should continue. The current work included, there is still too little aerodynamic data available to

develop proper correlations that could fully predict the flow fields of commercial scale dies. Secondly, the study of melt blowing jet turbulence is just beginning. Modern flow characterization techniques, such as laser Doppler velocimetry and particle image velocimetry, should be applied to the melt blowing flows to determine the true turbulent nature of melt blowing dies.

7.3 References

Krutka, H.; Shambaugh, R.L.; Papavassiliou, D.V. “Analysis of a Melt Blowing Die: Comparison of CFD and Experiments”, *Ind. Eng. Chem. Res.* **2002**, *41*, 5125-5138.

Marla, V.T.; Shambaugh, R.L. “Three-Dimensional Model of the Melt-Blowing Process”, *Ind. Eng. Chem. Res*. **2003**, *32*, 6993-7005.

						Accuracy of Results	
Die Class	**Source**	**Turb. Model**	**Cε1**	**Cε2**	**Solver**	**Centerline**	**Jet Spreading**
Slot	Krutka, et al.	RSM	**1.24**	**2.05**	Segregated	Excellent	Poor
Slot*	Krutka, et al.	RSM	**1.44**	**1.92**	Segregated	Poor	Poor
Annular	This Work	RSM	**1.44**	**1.82**	Segregated	Excellent	Good
Annular*	This Work	RSM	**1.44**	**1.92**	Segregated	Poor	Poor
Swirl Nozzle	This Work	k-ε**	**1.44**	**1.92**	Coupled - Implicit	Good	Fair

* FLUENT® Default Values

** RSM for swirl nozzle geometry diverges with 2nd order upwind discretization

Table 7.1 Turbulence modeling techniques for various melt blowing dies. Model parameters not listed are use the default values for FLUENT®.